Spring 2021

Elucidation of VPS13 and PIKfyve Proteins Functioning in the Regulation of Eukaryotic Lipid Homeostasis

PeiQi Li
Yale University Graduate School of Arts and Sciences, peiqi.li@yale.edu

Recommended Citation

Li, PeiQi, "Elucidation of VPS13 and PIKfyve Proteins Functioning in the Regulation of Eukaryotic Lipid Homeostasis" (2021). *Yale Graduate School of Arts and Sciences Dissertations*. 77.
https://elischolar.library.yale.edu/gsas_dissertations/77

Abstract

Elucidation of VPS13 and PIKfyve Proteins Functioning in the Regulation of Eukaryotic Lipid Homeostasis

PeiQi Li

2021

In eukaryotic cells, organelles are surrounded by membranes, which act as barriers to the cytosolic environment. Each subcellular membrane has a distinct lipid composition that is required for its unique organellar function, and is therefore is fundamental for cellular physiology. The unique distributions of organellar lipids result from highly regulated lipid transport networks and the activity of lipid metabolizing enzymes. Most phospholipids are initially synthesized in the ER and transferred to different organelles via vesicular or non-vesicular lipid transport pathways. Lipid transfer proteins (LTPs) localized at membrane contact sites mediate non-vesicular lipid transport. They contain a hydrophobic cavity to solubilize the hydrophobic “tail” of lipids. They either function as “shuttles” that typically ferry a single lipid at a time between membranes, or “bridges” that harbor hydrophobic channels along which more than one lipid can move between membranes at a time. For the first part of my thesis, I investigated the structure and function of VPS13, a novel lipid transfer “bridge” protein, and showed that the protein accommodates a 16nm long hydrophobic lipid transfer channel that mediates bulk lipid

transfer. My work marked the identification of the first lipid transfer bridge in eukaryotes and raised several still open questions regarding the molecular mechanism of bridge-like LTPs. I further investigated VPS13’s WD40 domain to provide insights into how VPS13 interacts with membranes at membrane contact sites.

The second part of my thesis focused on the modification of phosphatidylinositol (PI), which is essential in signalling. Phosphorylation on different positions of the head group of PI generates several phosphoinositide (PIP) species. Each of them has a unique subcellular localization. $PI(3,5)P_2$ is one of the signature phosphoinositides in endolysosomal membranes, whose level is tightly upregulated in response to stimuli. $PI(3,5)P_2$ is solely synthesized by the PIKfyve lipid kinase and its turnover is catalyzed by the Fig4 lipid phosphatase. Intriguingly, the two proteins, although catalyzing antagonistic reactions, are in the same complex together with a third protein, the scaffold Vac14. Little is known about how the activities of PIKfyve and Fig4 are regulated to prevent futile consumption of ATP. Combining structural and biochemistry studies, I gained insights into the overall architecture of the PIKfyve complex and into the regulatory mechanisms that govern PIKfyve and Fig4 activities.

Elucidation of VPS13 and PIKfyve Proteins Functions in Regulating Eukaryote Lipid Homeostasis

A Dissertation

Presented to Faculty of the Graduate School

Of

Yale University

In Candidacy for the Degree of

Doctor of Philosophy

By
PeiQi Li

Dissertation Director: Karin M. Reinisch, PhD

June 2021

Table of Contents

Acknowledgement

I would like to thank Karin M. Reinisch for being my supervisor throughout my Ph.D. I was and still am encouraged by her serious attitude towards science and her passion for exploring new possibilities. I would also like to thank my thesis committee members: Thomas Melia, Yong Xiong, and Christian Schlieker for their guidance and suggestions during my annual committee meetings. Thirdly, it was my honor to work with Joshua A. Lees, Nikit Kumar, and Florian A. Horenkamp during my Ph.D. They are not just collaborators but also role models for my life. It was also my honor to collaborate closely with Patrick Lusk for one of my projects. As a young professor under huge amounts of pressure, he showed the greatest positive attitude towards life. I would like to thank my colleague and also friend Patreece Suen. We spent most of the time sitting next to the bench talking about science, research, food, fiction books, and celebrities. She brought happiness and joy to my life. I would like to thank other members of Reinisch Lab. I am also grateful for people in the Cell Biology Department. I want to thank them for their generosity towards me, letting me borrow their instruments, reagents, time, and snacks. I would like to lastly thank my parents Guanhua Wang and Zhenjian Li as well as my partner Mingyuan Fu. Although they were far away during the past five years, they are my family, and always there for me.

Chapter 1 Introduction

Abbreviations

PC: phosphatidylcholine; PE: Phosphatidylethanolamine; PS: Phosphatidylserine; PI: Phosphatidylinositol; GPL: glycerophospholipid; ER: Endoplasm reticulum; PM: plasma membrane; MCS: membrane contact site; NVJ: nucleus–vacuole junction; LTP: lipid transfer protein; OSBP: Oxysterol-binding protein; ORP: OSBP related protein; PITP: Phosphatidylinositol transfer protein; SMP: Synaptotagmin-like mitochondrial-lipid-binding protein; TULIP: tubular lipid-binding domain protein; CL: Cardiolipin; LPS: lipopolysaccharide

Chapter 1.1 Glycerol lipids and membranes

Lipids are a category of macromolecule defined by their inability to mix with polar solvents. They function as primary chemical energy storage molecules and are essential nutrients for human health. At the molecular level, they are the primary building blocks of cellular and subcellular membranes. Cells are surrounded by membranes, which act as barriers to the extracellular environment. Compartmentalization within eukaryotic cells into membrane-bound organelles allows for micro-environments adapted for specialized functions. The lipid compositions of different organelles are distinct, and the lipid composition of organelles can even change in response to stimuli. Membrane lipids are highly diverse, with potentially 100,000 lipid species, and 5% of our genes are related to lipid synthesis (Frolov, Shnyrova, & Zimmerberg, 2011; Shevchenko & Simons, 2010; van Meer, Voelker, & Feigenson, 2008). Maintaining the lipid homeostasis of organellar membranes is fundamental for cellular life.

Chapter 1.1.1 Glycerophospholipid basic structure, classification and character

The lipid components of eukaryotic membranes can be classified into two major categories, glycerolipids and sphingolipids, based on their backbones (Figure 1.1). As implied by their name, glycerolipids have a glycerol backbone, with two fatty acid lipid groups attached to the C1 and C2 positions of glycerol known as hydrophobic "tail." The C3 position is also modified via the addition of a polar "headgroup" moiety to give rise to different sub-classes of glycerolipid. Glycerophospholipids have a phosphate ester at the C3 position linked to choline, ethanolamine, serine, or inositol to give rise to phosphatidylcholine (PC), phosphatidylethanolamine (PE), phosphatidylserine (PS), or phosphatidylinositol (PI). Variability in the size or electric charge in the headgroup, or length or saturation in the "tail," gives these lipids different properties. Sphingolipids use

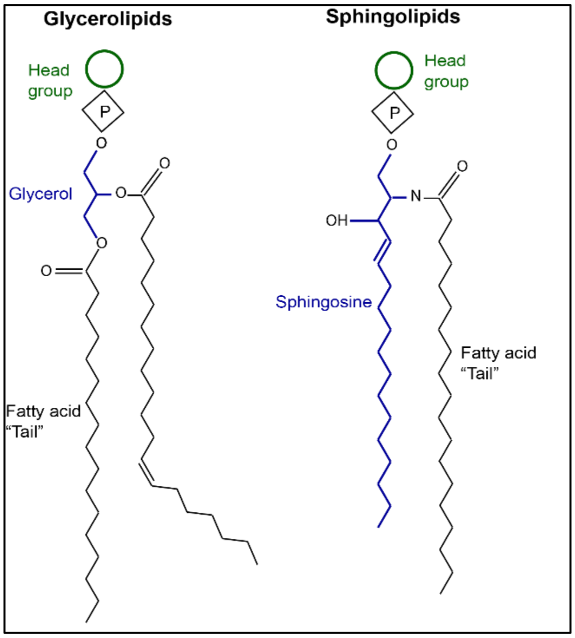

Figure1.1: Overall structure of Glycerolipids and Sphingolipids

sphingosine as the backbone with a long saturated fatty acid linked via amide linkage (Figure 1). Ceramide and sphingomyelin are common sphingolipids, with different head groups (Holthuis & Menon, 2014; van Meer & de Kroon, 2011).

Due to the amphiphilic property of membrane lipids, they naturally form a double layer membrane structure with “head” groups facing towards the cytosolic environment and “tail” groups embedded inside. PC is the most abundant phospholipid in membrane bilayers, accounting for more than 50% of membrane lipids. Because the diameters of the “head” and “tail” groups are similar, PC is cylindrical, allowing it to assemble into bilayers under normal physiological conditions. Non-bilayer lipids such as PE and diacylglycerol (no head group) are cone-shaped due to their relatively small “head” and wide “tail,” and so do not form a stable membrane bilayer by themselves. Their conical shape introduces packing defects into membranes, promoting the binding of peripheral membrane proteins, and induces membrane curvature. The head group of PS is negatively charged, allowing it to bind peripheral membrane proteins via electrostatic interactions (Chernomordik, Zimmerberg, & Kozlov, 2006; Dowhan, 1997; Frolov et al., 2011; Lee, 2004). The PI headgroup can be rapidly phosphorylated and dephosphorylated to generate seven different species of phosphoinositide lipids that specifically recruit adaptor proteins during signal transduction (Balla, 2013).

Each subcellular membrane has a distinct membrane lipid composition fundamental for cellular physiology (Frolov et al., 2011). Global lipid composition largely determines the physical properties of cellular membranes including overall shape, curvature, packing, and tension. In general, the endoplasmic reticulum (ER) contains mostly unsaturated glycerophospholipids, while cholesterol and sphingolipids are enriched at the plasma membrane (PM). Mitochondrial membranes are enriched in PE and cardiolipin. The seven phosphoinositides have distinct organellar distributions (Harayama & Riezman, 2018; van Meer & de Kroon, 2011). The unique distributions of bulk and signaling lipids result from directionality and selectivity in lipid transfer, and the activity of lipid metabolizing enzymes. Overall, changes in lipid composition are carefully tuned and tightly regulated (van Meer et al., 2008).

Chapter 1.1.2 Lipid synthesis and transportation

Lipid synthesis is compartmentalized to different organelles due to the localization of specific enzymes. The ER is the primary site for the synthesis of PC, PA, PI, and PS, while PE and cardiolipin are synthesized in mitochondria (Yang, Lee, & Fairn, 2018). Most other biological membranes, such as the PM and endosomes, do not have the capability to synthesize glycerophospholipids and must acquire newly synthesized lipids from ER. In eukaryotic cells, there are two major mechanisms for lipid transport: vesicular transport via the secretory pathway or protein-mediated lipid transport at so-called membrane contact sites (MCSs). Vesicular transport in the secretory pathway has long been studied as a means of bulk lipid transfer between the ER, Golgi, endosomes, and PM. Non-vesicular protein-mediated lipid transfer also takes place between organelles of the secretory pathway but is particularly important for organelles not connected to the secretory pathway, such as mitochondria and chloroplasts (Scorrano et al., 2019). Non-vesicular protein-mediated lipid transfer is more selective for fine-tuning membrane compositions and responds quickly to stimuli, versus having to travel via the secretory pathway. What has been learned about lipid transfer at MCSs in recent years will be discussed in more detail below.

Chapter 1.1.3 Membrane contact sites

The close proximity between the ER and mitochondria was first observed in the 1950s in liver cells after starvation and refeeding (Bernhard & Rouiller, 1956). Later, the concept of membrane contact sites started to emerge with discoveries such as ER and PM connections in skeletal muscle cells (Kawamoto, Brunschwig, Kim, & Caswell, 1986) and the identification of the nuclear–vacuolar junction (NVJ) in yeast (Pan et al., 2000). The study of MCSs has gained momentum in the last ten years. Membrane contacts are defined as sites where the membranes of two organelles come into close proximity without fusing. Although it was initially thought that MCSs always involve the ER, it is now clear that any two organelles can form contacts; for example, there are contacts between lipid droplets and mitochondria, between mitochondria and the PM, and between mitochondria and peroxisomes (Eisenberg-Bord, Shai, Schuldiner, & Bohnert, 2016). The distance between two membranes is largely determined by tethering proteins linking the membranes and is typically between 10 -30 nm. Contact sites mediate the transportation of lipids, ions, amino acids, and metals; the transmission of signaling information for the downstream events such as autophagy; and can regulate organelle morphology (Friedman et al., 2011; Knoblach & Rachubinski, 2015; Lewis, Uchiyama, & Nunnari, 2016). Contacts have also been proposed to allow enzymes in one membrane to access substrates *in trans* on another organelle (Eden, White, Tsapara, & Futter, 2010; Stefan et al., 2011). Each contact site has unique functions, with a unique set of proteins that carry out these functions (Muik et al., 2011; Stathopulos, Zheng, Li, Plevin, & Ikura, 2008). One of the major functions of MCSs is lipid transfer, which occurs in response to stimuli, either specifically or non-specifically. The importance of lipid transfer has been elucidated at ER and mitochondria contact sites. Mitochondria purified from rat liver cells contained a fraction of ER enriched with lipid biosynthesis enzymes (Vance, 1990). It has long been known that in mammalian cells, PS is synthesized in mitochondria, and then transferred back to the ER to synthesize PE. Also, cardiolipin is solely synthesized in the mitochondria and transferred back to the ER for the synthesis of PA. To fulfill the synthesis of these lipids, they need to be transferred between the ER and mitochondria in a selective and specific fashion. Furthermore, mitochondria need bulk lipids from the ER to maintain expansion. Given that mitochondria are not connected to vesicular transport, the close apposition between the ER and mitochondria serves as an ideal hub for high-volume lipid transfer. Non-vesicular lipid transport is mediated by lipid transfer proteins (LTPs) (Petrungaro & Kornmann, 2019).

Chapter 1.2 Lipid transfer protein families in cells

Because of their large hydrophobic moieties, lipids are poorly soluble in aqueous environments, and *in vitro* studies demonstrate that spontaneous lipid exchange between even closely apposed membranes is too slow to be physiologically relevant (McLean & Phillips, 1984). Lipid transfer proteins extract lipids from membranes and solubilize them to accelerate lipid exchange between membranes. The number of known LTPs has greatly risen in the past decade and are found in all organisms, from bacteria to humans.

LTPs typically have a hydrophobic cavity that binds the hydrophobic portions of the lipid normally embedded in the lipid bilayer. Most LTPs involved in glycerolipid transfer that have been studied so far are not specific for acyl chain length, where the acyl chains bind in the hydrophobic cavity, but many recognize a specific headgroup. In general, LTPs fall into two main categories: “shuttles” and “bridges.” They differ in hydrophobic cavity size and mechanism. Most eukaryotic LTPs identified so far are “shuttles” that ferry a single lipid at a time between membranes, and the cavity is normally selective for certain lipid species; in some cases, they exchange two distinct lipid species between membranes. Instead, “bridges” are thought to form a static hydrophobic conduit to allow for bulk lipids moving along within. It has been speculated that “bridges” have no selectivity since lipids are not occupying certain binding sites inside of the hydrophobic conduit (Figure 1.2). Indeed, our understanding of the molecular mechanism of LTPs is still limited, but the identification of several LTPs has improved our knowledge of the field. Several typical LTP families will be discussed below.

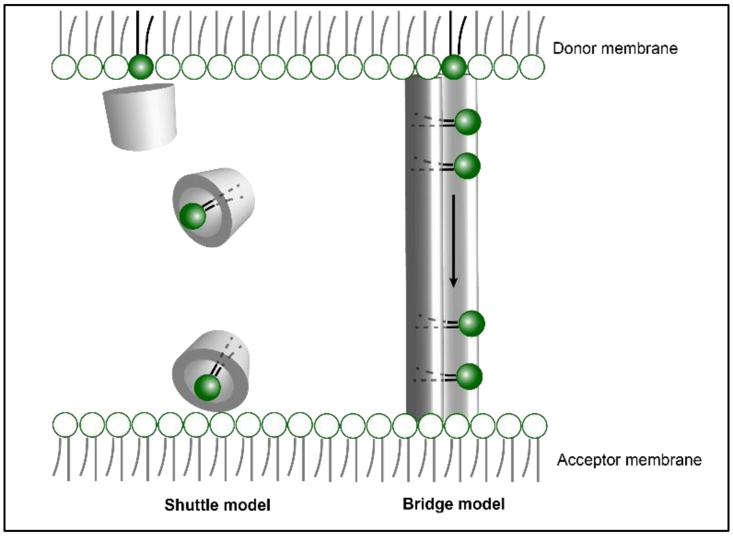

Figure 2: Comparison of shuttle model and bridge model of lipid transfer protein

Chapter 1.2.1 Shuttle-like lipid transfer proteins

OSBP-related protein family

Oxysterol-binding proteins (OSBP) and OSBP-related proteins (ORP) are conserved in all eukaryotes (Kentala, Weber-Boyvat, & Olkkonen, 2016). In humans, they are encoded by 12 genes and classified into six distinct subfamilies (Kentala et al., 2016), and localize to ER-PM, ER-Golgi, ER-late endosome, and ER-lipid droplet contact sites. All proteins in the ORP family have an ORD (OSBP-related domain) lipid-binding module. Additionally, some of the proteins also contain motifs for correct localization, recognizing specific phosphoinositides or proteins enriched at particular contact sites (Olkkonen, 2015). Several ORD domains of the ORP protein family specifically interact with two species of lipid; one of these is a phosphoinositide and the other is sterol or PS (Wong, Gatta, & Levine, 2019). These proteins mediate the exchange of lipids between membranes: they transport sterol or PS against a gradient by harnessing the energy present in the phosphoinositide gradients in the two membranes. For example, OSBP transfers cholesterol from the ER to the Golgi, where sterol is enriched, and PI4P from the Golgi, where PI4P is enriched, in the opposite direction (Mesmin et al., 2013). PI4P flowing forward in the gradient provides the energy for transferring cholesterol contrariwise to its gradient. ORP1 and ORP2 facilitate cholesterol transport between the ER and other organelles, including lipid droplets and late endosomes (Hynynen et al., 2009; Rocha et al., 2009). The ORP protein family participates in many cellular processes, including phosphoinositide and neutral lipid metabolism, apoptosis, and viral replication (Olkkonen, 2015).

PITP and Sec14 protein family

Phosphatidylinositol transfer proteins (PITPs) bind PI and PC, mediating their transfer or exchange between organellar compartments (Hsuan & Cockcroft, 2001). Sec14 and PITP family proteins are structurally distinct but functionally interchangeable. In humans, PITP proteins are divided into two classes. Class I proteins are compact, comprising only a lipid binding module, the so-called PITP domain. Class II proteins have additional modules, such as DDHD and LNS2 domains responsible for interacting with PM lipids, and some contain an FFAT motif to attach them to the ER (Cockcroft, 2012; Saheki & De Camilli, 2017). The hydrophobic cavity of the PITP domain binds either PI or PC, though the binding affinity to PI is 16-times higher than PC. This is due to a series of conserved residues in the cavity that form hydrogen bonds to the inositol group of PI (Hsuan & Cockcroft, 2001). Class II PITP proteins are thought to facilitate non-vesicular PI transfer at ER-PM contact sites (Saheki & De Camilli, 2017). They are proposed to present PI to lipid kinases at the PM during phosphoinositide synthesis there (Cockcroft, 2012). PITP may be evolutionarily related to the START family of lipid transporters, but binds to different lipids species (Radauer, Lackner, & Breiteneder, 2008).

SMP domain containing protein family (TULIP)

The synaptotagmin-like mitochondrial-lipid-binding protein (SMP) domain belongs to a tubular lipid-binding (TULIP) domain superfamily and is conserved across eukaryotes (Kopec, Alva, & Lupas, 2010). The SMP domain is characterized by an extended barrel shape with an inner cavity lined with hydrophobic residues that binds lipids (Reinisch &

De Camilli, 2016; Schauder et al., 2014). SMP domain proteins localize to different contact sites to promote lipid transfer between the ER and PM, or between the ER and other organelles. Several SMP domain-containing proteins have been identified to improve our knowledge about this protein family. The E-syt proteins, known as tricalbins in yeast, go to ER-PM contacts. E-syts comprise an N-terminal hairpin that is inserted into the membrane of the ER, an SMP domain, and finally 3-5 C2 domains at their C-terminus (Schulz & Creutz, 2004). The C2 domains interact with the PM depending on cytosolic calcium levels or interact with PI(4,5)P_2, a phosphoinositide enriched at the PM. E-syt2 dimerizes via its SMP domains, which form a 90 Å tube-like structure that can accommodate four glycerolipids at a time (Reinisch & De Camilli, 2016; Schauder et al., 2014). Because the SMP dimer is too short to bridge the space between membranes at contact sites, it was proposed to act as a shuttle, although it remains possible that it could be a bridge-like transporter. The E-Syts seem to interact with glycerolipids non-specifically, and their function in cells is not well understood. They are proposed to function in recycling diacylglycerol produced at the PM during phosphoinositide signaling to the ER, in order to terminate the signal (Saheki et al., 2016).

Another SMP-domain protein that localizes to ER-PM contact sites, present only in metazoa and expressed in neuroendocrine cells, is TMEM24. It has an N-terminal transmembrane helix that anchors it to the ER, followed by the SMP domain, a C2 domain of a still unknown function, and finally a C-terminal polybasic segment that interacts with negatively charged lipids in the PM. The SMP domain in TMEM24 preferentially binds phosphatidylinositol and plays a role in replenishing PI, which is made in the ER, at the PM during insulin secretion (Lees et al., 2017).

The ERMES complex localizes to ER-mitochondrial contact sites in yeast. The complex comprises four core proteins -- Mdm12, Mdm10, Mmm1, and Mdm34 -- and two peripheral proteins, Gem1 and Tom7 (Stroud et al., 2011). Mdm12, Mmm1, and Mdm34 have SMP domains (AhYoung, Lu, Cascio, & Egea, 2017). Mdm12 and Mmm1 form a 210 Å-long tubular heterotetramer. An *in vitro* study using purified protein found that Mdm12 and Mmm1, but not Mmm1 alone, is able to transfer lipids between membranes, indicating that the formation of the tetramer is essential for lipid transfer (AhYoung et al., 2015; Jeong, Park, Jun, & Lee, 2017; Kawano et al., 2018). Whether and how Mdm34 associates with the tetramer is unknown. Also unknown is whether ERMES behaves as a shuttle or instead as a bridge-like protein (Wong et al., 2019). Mdm10 is an integral membrane protein embedded in the mitochondrial outer membrane (Sogo & Yaffe, 1994), and Gem1 is a GTPase with a transmembrane helix anchored in the mitochondrial outer membrane (Kornmann, Osman, & Walter, 2011).

The ERMES complex mediates glycerolipid transfer between the ER and mitochondria and is thought to be required for PS transfer from the ER, where PS is synthesized, to mitochondria, where PS is a precursor for PE. PE is subsequently transferred back to the ER, where it is converted to PC. Supporting a role for ERMES in PS transport, a mutagenesis study showed that PS transfer from the ER to mitochondria is decreased in yeast that does not contain Mdm12 and Mmm1 (AhYoung et al., 2015; Jeong et al., 2017; Kawano et al., 2018).

Chapter 1.2.2 Bridge-like lipid transfer proteins

LPS transporter

Apart from requiring a small volume of certain lipid species, organelles such as mitochondria need bulk lipids from ER to maintain membrane expansion, which is also true for the autophagosome membrane expansion during autophagy and the prospore membrane expansion during sporulation in yeast. It has been widely speculated that such bulk transfer could be mediated by bridge-like LTPs, which form hydrophobic conduits along which lipids can traverse the cytosol between membranes. Some SMP proteins, in particular the ERMES complex, have been proposed to form such bridges (Kornmann, 2020), although this is still under discussion. In general, until our work, the best characterized bridge-like protein was identified from bacteria.

At the outer membrane of gram-negative bacteria, lipopolysaccharide (LPS) functions as a barrier for protection from extracellular hazards, such as antibiotics. The LPS transporter transfers LPS, which is made at the inner membrane of bacteria, to the outer membrane, and maintains the asymmetric distribution of LPS. The LPS transporter is composed of seven proteins, LptA – LptG, which localize between inner and outer membranes. The LptA protein consists of a β-sheet curved to adopt a taco shape whose inner surface is lined by hydrophobic residues. Several LptA proteins linked together head-to-tail form a 21 nm-long hydrophobic bridge across the intra-membrane space. The bridge accommodates the hydrophobic tail of LPS, enabling the movement of LPS between the inner and outer membrane. Other Lpt proteins in the complex mediate LPS extraction, insertion, and transfer between membrane leaflets (Wong et al., 2019). The complex utilizes two ATP hydrolysis steps to provide energy, driving LPS against a gradient. The entire LPS transfer bridge system is critical for maintaining the asymmetrical distribution of LPS in *E. coli* (Okuda, Freinkman, & Kahne, 2012).

Chorein-N domain protein family

Together with our collaborators, our lab recently discovered that large proteins that have a chorein-N motif belong to a novel family of lipid transport proteins. The chorein-N motif is a ~120 amino acid sequence at the N-terminus of these proteins. Three major proteins have been identified belonging to this family: VPS13 (Vacuolar protein sorting-associated protein 13) (Ueno et al., 2001), ATG2 (autophagy-related protein 2) (Gomez-Sanchez et al., 2018), and SHIP164 (Syntaxin 6 Habc‐interacting protein of 164 kDa) (Otto, Razi, Morvan, Stenner, & Tooze, 2010). Several bacterial proteins may also belong to this family based on bioinformatics studies (Levine, 2019). VPS13 and ATG2 are the best-studied members of this family. ATG2 plays a critical role in the early steps of autophagy, and VPS13 is of high interest because dysfunction in any four human genes VPS13 A-D (Velayos-Baeza, Vettori, Copley, Dobson-Stone, & Monaco, 2004) lead to severe neurological disorders, including chorea-acanthocytosis, Cohen syndrome, an early-onset form of Parkinson’s disease, and ataxia (Lesage et al., 2016; Rampoldi et al., 2001; Seifert et al., 2011; Seong et al., 2018).

VPS13 was first identified via yeast genetics, where a VPS13 mutation strain was found to bypass ERMES deficiency (Lang, John Peter, Walter, & Kornmann, 2015). Since ERMES is not conserved in metazoa, VPS13 was hypothesized to substitute for ERMES in higher eukaryotes. VPS13 has a PH-DH domain at the C-terminus that is proposed to mediate interaction with membranes (Kumar et al., 2018). Upstream of the PH-DH domain is a WD40-like domain. In yeast, this domain has been shown to interact with PxP motifs present in organellar receptor proteins, and likely also functions in VPS13 localization to particular contact sites (Bean et al., 2018). A small segment at the N-terminus that includes the chorein-N motif (~10% of the whole protein), $\text{VPS13}_{\text{crystal}}$, forms a scoop-like structure with the entire inner surface lined with hydrophobic residues. A longer fragment of the N-terminus of VPS13 (VPS13α) can bind more lipids compared with $\text{VPS13}_{\text{crystal}}$, suggesting that the complete lipid transfer module extends beyond the crystallized fragment. Interestingly, VPS13α purified from a human cell line was able to bind tens of lipids per molecule, as quantified by mass spectrometry (Kumar et al., 2018), versus previously identified lipid transfer modules that typically bind 1-2 lipids. These findings suggest that VPS13 differs from conventional shuttle-like lipid transfer proteins and instead might utilize a bridge-like mechanism similar to the LPS transporter. To test this hypothesis, I combined structural and biochemical studies to investigate the molecular function of VPS13.

The autophagy protein ATG2 is required for the growth of autophagosome membranes (Gomez-Sanchez et al., 2018). ATG2 has an N-terminal chorein-N motif and a C-terminal PH-DH domain, similar to VPS13. While ATG2 does not have a WD40-like domain, it interacts with WD40 proteins, including Atg18 in yeast and the WIPI proteins in mammals (Kotani, Kirisako, Koizumi, Ohsumi, & Nakatogawa, 2018; Zheng et al., 2017). The N-terminal portion of ATG2 adopts a scoop-like fold similar to VPS13, with the entire inner surface lined with hydrophobic residues (Osawa et al., 2019). In both VPS13 and ATG2, the chorein-N motif is followed by mostly β-strand sequences, and low resolution cryo-EM studies suggest, intriguingly, that these fold into a taco shape that might function in lipid transport by the bridge-like mechanism (Valverde et al., 2019). Such a structural feature can mediate lipid transfer *in vitro* and is critical for the expansion of the autophagosome membrane *in vivo* (Valverde et al., 2019). Localizing to different MCSs, VPS13 and ATG2 have high similarity structurally and functionally.

In the first part of my thesis work, I showed by cryo-EM that there is a hydrophobic channel in VPS13, at least 16nm long, strongly supporting that proteins from this family could function as lipid transfer bridges. The structure raised several questions regarding the molecular mechanism of lipid transfer bridges. How is the directionality of bulk lipid flow determined, and what provides the energy for driving lipid flow?

A more detailed understanding as to the mechanisms underlying protein-mediated lipid transfer, especially for bridge-like LTP's, is still lacking. Limitations in technology make it difficult to trace the entire process of lipid extraction, lipid flow through the hydrophobic conduit, and lipid insertion. However, it possible to speculate about some critical steps. It not hard to understand that lipid transfer proteins decrease the activation energy of the lipid extraction process by providing a hydrophobic environment. However, the energy provided by LTPs is not enough. (Moser von Filseck, Vanni, Mesmin, Antonny, & Drin, 2015). The biophysical properties of donor membranes also affect lipid desorption and lipid delivery. The regions of ER that form close contacts with other organelles contain specialized lipids compositions and thus differ in membrane properties such as lipid packing, curvature, and tension (King, Sengupta, Seo, & Lippincott-Schwartz, 2020). It is intriguing to speculate that the properties of the membrane are regulated by integral and peripheral membrane proteins. VPS13 is recruited to membranes via binding with several adaptor proteins (Bean et al., 2018; Kumar et al., 2018). Little is known about the functions of these adaptor proteins besides tethering LTPs. It has been speculated that protein adaptors are required to destabilize donor membranes, making it easy for lipid desorption (Petrungaro & Kornmann, 2019), and to scramble lipids to the inner leaflet at acceptor membranes to release tension on the outer leaflet after receiving bulk lipids. Indeed, several recent studies have demonstrated that ATG2 interacts directly with ATG9 (Guardia et al., 2020), and that ATG9 functions as a scramblase to facilitate autophagosome inner leaflet membrane expansion (Maeda et al., 2020; Matoba et al., 2020). Moreover, reminiscent of the LPS transporter, lipid transfer bridges might acquire energy from the hydrolysis of ATP. However, our understanding of this process is still limited and the investigation of interacting partners is needed.

Chapter 1.3 Phosphatidylinositol and phosphoinositide

Overview of signaling function

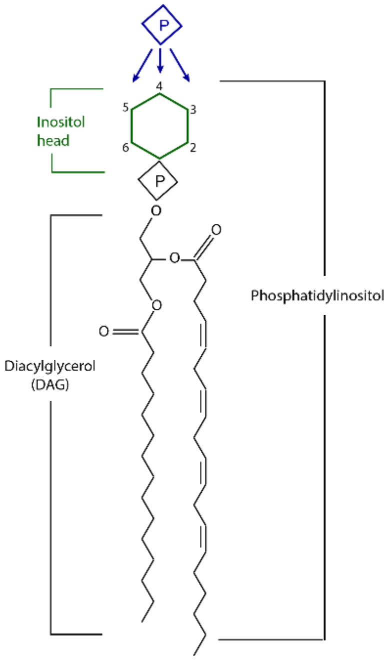

Figure 1.3: Overall structure of Phosphatidylinositol

Phosphoinositides are low-abundance but essential signaling lipids. They are derived from PI, which is synthesized in the ER and then redistributed to other organelles either via vesicular trafficking or LTPs. At different organelles, PI is phosphorylated at its 3,4, or 5 positions on the inositol ring, resulting in the production of seven phosphoinositides: PI(3)P, PI(4)P, PI(5)P, PI(3,4)P$_2$,

$PI(3,5)P_2$, $PI(4,5)P_2$, and $PI(3,4,5)P_3$ (Figure 1.3). These phosphoinositides are distributed unevenly at subcellular membranes due to modification by lipid kinases and phosphatases resident at different compartments. PI(4)P is the signature phosphoinositide on the Golgi apparatus, while the derivatives $PI(4,5)P_2$, $PI(3,4)P_2$, and $PI(3,4,5)P_3$ mainly reside at the PM. PI(3)P and $PI(3,5)P_2$ are enriched at, and critical for the biology of, endo-lysosomal membranes. Phosphoinositides recruit specific effector proteins to their organelles at specific times. The PI effectors, in turn, regulate the activity of the cytoskeleton, membrane contact sites, and ion channels, and control signaling pathways (Schink, Tan, & Stenmark, 2016) (Di Paolo & De Camilli, 2006; Jin, Lang, & Weisman, 2016).

Chapter 1.3.1 $PI(3,5)P_2$ – phenotype and function, synthesis

$PI(3,5)P_2$ is the least abundant phosphoinositide, accounting for only 0.05% - 0.1% of total PIPs, and localizes to the endo-lysosomal system. It regulates many processes, including lysosomal ion homeostasis, lysosome acidification, retrograde trafficking between the Golgi and lysosomes, membrane fission and fusion, autophagy (Hasegawa, Strunk, & Weisman, 2017), and viral replication (Qiu et al., 2018). $PI(3,5)P_2$ levels are highly dynamic in response to stimuli, such as insulin or growth factors in human cells, or hyperosmotic shock in yeast and plant cells (Dove et al., 1997). $PI(3,5)P_2$ levels are correlated with endo-lysosomal size in human and vacuolar compartment sizes in yeast. (Gary, Wurmser, Bonangelino, Weisman, & Emr, 1998; Ikonomov, Sbrissa, & Shisheva, 2001). In humans, $PI(3,5)P_2$ mis-regulation causes developmental disorders, including

Charcot-Marie-Tooth syndrome type 4J and forms of amyotrophic lateral sclerosis (Chow et al., 2009; Chow et al., 2007).

Chapter 1.3.2 regulation of PI(3,5)P_2 level

In yeast, PI(3,5)P_2 levels increase 20-fold within 5 minutes in response to hyperosmotic shock (Duex, Nau, Kauffman, & Weisman, 2006), resulting in activation of upstream effectors. Such a fast response to stimuli indicates that levels of PI(3,5)P_2 are tightly regulated. PI(3,5)P_2 is synthesized solely from PI3P by the lipid kinase PIKfyve. PIKfyve has an FYVE domain at its N-terminus, which recognizes PI3P at endo-lysosomes and localizes PIKfyve, a CCT (chaperone-containing TCP1) domain, and a CCR (conserved cysteine-rich) domain with unknown function. The kinase domain is at the very C-terminus. All the domains are conserved across eukaryotes, suggesting conserved mechanisms of action, although little was known about the domain arrangement in the context of full-length PIKfyve (Jin et al., 2016). Turnover of PI(3,5)P_2 is catalyzed by Fig4, which contains a phosphatase with a Sac homology domain. Paradoxically, the proteins PIKfyve and Fig4, although catalyzing antagonistic reactions, exist in a single complex together with the scaffolding protein Vac14 (Botelho, Efe, Teis, & Emr, 2008). It was long unclear how the activities of PIKfyve and Fig4 are regulated within the complex to prevent futile hydrolysis of ATP. Further, while Fig4 catalyzes the dephosphorylation of PI(3,5)P_2, deletion of Fig4 causes defects in the upregulation of PI(3,5)P_2 in response to hyperosmotic shock in yeast (Duex et al., 2006), suggesting that PIKfyve might require Fig4 for activity.

In the second part of my thesis work, we found that the PIKfyve complex comprises five copies of the scaffolding protein Vac14 and one copy each of the PIKfyve and Fig4. In the ternary complex, Fig4 is active as a lipid phosphatase, while PIKfyve cannot access membrane-incorporated phosphoinositides due to conformational constraints. The phosphoinositide-directed activities of both PIKfyve and Fig4 are regulated by protein-directed activities. In detail, PIKfyve was previously reported to also act as a protein kinase, and its autophosphorylation was found to repress its lipid kinase activity (Sbrissa, Ikonomov, & Shisheva, 2000). We found that its autophosphorylation stimulates Fig4 lipid phosphatase activity. Further, we found that in addition to its role as a lipid phosphatase, Fig4 is also a protein phosphatase acting on PIKfyve to stimulate its lipid kinase activity. This explains why catalytically active Fig4 is required for maximal $PI(3,5)P_2$ production *in vivo*. Our work greatly advances the knowledge of the overall architecture and regulatory mechanism of the PIKfyve complex. However, we were unable to capture other conformations of the PIKfyve complex, which should exist as indicated by our biochemistry assay. Additionally, our work was in the context of purified PIKfyve complex that lacked the participation of other interacting partners as it normally occurs *in vivo*. Further investigations of the PIKfyve complex in a more biologically relevant context will advance our knowledge of lysosomal membrane biology.

Reference

AhYoung, A. P., Jiang, J., Zhang, J., Khoi Dang, X., Loo, J. A., Zhou, Z. H., & Egea, P. F. (2015). Conserved SMP domains of the ERMES complex bind phospholipids and mediate tether assembly. *Proc Natl Acad Sci U S A, 112*(25), E3179-3188. doi: 10.1073/pnas.1422363112

AhYoung, A. P., Lu, B., Cascio, D., & Egea, P. F. (2017). Crystal structure of Mdm12 and combinatorial reconstitution of Mdm12/Mmm1 ERMES complexes for structural studies. *Biochem Biophys Res Commun, 488*(1), 129-135. doi: 10.1016/j.bbrc.2017.05.021

Balla, T. (2013). Phosphoinositides: tiny lipids with giant impact on cell regulation. *Physiol Rev, 93*(3), 1019-1137. doi: 10.1152/physrev.00028.2012

Bean, B. D. M., Dziurdzik, S. K., Kolehmainen, K. L., Fowler, C. M. S., Kwong, W. K., Grad, L. I., . . . Conibear, E. (2018). Competitive organelle-specific adaptors recruit Vps13 to membrane contact sites. *J Cell Biol, 217*(10), 3593-3607. doi: 10.1083/jcb.201804111

Bernhard, W., & Rouiller, C. (1956). Close topographical relationship between mitochondria and ergastoplasm of liver cells in a definite phase of cellular activity. *J Biophys Biochem Cytol, 2*(4 Suppl), 73-78. doi: 10.1083/jcb.2.4.73

Botelho, R. J., Efe, J. A., Teis, D., & Emr, S. D. (2008). Assembly of a Fab1 phosphoinositide kinase signaling complex requires the Fig4 phosphoinositide phosphatase. *Molecular Biology of the Cell, 19*(10), 4273-4286. doi: 10.1091/mbc.E08-04-0405

Chernomordik, L. V., Zimmerberg, J., & Kozlov, M. M. (2006). Membranes of the world unite! *J Cell Biol, 175*(2), 201-207. doi: 10.1083/jcb.200607083

Chow, C. Y., Landers, J. E., Bergren, S. K., Sapp, P. C., Grant, A. E., Jones, J. M., . . . Meisler, M. H. (2009). Deleterious variants of FIG4, a phosphoinositide phosphatase, in patients with ALS. *Am J Hum Genet, 84*(1), 85-88. doi: 10.1016/j.ajhg.2008.12.010

Chow, C. Y., Zhang, Y., Dowling, J. J., Jin, N., Adamska, M., Shiga, K., . . . Meisler, M. H. (2007). Mutation of FIG4 causes neurodegeneration in the pale tremor mouse and patients with CMT4J. *Nature, 448*(7149), 68-72. doi: 10.1038/nature05876

Cockcroft, S. (2012). The diverse functions of phosphatidylinositol transfer proteins. *Curr Top Microbiol Immunol, 362*, 185-208. doi: 10.1007/978-94-007-5025-8_9

Di Paolo, G., & De Camilli, P. (2006). Phosphoinositides in cell regulation and membrane dynamics. *Nature, 443*(7112), 651-657. doi: 10.1038/nature05185

Dove, S. K., Cooke, F. T., Douglas, M. R., Sayers, L. G., Parker, P. J., & Michell, R. H. (1997). Osmotic stress activates phosphatidylinositol-3,5-bisphosphate synthesis. *Nature, 390*(6656), 187-192. doi: 10.1038/36613

Dowhan, W. (1997). Molecular basis for membrane phospholipid diversity: why are there so many lipids? *Annu Rev Biochem, 66*, 199-232. doi: 10.1146/annurev.biochem.66.1.199

Duex, J. E., Nau, J. J., Kauffman, E. J., & Weisman, L. S. (2006). Phosphoinositide 5-phosphatase Fig 4p is required for both acute rise and subsequent fall in stress-induced phosphatidylinositol 3,5-bisphosphate levels. *Eukaryot Cell, 5*(4), 723-731. doi: 10.1128/EC.5.4.723-731.2006

Eden, E. R., White, I. J., Tsapara, A., & Futter, C. E. (2010). Membrane contacts between endosomes and ER provide sites for PTP1B-epidermal growth factor receptor interaction. *Nature Cell Biology, 12*(3), 267-272. doi: 10.1038/ncb2026

Eisenberg-Bord, M., Shai, N., Schuldiner, M., & Bohnert, M. (2016). A Tether Is a Tether Is a Tether: Tethering at Membrane Contact Sites. *Dev Cell, 39*(4), 395-409. doi: 10.1016/j.devcel.2016.10.022

Friedman, J. R., Lackner, L. L., West, M., DiBenedetto, J. R., Nunnari, J., & Voeltz, G. K. (2011). ER tubules mark sites of mitochondrial division. *Science, 334*(6054), 358-362. doi: 10.1126/science.1207385

Frolov, V. A., Shnyrova, A. V., & Zimmerberg, J. (2011). Lipid polymorphisms and membrane shape. *Cold Spring Harb Perspect Biol, 3*(11), a004747. doi: 10.1101/cshperspect.a004747

Gary, J. D., Wurmser, A. E., Bonangelino, C. J., Weisman, L. S., & Emr, S. D. (1998). Fab1p is essential for PtdIns(3)P 5-kinase activity and the maintenance of vacuolar size and membrane homeostasis. *J Cell Biol, 143*(1), 65-79. doi: 10.1083/jcb.143.1.65

Gomez-Sanchez, R., Rose, J., Guimaraes, R., Mari, M., Papinski, D., Rieter, E., . . . Reggiori, F. (2018). Atg9 establishes Atg2-dependent contact sites between the endoplasmic reticulum and phagophores. *J Cell Biol, 217*(8), 2743-2763. doi: 10.1083/jcb.201710116

Guardia, C. M., Tan, X. F., Lian, T., Rana, M. S., Zhou, W., Christenson, E. T., . . . Banerjee, A. (2020). Structure of Human ATG9A, the Only Transmembrane Protein of the Core Autophagy Machinery. *Cell Rep, 31*(13), 107837. doi: 10.1016/j.celrep.2020.107837

Harayama, T., & Riezman, H. (2018). Understanding the diversity of membrane lipid composition. *Nat Rev Mol Cell Biol, 19*(5), 281-296. doi: 10.1038/nrm.2017.138

Hasegawa, J., Strunk, B. S., & Weisman, L. S. (2017). PI5P and PI(3,5)P2: Minor, but Essential Phosphoinositides. *Cell Struct Funct, 42*(1), 49-60. doi: 10.1247/csf.17003

Holthuis, J. C., & Menon, A. K. (2014). Lipid landscapes and pipelines in membrane homeostasis. *Nature, 510*(7503), 48-57. doi: 10.1038/nature13474

Hsuan, J., & Cockcroft, S. (2001). The PITP family of phosphatidylinositol transfer proteins. *Genome Biol, 2*(9), REVIEWS3011. doi: 10.1186/gb-2001-2-9-reviews3011

Hynynen, R., Suchanek, M., Spandl, J., Back, N., Thiele, C., & Olkkonen, V. M. (2009). OSBP-related protein 2 is a sterol receptor on lipid droplets that regulates the metabolism of neutral lipids. *J Lipid Res, 50*(7), 1305-1315. doi: 10.1194/jlr.M800661-JLR200

Ikonomov, O. C., Sbrissa, D., & Shisheva, A. (2001). Mammalian cell morphology and endocytic membrane homeostasis require enzymatically active phosphoinositide 5-kinase PIKfyve. *J Biol Chem, 276*(28), 26141-26147. doi: 10.1074/jbc.M101722200

Jeong, H., Park, J., Jun, Y., & Lee, C. (2017). Crystal structures of Mmm1 and Mdm12-Mmm1 reveal mechanistic insight into phospholipid trafficking at ER-mitochondria contact sites. *Proc Natl Acad Sci U S A, 114*(45), E9502-E9511. doi: 10.1073/pnas.1715592114

Jin, N., Lang, M. J., & Weisman, L. S. (2016). Phosphatidylinositol 3,5-bisphosphate: regulation of cellular events in space and time. *Biochem Soc Trans, 44*(1), 177-184. doi: 10.1042/BST20150174

Kawamoto, R. M., Brunschwig, J. P., Kim, K. C., & Caswell, A. H. (1986). Isolation, characterization, and localization of the spanning protein from skeletal muscle triads. *J Cell Biol, 103*(4), 1405-1414. doi: 10.1083/jcb.103.4.1405

Kawano, S., Tamura, Y., Kojima, R., Bala, S., Asai, E., Michel, A. H., . . . Endo, T. (2018). Structure-function insights into direct lipid transfer between membranes by Mmm1-Mdm12 of ERMES. *J Cell Biol, 217*(3), 959-974. doi: 10.1083/jcb.201704119

Kentala, H., Weber-Boyvat, M., & Olkkonen, V. M. (2016). OSBP-Related Protein Family: Mediators of Lipid Transport and Signaling at Membrane Contact Sites. *Int Rev Cell Mol Biol, 321*, 299-340. doi: 10.1016/bs.ircmb.2015.09.006

King, C., Sengupta, P., Seo, A. Y., & Lippincott-Schwartz, J. (2020). ER membranes exhibit phase behavior at sites of organelle contact. *Proc Natl Acad Sci U S A, 117*(13), 7225-7235. doi: 10.1073/pnas.1910854117

Knoblach, B., & Rachubinski, R. A. (2015). Transport and retention mechanisms govern lipid droplet inheritance in Saccharomyces cerevisiae. *Traffic, 16*(3), 298-309. doi: 10.1111/tra.12247

Kopec, K. O., Alva, V., & Lupas, A. N. (2010). Homology of SMP domains to the TULIP superfamily of lipid-binding proteins provides a structural basis for lipid exchange between ER and mitochondria. *Bioinformatics, 26*(16), 1927-1931. doi: 10.1093/bioinformatics/btq326

Kornmann, B., Osman, C., & Walter, P. (2011). The conserved GTPase Gem1 regulates endoplasmic reticulum-mitochondria connections. *Proc Natl Acad Sci U S A, 108*(34), 14151-14156. doi: 10.1073/pnas.1111314108

Kornmann, B. (2020). The endoplasmic reticulum-mitochondria encounter structure: coordinating lipid metabolism across membranes. Biol Chem, 401(6-7), 811-820. doi: 10.1515/hsz-2020-0102

Kotani, T., Kirisako, H., Koizumi, M., Ohsumi, Y., & Nakatogawa, H. (2018). The Atg2-Atg18 complex tethers pre-autophagosomal membranes to the endoplasmic reticulum for autophagosome formation. *Proc Natl Acad Sci U S A, 115*(41), 10363-10368. doi: 10.1073/pnas.1806727115

Kumar, N., Leonzino, M., Hancock-Cerutti, W., Horenkamp, F. A., Li, P., Lees, J. A., . . . De Camilli, P. (2018). VPS13A and VPS13C are lipid transport proteins differentially localized at ER contact sites. *J Cell Biol, 217*(10), 3625-3639. doi: 10.1083/jcb.201807019

Lang, A. B., John Peter, A. T., Walter, P., & Kornmann, B. (2015). ER-mitochondrial junctions can be bypassed by dominant mutations in the endosomal protein Vps13. *J Cell Biol, 210*(6), 883-890. doi: 10.1083/jcb.201502105

Lee, A. G. (2004). How lipids affect the activities of integral membrane proteins. *Biochim Biophys Acta, 1666*(1-2), 62-87. doi: 10.1016/j.bbamem.2004.05.012

Lees, J. A., Messa, M., Sun, E. W., Wheeler, H., Torta, F., Wenk, M. R., . . . Reinisch, K. M. (2017). Lipid transport by TMEM24 at ER-plasma membrane contacts regulates pulsatile insulin secretion. *Science, 355*(6326). doi: 10.1126/science.aah6171

Lesage, S., Drouet, V., Majounie, E., Deramecourt, V., Jacoupy, M., Nicolas, A., . . . International Parkinson's Disease Genomics, C. (2016). Loss of VPS13C Function in Autosomal-Recessive Parkinsonism Causes Mitochondrial Dysfunction and Increases PINK1/Parkin-Dependent Mitophagy. *Am J Hum Genet, 98*(3), 500-513. doi: 10.1016/j.ajhg.2016.01.014

Levine, T. P. (2019). Remote homology searches identify bacterial homologues of eukaryotic lipid transfer proteins, including Chorein-N domains in TamB and AsmA and Mdm31p. *BMC Mol Cell Biol, 20*(1), 43. doi: 10.1186/s12860-019-0226-z

Lewis, S. C., Uchiyama, L. F., & Nunnari, J. (2016). ER-mitochondria contacts couple mtDNA synthesis with mitochondrial division in human cells. *Science, 353*(6296), aaf5549. doi: 10.1126/science.aaf5549

Maeda, S., Yamamoto, H., Kinch, L. N., Garza, C. M., Takahashi, S., Otomo, C., . . . Otomo, T. (2020). Structure, lipid scrambling activity and role in autophagosome formation of ATG9A. *Nature Structural & Molecular Biology, 27*(12), 1194-1201. doi: 10.1038/s41594-020-00520-2

Matoba, K., Kotani, T., Tsutsumi, A., Tsuji, T., Mori, T., Noshiro, D., . . . Noda, N. N. (2020). Atg9 is a lipid scramblase that mediates autophagosomal membrane expansion. *Nature Structural & Molecular Biology, 27*(12), 1185-1193. doi: 10.1038/s41594-020-00518-w

McLean, L. R., & Phillips, M. C. (1984). Kinetics of phosphatidylcholine and lysophosphatidylcholine exchange between unilamellar vesicles. *Biochemistry, 23*(20), 4624-4630. doi: 10.1021/bi00315a017

Mesmin, B., Bigay, J., Moser von Filseck, J., Lacas-Gervais, S., Drin, G., & Antonny, B. (2013). A four-step cycle driven by PI(4)P hydrolysis directs sterol/PI(4)P exchange by the ER-Golgi tether OSBP. *Cell, 155*(4), 830-843. doi: 10.1016/j.cell.2013.09.056

Moser von Filseck, J., Vanni, S., Mesmin, B., Antonny, B., & Drin, G. (2015). A phosphatidylinositol-4-phosphate powered exchange mechanism to create a lipid gradient between membranes. *Nat Commun, 6*, 6671. doi: 10.1038/ncomms7671

Muik, M., Fahrner, M., Schindl, R., Stathopulos, P., Frischauf, I., Derler, I., . . . Romanin, C. (2011). STIM1 couples to ORAI1 via an intramolecular transition into an extended conformation. *EMBO J, 30*(9), 1678-1689. doi: 10.1038/emboj.2011.79

Okuda, S., Freinkman, E., & Kahne, D. (2012). Cytoplasmic ATP hydrolysis powers transport of lipopolysaccharide across the periplasm in E. coli. *Science, 338*(6111), 1214-1217. doi: 10.1126/science.1228984

Olkkonen, V. M. (2015). OSBP-Related Protein Family in Lipid Transport Over Membrane Contact Sites. *Lipid Insights, 8*(Suppl 1), 1-9. doi: 10.4137/LPI.S31726

Osawa, T., Kotani, T., Kawaoka, T., Hirata, E., Suzuki, K., Nakatogawa, H., . . . Noda, N. N. (2019). Atg2 mediates direct lipid transfer between membranes for autophagosome formation. *Nature Structural & Molecular Biology, 26*(4), 281-288. doi: 10.1038/s41594-019-0203-4

Otto, G. P., Razi, M., Morvan, J., Stenner, F., & Tooze, S. A. (2010). A novel syntaxin 6-interacting protein, SHIP164, regulates syntaxin 6-dependent sorting from early endosomes. *Traffic, 11*(5), 688-705. doi: 10.1111/j.1600-0854.2010.01049.x

Pan, X., Roberts, P., Chen, Y., Kvam, E., Shulga, N., Huang, K., . . . Goldfarb, D. S. (2000). Nucleus-vacuole junctions in Saccharomyces cerevisiae are formed through the direct interaction of Vac8p with Nvj1p. *Molecular Biology of the Cell, 11*(7), 2445-2457. doi: 10.1091/mbc.11.7.2445

Petrungaro, C., & Kornmann, B. (2019). Lipid exchange at ER-mitochondria contact sites: a puzzle falling into place with quite a few pieces missing. *Curr Opin Cell Biol, 57*, 71-76. doi: 10.1016/j.ceb.2018.11.005

Qiu, S., Leung, A., Bo, Y., Kozak, R. A., Anand, S. P., Warkentin, C., . . . Cote, M. (2018). Ebola virus requires phosphatidylinositol (3,5) bisphosphate production for efficient viral entry. *Virology, 513*, 17-28. doi: 10.1016/j.virol.2017.09.028

Radauer, C., Lackner, P., & Breiteneder, H. (2008). The Bet v 1 fold: an ancient, versatile scaffold for binding of large, hydrophobic ligands. *BMC Evol Biol, 8*, 286. doi: 10.1186/1471-2148-8-286

Rampoldi, L., Dobson-Stone, C., Rubio, J. P., Danek, A., Chalmers, R. M., Wood, N. W., . . . Monaco, A. P. (2001). A conserved sorting-associated protein is mutant in chorea-acanthocytosis. *Nat Genet, 28*(2), 119-120. doi: 10.1038/88821

Reinisch, K. M., & De Camilli, P. (2016). SMP-domain proteins at membrane contact sites: Structure and function. *Biochim Biophys Acta, 1861*(8 Pt B), 924-927. doi: 10.1016/j.bbalip.2015.12.003

Rocha, N., Kuijl, C., van der Kant, R., Janssen, L., Houben, D., Janssen, H., . . . Neefjes, J. (2009). Cholesterol sensor ORP1L contacts the ER protein VAP to control Rab7-RILP-p150 Glued and late endosome positioning. *J Cell Biol, 185*(7), 1209-1225. doi: 10.1083/jcb.200811005

Saheki, Y., Bian, X., Schauder, C. M., Sawaki, Y., Surma, M. A., Klose, C., . . . De Camilli, P. (2016). Control of plasma membrane lipid homeostasis by the extended synaptotagmins. *Nature Cell Biology, 18*(5), 504-515. doi: 10.1038/ncb3339

Saheki, Y., & De Camilli, P. (2017). Endoplasmic Reticulum-Plasma Membrane Contact Sites. *Annu Rev Biochem, 86*, 659-684. doi: 10.1146/annurev-biochem-061516-044932

Sbrissa, D., Ikonomov, O. C., & Shisheva, A. (2000). PIKfyve lipid kinase is a protein kinase: downregulation of 5'-phosphoinositide product formation by autophosphorylation. Biochemistry, 39(51), 15980-15989. doi: 10.1021/bi001897f

Schauder, C. M., Wu, X., Saheki, Y., Narayanaswamy, P., Torta, F., Wenk, M. R., . . . Reinisch, K. M. (2014). Structure of a lipid-bound extended synaptotagmin indicates a role in lipid transfer. *Nature, 510*(7506), 552-555. doi: 10.1038/nature13269

Schink, K. O., Tan, K. W., & Stenmark, H. (2016). Phosphoinositides in Control of Membrane Dynamics. *Annu Rev Cell Dev Biol, 32*, 143-171. doi: 10.1146/annurev-cellbio-111315-125349

Schulz, T. A., & Creutz, C. E. (2004). The tricalbin C2 domains: lipid-binding properties of a novel, synaptotagmin-like yeast protein family. *Biochemistry, 43*(13), 3987-3995. doi: 10.1021/bi036082w

Scorrano, L., De Matteis, M. A., Emr, S., Giordano, F., Hajnoczky, G., Kornmann, B., . . . Schuldiner, M. (2019). Coming together to define membrane contact sites. *Nat Commun, 10*(1), 1287. doi: 10.1038/s41467-019-09253-3

Seifert, W., Kuhnisch, J., Maritzen, T., Horn, D., Haucke, V., & Hennies, H. C. (2011). Cohen syndrome-associated protein, COH1, is a novel, giant Golgi matrix protein required for Golgi integrity. *J Biol Chem, 286*(43), 37665-37675. doi: 10.1074/jbc.M111.267971

Seong, E., Insolera, R., Dulovic, M., Kamsteeg, E. J., Trinh, J., Bruggemann, N., . . . Burmeister, M. (2018). Mutations in VPS13D lead to a new recessive ataxia with spasticity and mitochondrial defects. *Ann Neurol, 83*(6), 1075-1088. doi: 10.1002/ana.25220

Shevchenko, A., & Simons, K. (2010). Lipidomics: coming to grips with lipid diversity. *Nat Rev Mol Cell Biol, 11*(8), 593-598. doi: 10.1038/nrm2934

Sogo, L. F., & Yaffe, M. P. (1994). Regulation of mitochondrial morphology and inheritance by Mdm10p, a protein of the mitochondrial outer membrane. *J Cell Biol, 126*(6), 1361-1373. doi: 10.1083/jcb.126.6.1361

Stathopulos, P. B., Zheng, L., Li, G. Y., Plevin, M. J., & Ikura, M. (2008). Structural and mechanistic insights into STIM1-mediated initiation of store-operated calcium entry. *Cell, 135*(1), 110-122. doi: 10.1016/j.cell.2008.08.006

Stefan, C. J., Manford, A. G., Baird, D., Yamada-Hanff, J., Mao, Y., & Emr, S. D. (2011). Osh proteins regulate phosphoinositide metabolism at ER-plasma membrane contact sites. *Cell, 144*(3), 389-401. doi: 10.1016/j.cell.2010.12.034

Stroud, D. A., Oeljeklaus, S., Wiese, S., Bohnert, M., Lewandrowski, U., Sickmann, A., . . . Wiedemann, N. (2011). Composition and topology of the endoplasmic reticulum-mitochondria encounter structure. *J Mol Biol, 413*(4), 743-750. doi: 10.1016/j.jmb.2011.09.012

Ueno, S., Maruki, Y., Nakamura, M., Tomemori, Y., Kamae, K., Tanabe, H., . . . Sano, A. (2001). The gene encoding a newly discovered protein, chorein, is mutated in chorea-acanthocytosis. *Nat Genet, 28*(2), 121-122. doi: 10.1038/88825

Valverde, D. P., Yu, S., Boggavarapu, V., Kumar, N., Lees, J. A., Walz, T., . . . Melia, T. J. (2019). ATG2 transports lipids to promote autophagosome biogenesis. *J Cell Biol, 218*(6), 1787-1798. doi: 10.1083/jcb.201811139

van Meer, G., & de Kroon, A. I. (2011). Lipid map of the mammalian cell. *J Cell Sci, 124*(Pt 1), 5-8. doi: 10.1242/jcs.071233

van Meer, G., Voelker, D. R., & Feigenson, G. W. (2008). Membrane lipids: where they are and how they behave. *Nat Rev Mol Cell Biol, 9*(2), 112-124. doi: 10.1038/nrm2330

Vance, J. E. (1990). Phospholipid synthesis in a membrane fraction associated with mitochondria. *J Biol Chem, 265*(13), 7248-7256.

Velayos-Baeza, A., Vettori, A., Copley, R. R., Dobson-Stone, C., & Monaco, A. P. (2004). Analysis of the human VPS13 gene family. *Genomics, 84*(3), 536-549. doi: 10.1016/j.ygeno.2004.04.012

Wong, L. H., Gatta, A. T., & Levine, T. P. (2019). Lipid transfer proteins: the lipid commute via shuttles, bridges and tubes. *Nat Rev Mol Cell Biol, 20*(2), 85-101. doi: 10.1038/s41580-018-0071-5

Yang, Y., Lee, M., & Fairn, G. D. (2018). Phospholipid subcellular localization and dynamics. *J Biol Chem, 293*(17), 6230-6240. doi: 10.1074/jbc.R117.000582

Zheng, J. X., Li, Y., Ding, Y. H., Liu, J. J., Zhang, M. J., Dong, M. Q., . . . Yu, L. (2017). Architecture of the ATG2B-WDR45 complex and an aromatic Y/HF motif crucial for complex formation. *Autophagy, 13*(11), 1870-1883. doi: 10.1080/15548627.2017.1359381

Chapter 2: VPS13 has a long groove that channels lipids at membrane contact site.

The work was previously published as “Li, P., Lees, J. A., Lusk, C. P., & Reinisch, K. M. (2020). Cryo-EM reconstruction of a VPS13 fragment reveals a long groove to channel lipids between membranes. *Journal of Cell Biology*, *219*(5).”

Author contributions: PL carried out all the experiments, with assistance from JAL in the cryo-EM studies and CPL in the functional assays. PL and KMR conceived of the study and designed the experiments with help from JAL and CPL, and KMR supervised the study and wrote the manuscript with input from all authors.

Abstract. A single particle cryo-EM reconstruction of a ~160 kDa N-terminal fragment of the lipid transport protein VPS13 reveals a ~160 Å long channel lined with hydrophobic residues suitable for solubilizing multiple lipid fatty acid moieties. The structure suggests that VPS13 and related proteins, like the autophagy protein ATG2, can act as bridges between organelle membranes to allow bulk lipid flow between organelles.

Introduction.

In eukaryotic cells, most membrane lipids are synthesized in the endoplasmic reticulum (ER), then distributed to other organelles. This occurs through vesicular trafficking or else via protein-mediated lipid transport at membrane contact sites, where two organelles are closely apposed. The eukaryotic lipid transport proteins characterized so far are thought mostly to act as shuttles that extract and solubilize lipids from the membrane of the donating organelle, ferry these through the cytosol, then deposit them in the membrane of the acceptor organelle (Wong et al., 2019). Typically, these proteins comprise domains resembling lidded tea cups, each with a hydrophobic cavity that accommodates one or two lipid molecules. Here we describe a different architecture for large proteins in the VPS13 family of lipid transporters, whose features suggest that these proteins may instead function as bridges along which bulk lipid can traverse the cytosolic space between membranes. The VPS13 proteins themselves, present in all eukaryotes, are of intense biomedical interest because their loss-of-function mutations give rise to severe neurodegenerative diseases, including chorea acanthocytosis and an early onset version of Parkinson’s disease (Lesage et al., 2016; Rampoldi et al., 2001; Ueno et al., 2001). In metazoa, they are proposed to mediate lipid exchange between the ER and mitochondria, the endo/lysosomal system, or lipid droplets (Kumar et al., 2018). In budding yeast, Vps13p plays a role in the biogenesis of the prospore (Park and Neiman, 2012), a double membrane structure that surrounds the four meiotic products during sporulation. Lipid transport by the VPS13-like protein ATG2 is required for the biogenesis of another double membrane structure, the autophagosome (Valverde et al., 2019).

Results and Discussion.

The lipid transport functionality of VPS13 resides in a ~200 kDa N-terminal portion rich in ß-strand structure, whereas its C-terminus is predicted to comprise a WD40 and a PH domain critical in targeting the protein to organelle contact sites (Bean et al., 2018; Kumar et al., 2018). To better understand how VPS13 mediates lipid transfer, we imaged an N-terminal fragment of *Chaetomium thermophilum* VPS13, $\text{VPS13}_{1\text{-}1390}$ comprising residues 1-1390, by single particle cryo-electron microscopy, to obtain a 3D reconstruction at a nominal resolution of 3.75 Å (Fig. 2.1). The ß-strands in $\text{VPS13}_{1\text{-}1390}$ form an extended sheet curved to resemble an open-ended basket, which is twisted by ~90° along its length. α-helices in the loops between strands trim a long edge of the basket and also assemble into a basket “handle”. Because the fragment lacks a protein core, so that most side chains and long loops connecting secondary structure elements are solvent exposed and poorly resolved, it has not been possible to confidently trace the polypeptide chain. We were able to assign a Cα trace for residues 650-830 to the middle portion of the basket (shaded blue region in Fig. 2.1B), which corresponds to higher resolution regions of the map. Moreover, we can definitively dock the crystal structure of the very N-terminus of the *C. thermophilum* protein, VPS13$_{1\text{-}335}$ comprising residues 1-335 (PDBID 6CBC) (Kumar et al., 2018), into density at one end of the basket (Fig. 1A, 2A). Two helical segments (residues 99-118, disordered in 6CBC, and 300-322) were repositioned with respect to the crystal structure to form part of the basket handle (Fig. 1A, 2A). The VPS131-335 fragment is shaped like a scoop, and its concave surface is lined exclusively with hydrophobic residues (Kumar et al., 2018). Docked into the EM reconstruction, this hydrophobic surface faces the basket interior. As in this smaller fragment, the remaining ß-strands in Vps13$_{1\text{-}1390}$ feature alternating hydrophobic and hydrophilic residues, and it is probable that as in the smaller fragment the hydrophobics will face the basket interior while the hydrophilics are solvent exposed. Thus, VPS13$_{1\text{-}1390}$ forms a long channel well suited for solubilizing, as reported before 5, tens of lipid fatty acid moieties. The hydrophilic headgroups of the lipids would extrude into solvent. An interesting feature of VPS13$_{1\text{-}1390}$ is its asymmetry along its longitudinal axis: the channel is approximately twice as wide at the end harboring Vps13$_{1\text{-}335}$ as at the other, where its width across (~12 Å from Cα to Cα) resembles that of a more typical lipid transport module. A 3D cryo-EM reconstruction of ATG2, determined at ~15 Å resolution, suggests that ATG2 has a long channel similar to that in VPS131-1390 (Valverde et al., 2019).

Like ATG2 (Chowdhury et al., 2018; Gomez-Sanchez et al., 2018; Kotani et al., 2018), VPS13 is proposed also to act as a tether, since its overexpression promotes the formation of more numerous and more extensive membrane contacts (Kumar et al., 2018; Lang et al., 2015). Via its C-terminal WD40 domain, VPS13 can interact with membrane associated proteins containing a proline-X-proline motif (Bean et al., 2018); and a FFAT motif in human VPS13A and VPS13C, which we would tentatively place in or near the "handle" in the $VPS13_{1-1390}$ reconstruction, interacts with the ER-anchored VAP protein (Kumar et al., 2018). This suggests that at contact sites VPS13 might be arranged with its length approximately normal to the membrane planes, so that lipids would access the hydrophobic cavity via its ends, one of which is formed by $VPS13_{1-335}$, then travel between membranes through the channel (Fig. 2.2B). In this "bridge" model, lipids move through the entire length of the channel, whereas in an alternative "shuttle" model, the lipids would be stationary within the channel as the protein carries them between membranes. If the "bridge" model is correct, then rendering a band within the VPS13 channel impassible to lipids, by replacing hydrophobic with hydrophilic residues unable to solubilize fatty acid moieties, should disrupt lipid transfer. If instead VPS13 acts as a shuttle, then lipid transport should be largely unaffected by the mutations, as most of the hydrophobic channel is unaltered and would retain the ability to bind lipids. Since VPS13 function is required for prospore formation in yeast (Park and Neiman, 2012), and strains lacking the protein fail to sporulate (Enyenihi and Saunders, 2003), we tested mutant versions of VPS13 for their ability to rescue sporulation in *vps13*α strains. In one mutant, guided by the crystal structure, we altered a band of residues at one end of the channel in the N-terminal portion of *S. cerevisiae* VPS13 (*vps13-mut1*: L64K/I80E/L87E/I162R/L185E/A192E/L217R/V269E/L275D/M293K/L300R; Fig. 1B, 2B-C). In a second mutant, based on the assignment for residues 650-830 in *C. thermophilum* VPS13, the alterations are in a band midway along $VPS13_{1-1390}$'s length (*vps13-mut2:* V690D/L692R/L694E/I715K/A717D/M720K/I722D/I761R/I768E/F790D/M796D/L798

R/V802E/I816R/G820D/L827E; Fig. 2.1B, Fig. 2.2B). The mutations do not interfere with folding as yeast VPS13$_{1-1350}$ constructs incorporating the mutations are monodisperse by negative stain electron microscopy, and the mutated constructs still bind lipids (Fig. S2.1). Further, GFP-tagged full length wild-type and mutant constructs are expressed in yeast and localize as expected (Lang et al., 2015) (Fig. 2.3A, S2.1). Consistent with the bridge model, we found that the inability of diploid *vps13*α cells to sporulate could only be rescued by introduction of plasmid-borne copies of VPS13, but not of *vps13-mut1* or *vps13-mut2*, even when expressed from high copy number (2 μm) vectors (Fig. 2.3B).

We and others had previously speculated that VPS13 and related proteins like ATG2 could harbor channels to facilitate the transfer of lipids between membranes (Kumar et al., 2018; Osawa et al., 2019; Valverde et al., 2019). Here we provide the first strong evidence for a continuous, hydrophobic channel in VPS13, and by analogy in ATG2, and a channel versus a shuttle lipid transfer mechanism. The size of the VPS13 lipid binding cavity and, hence, ability of these proteins to accommodate many lipids simultaneously suggests a role in bulk lipid transfer. Further, in the narrower, more C-terminal portions of the channel, lipids will be lined up one behind the other, indicating directional transport. Although the architecture of VPS13$_{1-1390}$ is distinct from that of other eukaryotic lipid transport modules, it broadly resembles bacterial lipopolysaccharide transporters, which feature a channel through which lipopolysaccharide travels from the inner to the outer membrane of Gram-negative bacteria (Owens et al., 2019). The bacterial channel also is a primarily ß-strand structure, though composed of multiple small subunits, and resembles an open-ended basket. Importantly, it is associated with biosynthetic machinery in the inner membrane that pumps lipopolysaccharide into the channel as it is produced, thus ensuring efficient, vectorial transfer. It is tempting to speculate that this bridge-like transfer mechanism is conserved in eukaryotes, with VPS13 and ATG2 similarly collaborating with the lipid biosynthetic machinery for effective bulk lipid transfer.

The density map has been deposited in the EMD databank www.emdatabank.org/ (accession no. EMD-21113).

Materials and Methods

Protein expression and purification. Vps13$_{1\text{-}1390}$, comprising residues 1-1390 from *C. thermophilum* Vps13, was cloned into a pCMV-10 vector containing an N-terminal 3XFLAG tag, and expressed using the Expi293 Expression System (Thermo Fisher Scientific, Table S1). Cells were harvested after 95 hours and resuspended in lysis buffer (50 mM HEPES, pH 7.8, 500 mM NaCl, 1 mM TCEP, and 5% glycerol supplemented with EDTA-free protease inhibitor tablet (Roche)). Cells were lysed by sonication and clarified via centrifugation at 27,216 g for 30 minutes. The protein was purified by batch binding with anti-FLAG M2 Affinity Gel (Sigma). The resin was washed three times with 5 bed volumes of lysis buffer. The washed resin was incubated overnight (about 15 hrs) with lysis buffer supplemented with 1 mM ATP and 2 mM $MgCl_2$ in a total volume of 10ml. The resin was washed three more times, with 10 bed volumes of lysis buffer and eluted with 0.25mg/ml of 3X FLAG peptide (APExBIO). The eluted protein was loaded onto a Superdex 200 10/300 column (GE Healthcare). The peak fractions were collected and concentrated by Amicon® Ultra-4 Centrifugal Filter Unit with 30 kDa MWCO. Protein at a concentration of 0.3mg/ml was used for CryoEM sample preparation.

Cryo sample preparation and data collection (Table S2.2)**.** For freezing EM grids, freshly purified Vps13$_{1-1390}$ was supplemented with 0.02% n-Octyl-β-D-Glucoside. 4 ul of sample was applied to Quantifoil R1.2/1.3 300 mesh copper grids after 30 s glow discharge. Grids were plunge-frozen in liquid ethane using an FEI Vitrobot Mark IV (Thermo Fisher Scientific) after blotting with a single blotting paper for 5 s at a blot force of -2 in 90% humidity at 4°C. Data collection was performed using an FEI Titan Krios G2 300 kV transmission electron microscope with K2 summit direct detection camera. For the first dataset, 1976 micrographs were collected in super-resolution mode at a magnification of 135,000k with 1.05Å/physical pixel with a total exposure of 8 s fractionated into 40 frames for a total dose of 50.4 $e^-/Å^2$ with a defocus range of 1.9 μm to 2.8 μm. For the second dataset, 970 micrographs were collected in super-resolution mode at a magnification of 135,000k with 1.05Å/physical pixel and a total exposure of 6.2 s fractionated into 31 frames for a total dose of 49.5 $e^-/ Å^2$ with a defocus range of 1.4 μm to 2.3 μm.

Image processing (Fig. S2.2, Table S2.2). A total of 2946 micrographs from two datasets was analyzed using RELION 3.0(Zivanov et al., 2018). Super-resolution micrograph movie frames were binned by a factor of 2 and divided into 5x5 patches for motion correction by MotionCor2 (Zheng et al., 2017). Contrast transfer function estimation was done by CTFFIND-4 (Rohou and Grigorieff, 2015). Vps13$_{1-1390}$ forms tail-to-tail dimers. Half of each dimer, corresponding to a monomer, was used for the 3D reconstruction. For the first dataset, 1029 particles were manually picked from micrographs and subjected to

2D classification (Fig. S2a). The two best 2D classes were used as references for auto-picking in RELION 3.0 (Zivanov et al., 2018), which yielded a total of 564503 particles, which were extracted using a box size of 250 x 250 pixels. For the second dataset, 506742 particles were auto-picked in RELION 3.0 (Zivanov et al., 2018) using the refined 3D map from the initial dataset to generate 2D projections as references. Particles were extracted using the same parameters as for the first dataset. For analyzing the first dataset, several rounds of 2D classification with 200 classes were used to remove ice and bad particles. An initial model was generated from 20,000 particles using stochastic gradient descent with C1 symmetry. A total of 391,836 particles were then put into 3D classification using the initial model as a reference. All the particles were classified into either three or four classes, and the best classes from these two jobs were selected separately. Particles that appeared in both classes were selected using a locally developed script and polished using Bayesian polishing in RELION 3.0 (Zivanov et al., 2018). After polishing and postprocessing, the resulting map, which was calculated from 61230 particles, had an estimated resolution of 4.23 Å. This map was used as a reference for 3D classification for the second dataset. Following Bayesian polishing, the best final refined map from the second dataset, based on 114134 particles, had a resolution of 3.9 Å. Polished particles from the two final maps were pooled and subjected to per-particle CTF refinement, as in (Wan et al., 2019; Yang et al., 2019), as implemented in RELION 3.0 (Zivanov et al., 2018). Final gold standard refinement and postprocessing were done with the resulting 175,364 particles, producing a map with an estimated resolution of 3.75 Å according to the FSC = 0.143 criterion. The map was sharpened during post-processing with a B-factor of -105.771. Local resolution estimation was performed using the RELION 3.0 (Zivanov et al., 2018) implementation.

The Vps13$_{1\text{-}335}$ crystal structure (6CBC) was docked into the map manually and fitted using UCSF Chimera (Pettersen et al., 2004). The "pseudotrace" interpreting the map in terms of secondary structure (in Fig. 2.1B) was built manually in Coot (Emsley et al., 2010).

Sporulation assay: Diploid *vps13Δ* cells were transformed with plasmids (low copy *CEN*/pRS413 or multi-copy 2μm/pRS423) GFP-tagged versions of *VPS13*, *vps13-mut1* and *vps13-mut2* under the control of the endogenous *VPS13* promoter and transferred to sporulation plates (Table S2.1). Sporulation efficiency was assessed by direct visualization of ascospores by light microscopy after 1, 2, and 3 days of incubation at 30 °C. In these constructs, GFP was inserted after residue 499 of the VPS13 sequence, where it is known not to interfere with VPS13 function (Lang et al., 2015). Residues in the VPS13 channel were made hydrophilic in *vps13-mut1* (L64K/I80E/L87E/I162R/L185E/A192E/L217R/V269E/L275D/M293K/L300R) and *vps13-mut2* (V690D/L692R/L694E/I715K/A717D/M720K/I722D/I761R/I768E/F790D/M796D/L798R/V802E/I816R/G820D/L827E). Coding sequences for fragments of the genome incorporating the mutations were purchased from Genscript and replaced the VPS13 WT sequence in the mutant constructs.

Fluorescence microscopy: Yeast expressing GFP-VPS13 from a plasmid was cultured in CSM-His media with 2% of glucose at 30°C. To assess the localization of GFP-VPS13 constructs, we used a wide-field DeltaVision microsope (Applied Precision/GE

Healthcare) fitted with a 100x, 1.4 NA objective (Olympus) and solid-state laser illumination. Images were acquired at 30°C using a CoolSnapHQ2 CCD camera (Photometrics) and deconvolved using the iterative algorithm in softWoRx (7.0.0; Applied Precision GE Healthcare).

Immunoprecipitation. Diploid *vps13α* cells were transformed with linearized integrating plasmids (pRS406 backbone) expressing GFP-tagged versions of VPS13, VPS13-mut1, VPS13-mut2 under the control of the *GAL1* promoter using standard lithium acetate transformation methods. Yeast colonies were then streaked on selection plates containing 2% galactose and GFP-expression and localization confirmed by microscopy. Selected clones were grown in 100 ml of YP (1% Yeast Extract, 2% Peptone) media with 2% Raffinose at 30°C. A final concentration of 2% galactose was added when the cultures reached OD600 of 0.5. For each strain, 2 grams of wet yeast pellet was resuspended with 15 ml of buffer (50 mM NaCl, 50 mM HEPES, pH 7.4, 0.1% Tween-20, 1 mM EDTA, 1 mM PMSF) supplemented with EDTA-free protease inhibitor cocktail (Roche). Yeast were lysed by vortexing with 5 g glass beads 20 times in 30-second pulses with 1-minute rests on ice in between, and the lysates were clarified via centrifugation at 27,216 x g for 20 minutes. The protein was captured by batch binding with GFP-Trap Agarose (Chromotek). The resin was washed three times with 5 bed volumes of buffer. The washed resin was incubated with 6x Laemmli gel loading buffer at 95°C for 10 minutes and proteins resolved on a 4% - 15% gradient native gel (Bio-Rad, #4568086).

Lipid-binding gel shift assay: 3XFLAG-tagged *S. cerevisiae* VPS13$_{1\text{-}1350}$ with WT or mutant sequences were purified using the same strategy described above for *C. thermophilum* Vps131-1390. For lipid binding, 7 ul of 150 nM purified protein was incubated with 1 mg of dried films of NBD-PA, NBD-PC, or no lipid on ice for two hours. 7 ul of 2x native gel sample loading buffer were then added and 14 μl of sample was loaded onto a 4% - 15% gradient native gel (Bio-rad, #4568086) and run at a constant voltage of 90V for 90 minutes.

Negative staining: 3XFLAG-tagged *S. cerevisiae* VPS13$_{1\text{-}1350}$ with WT or mutant sequences were purified using the same strategy described above for *C. thermophilum* Vps13$_{1\text{-}1390}$, while wild type VPS13 was purified from 50 ml of Expi293 cells and mutant constructs 1 and 2 were purified from 200 ml of Expi293 cells. Samples were negatively stained on copper grids overlaid with 10 nm amorphous carbon with 2% uranyl acetate. Grids were imaged using an FEI Tecnai T12 microscope operated at an accelerating voltage of 120 kV with a nominal magnification of 52,000x (2.14 Å/pixel at the specimen level). 2D classification was performed in RELION 3.0.4, where 100 manually picked particles were selected as references for Auto-pick in RELION 3.0.4. Final 2D classification was done using auto-picked particles.

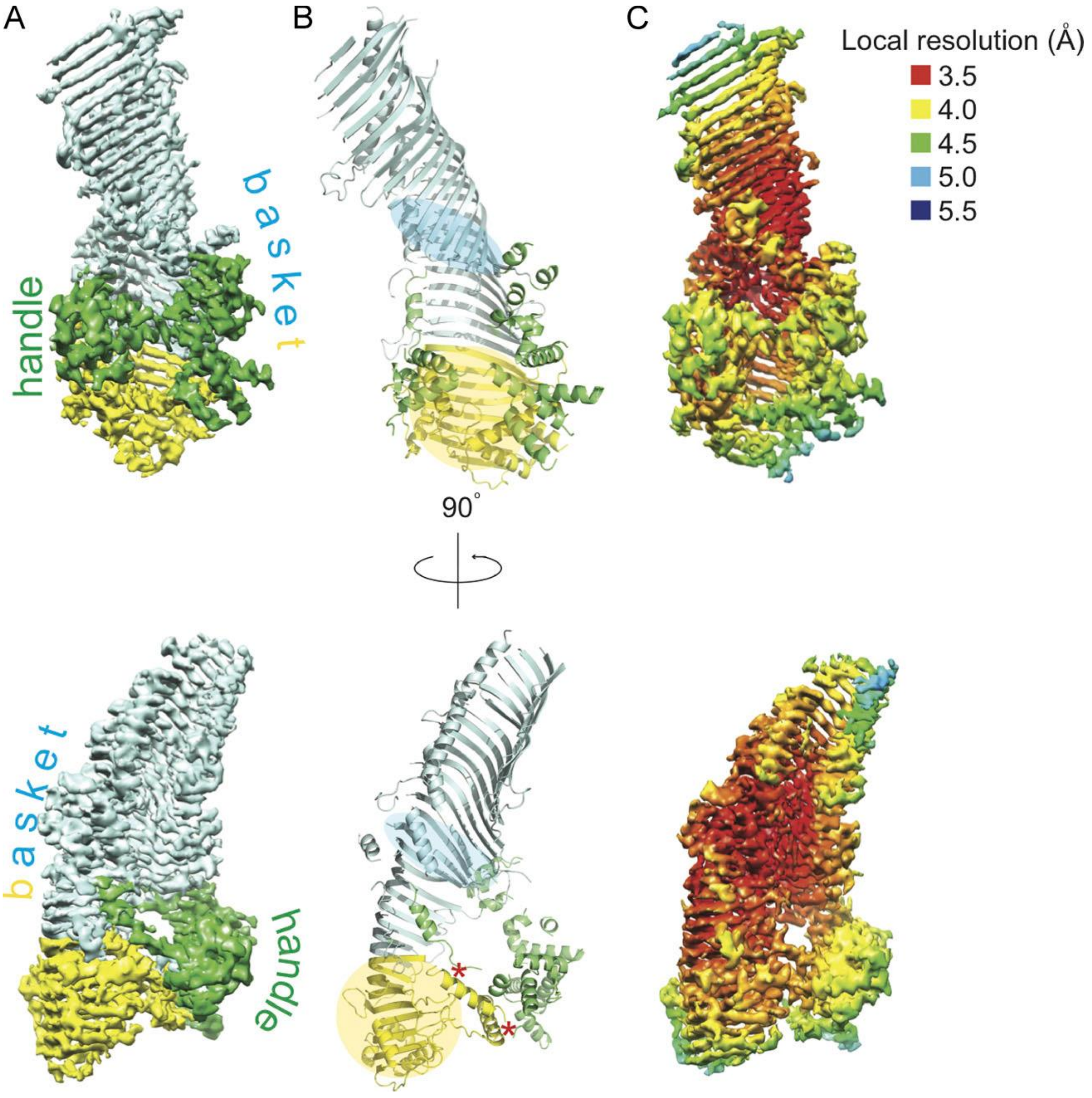

Figure 2.1. VPS13 forms a channel for lipid transport. (A) The density map for VPS131-1390 (contoured at 4.55 signal/noise), which resembles a twisted gathering basket. The “basket” is colored light blue and yellow, where yellow corresponds to the portion of *C. thermophilum* VPS13 previously crystallized (PDBID 6CBC, residues 1-335). Helices comprising the “handle” are green, except for two helices from 6CBC (yellow). (B)

Secondary structure is indicated. Red asterisks mark helices positionally adjusted with respect to 6CBC to form part of the “handle”. For functional assays, mutations were introduced to render bands within the VPS131-1390 channel hydrophilic and unable to bind lipids. The bands are indicated in yellow (mutant 1) and blue (mutant 2) shading and arrows. (C) Density map colored by local resolution. In a-c, VPS131-1390 in lower panels is rotated by 90° with respect to the top panels. At top, the view is into the basket interior at the VPS13 N-terminal end; in the bottom panels, the view is into the interior of the basket at its C-terminal end. (See also Movie S1).

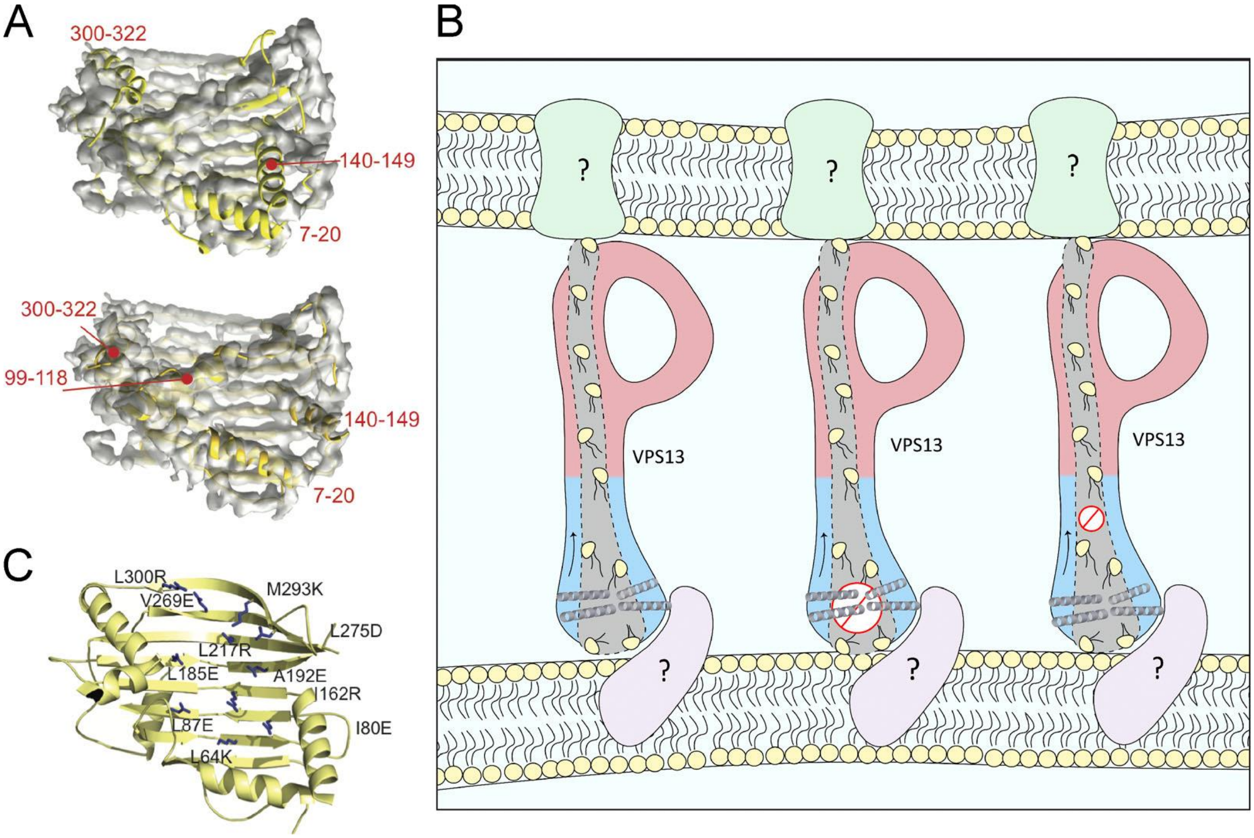

Figure 2.2. The VPS131-335 fragment is located at the wider end of the VPS131-1390 “basket”. (A) VPS131-335 coordinates (PDBID 6CBC) were docked into the part of the EM map colored yellow in Figure 1 A-B (top) and fitted (bottom). (B) VPS13 may function as a channel for lipid transfer between membranes. Intact VPS13 resembles a bubble wand(De et al., 2017); the portion corresponding to VPS131-1390 is blue. Mutations were introduced to render the N-terminal or middle portion of the channel hydrophilic, as indicated here and in Fig. 1B. VPS13 may cooperate with protein partners to ensure directional lipid transport. (C) Changes in mutant 1 are indicated here in a model of *S. cerevisiae* VPS13 based on the crystal structure of Vps131-335 (PDBID 6CBC):

(L64K/I80E/L87E/I162R/L185E/A192E/L217R/V269E/L275D/M293K/L300R).

Mutations in

mutant 2:

V690D/L692R/L694E/I715K/A717D/M720K/I722D/I761R/I768E/F790D/M796D/L798R/V802E/I816R/G820D/L827E.

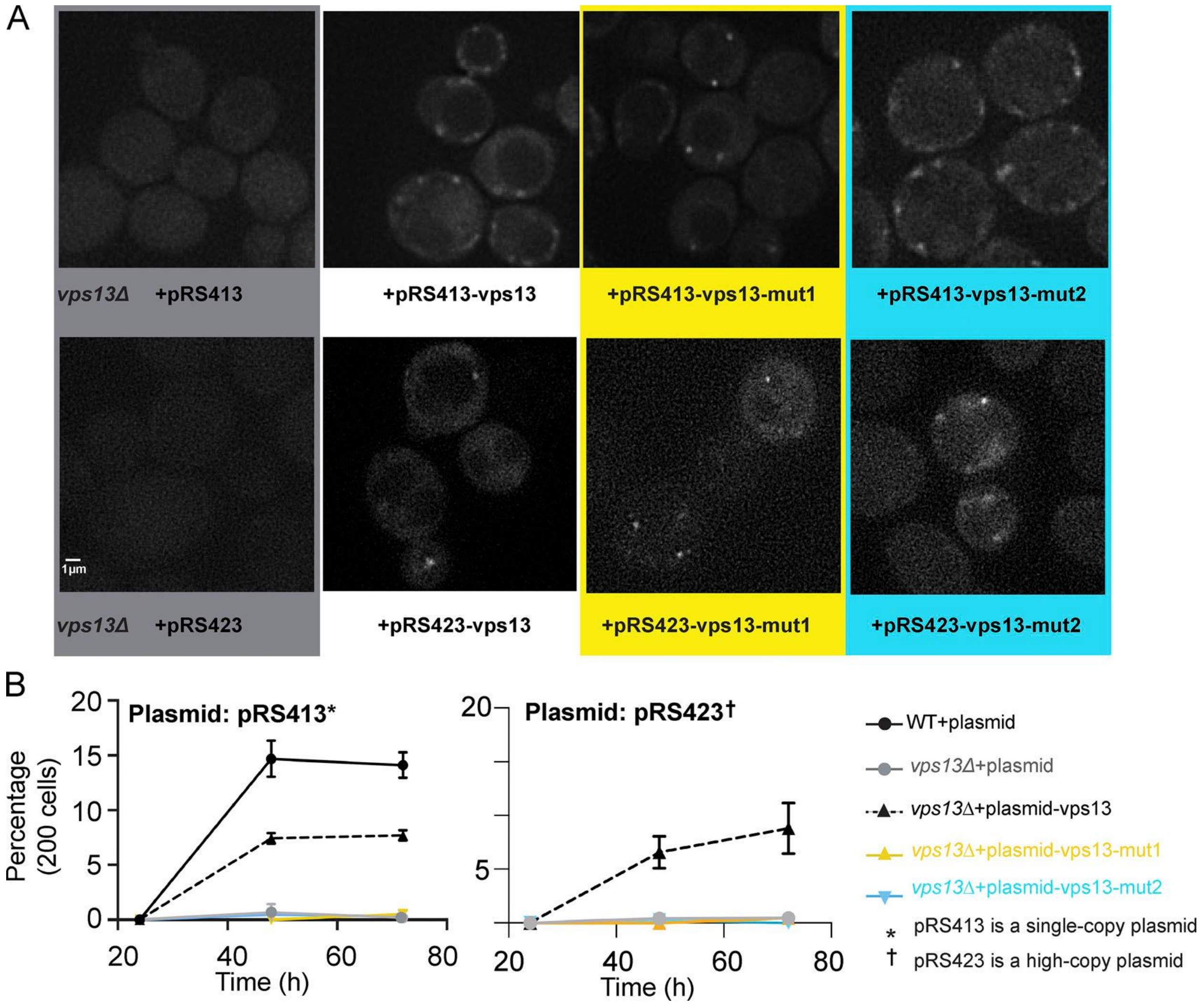

Figure 2.3. Mutations that render portions of the VPS131-1390 channel unable to bind lipids (Fig. 2B-C) abrogate VPS13 function in sporulation. (A) Low copy (*CEN*/pRS413) or multicopy (2μm/pRS423) plasmids encoding GFP-tagged VPS13 constructs were expressed in *vps13*Δ strains and visualized as fluorescent punctae by fluorescence microscopy. Also see Fig. S1. (B) Yeast lacking *VPS13* fail to sporulate(Enyenihi and Saunders, 2003). Sporulation can be rescued by *VPS13* but not the channel mutants. The experiment was repeated in triplicate. SD indicated.

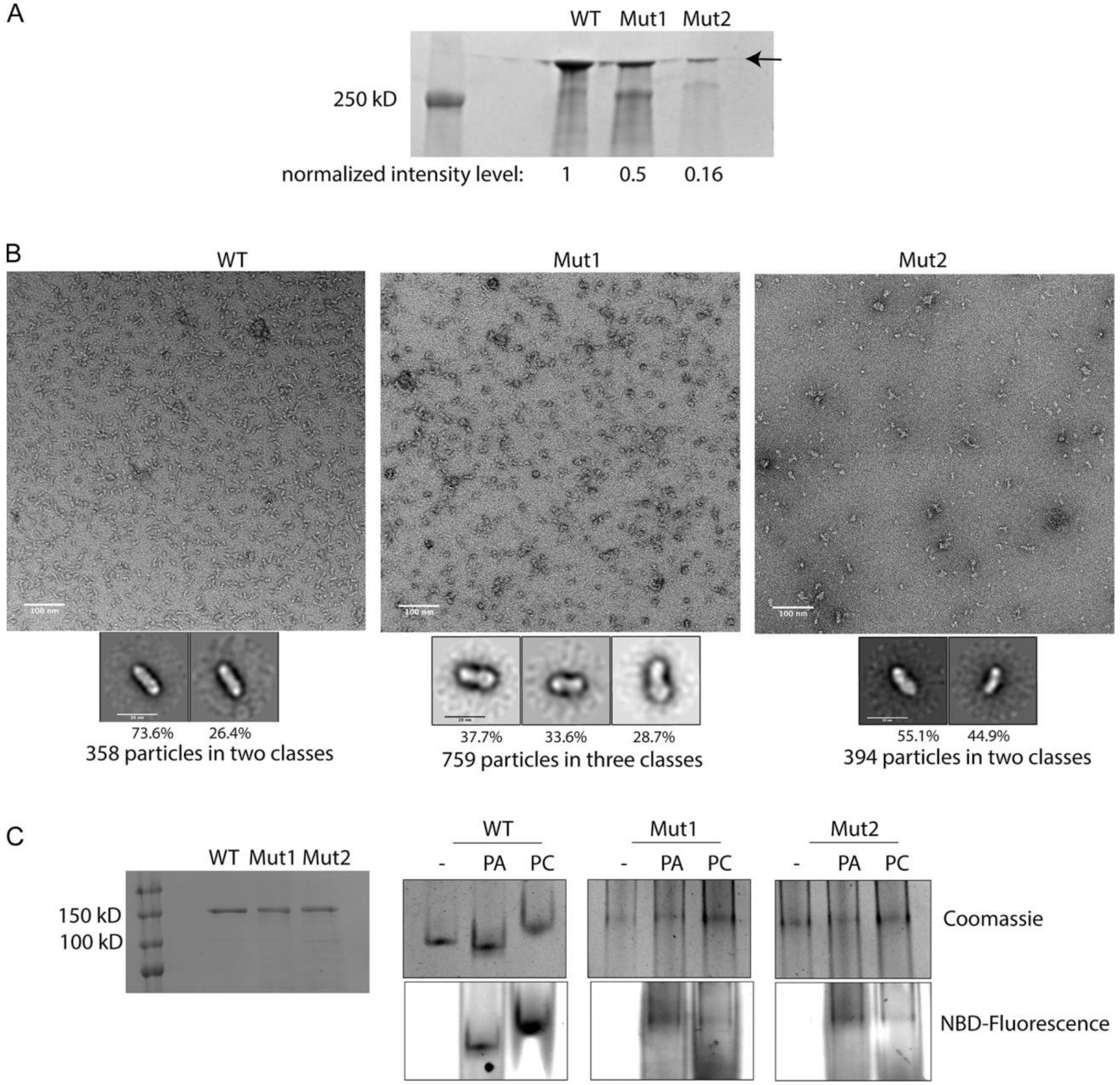

Supplementary Figure 2.1. Characterization of VPS13 mutant constructs. (A) Immunoprecipitation of GFP-tagged VPS13 protein from yeast cells expressing the protein from an integrated genomic copy under control of a *GAL1* promoter. From left to right: wild type, mutation 1, mutation 2. Proteins in each lane are purified from equal numbers of cells, and the indicated yield is normalized to wild type VPS13 protein. (B) Negative staining of 3xFLAG-tagged *Saccharomyces cerevisiae* VPS131-1350 purified from Expi293 cells, with representative 2D-class averages shown below. Numbers of particles included in averages are indicated. from left to right: wild type, mutation 1, mutation 2. (C) Lipid binding gel shift assay with *Saccharomyces cerevisiae* VPS131-1350. Equal amounts of VPS131-1350 constructs are co-incubated with the indicated fluorescent lipids (PA is phosphatidic acid; PC is phosphatidylcholine; NBD is nitrobenzoxadiazole) or no lipids and separated on a native gel. Gel imaging performed both by fluorescence imaging and Coomassie staining. From left to right: wild type, mutation 1, mutation 2.

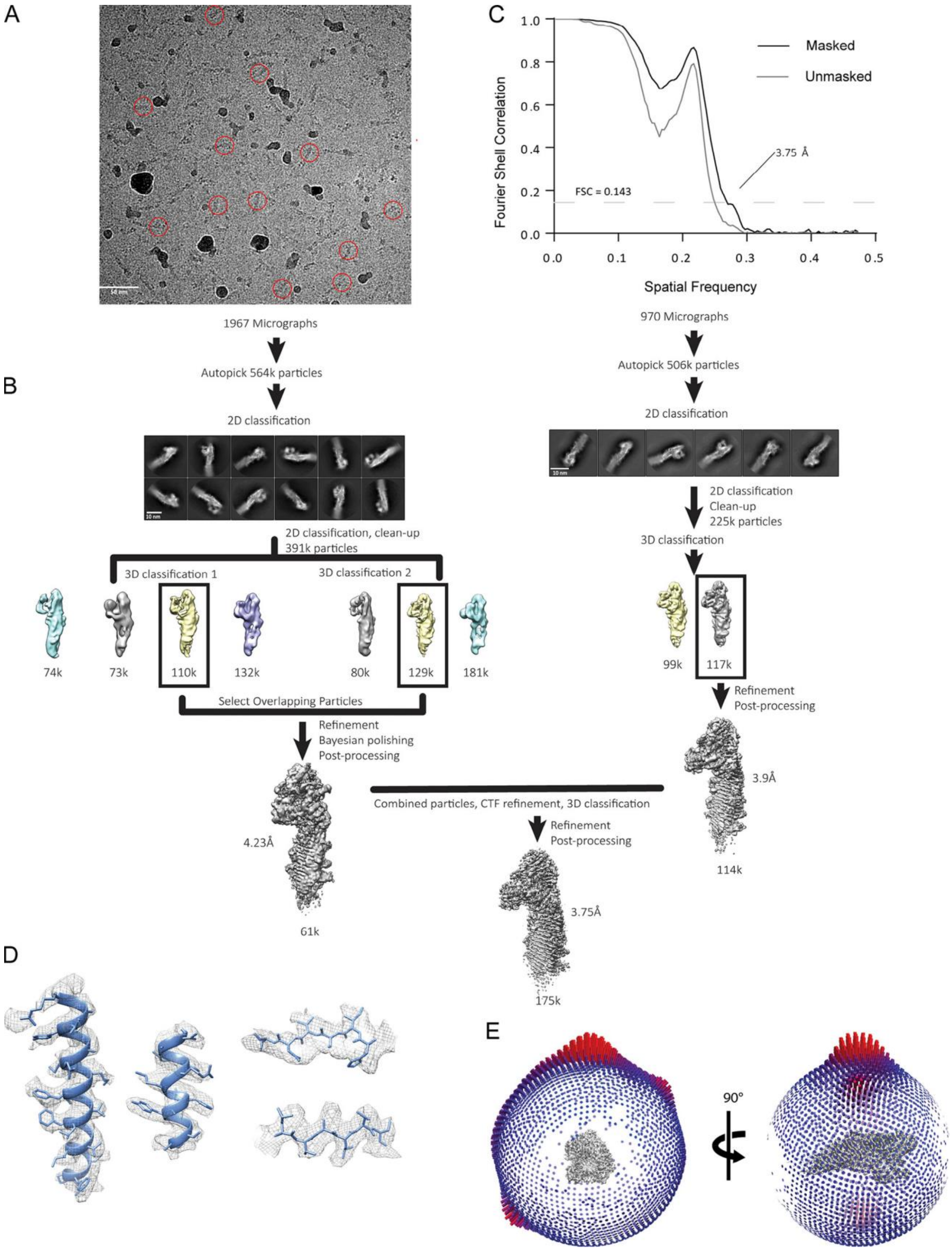
A
50 nm
1967 Micrographs
Autopick 564k particles
2D classification
10 nm
B
2D classification, clean-up
391k particles
3D classification 1
3D classification 2
74k
73k
110k
132k
80k
129k
181k
Select Overlapping Particles
Refinement
Bayesian polishing
Post-processing
4.23Å
61k
Combined particles, CTF refinement, 3D classification
Refinement
Post-processing
3.75Å
175k
C
Fourier Shell Correlation
Spatial Frequency
1.0
0.8
0.6
0.4
0.2
0.0
0.0
0.1
0.2
0.3
0.4
0.5
Masked
Unmasked
3.75 Å
FSC = 0.143
970 Micrographs
Autopick 506k particles
2D classification
10 nm
2D classification
Clean-up
225k particles
3D classification
99k
117k
Refinement
Post-processing
3.9Å
114k
D
E
90°

Supplementary Figure 2.2. CryoEM workflow. (A) A representative raw micrograph of Vps13 collected on a Titan Krios. Some of the particles are circled red. See Experimental Methods for details. (B) CryoEM workflow resulting in a density map at 3.75 Å resolution. The box side length of individual averages is 26.2 nm. See Experimental Methods for details. (C) FSC curves after gold standard refinement for masked and unmasked maps with FSC cut-off at 0.143 shown by a dashed line (D) CryoEM density for selected high-resolution regions, consistent with the reported resolution range. (E) Particle orientation distribution of the final map.

Table S2.1 primer info

Construct Name	**Species**	**Primer**
VPS13 (1-1390)	**C.Thermophilum**	cgaattcgagctcggcgcgccaatgttagaaggtctggtagcaggg atatcagatctatcgatgaattcttacgtgtgctgctccacgtc
"VPS13-mut1, VPS13-mut2, pRS413; VPS13-mut1, VPS13-mut2, pRS423-VPS13	**S. Cerevisiae**	gatatcgaattcctgcagcccggggaactgatcagtcctcgcaatattttc agactctaacatttaactgttcttaattttccttttttctg taagaacagttaaatgttagagtctttagctgctaatttg cttgctcaccatatcttcattctcgtcaaattcaatag cgagaatgaagatatggtgagcaagggcgag gtacaggacctttcttgtacagctcgtccatg gagctgtacaagaaaggtcctgtactgcaag tttcatatgtgatcataggatagcttcacagtac agctatcctatgatcacatatgaaagtatatacccgc atcgtaaacgccgccgaggcaactgtagaaggttggacaacacaaacaagaatgggtattgagtctttgttggaagac accagaagagtaattaacgtaatcgccgttgttttcttcatcatcaatcatagaaggtatagaattagcaatcaaattca aaagctggagctccaccgcggtggctcaatctgggggtatgcg aaagctggagctccaccgcggtggcatagcacgttcaacatccc
VPS13-mut1,	**S. Cerevisiae**	actagtggatcccccgggctgcaggaattcatgttagagtctttagctg agcgtgacataactaattacatgactcgagtcataggatagcttcacag

VPS13-mut2, pRS406-GAL		gcttatcgataccgtcgacctcgagatgttagagtctttagctg gacataactaattacatgactcgagtcataggatagcttcacag cgaagagtaaaaaattgtacttggcg aagacagaaaatttgctgacattg

Table S2.2. Cryo-EM data collection and image processing statistics

	VPS13$_{1390}$ (EMD – 21113)
Magnification	13000x
Voltage (kV)	300
Electron exposure (e$^-$/Å)	50.4 (Dataset 1) 49.6(Dataset 2)
Defocus range (μm)	-1.9 to 2.9 μm (Dataset 1) -1.4 to -2.3 μm (Dataset 2)
Pixel size (Å)	1.05 Å
Symmetry imposed	C1
Initial particle images (No.)	564503 (Dataset 1)

	506742 (Dataset 2)
Final particle images (No.)	175362
Map resolution (Å)	3.75
FSC threshold	0.143
Map resolution range (Å)	21 – 3.5
Map sharpening *B* factor (Å)	-105.771

Reference:

Bean, B.D.M., S.K. Dziurdzik, K.L. Kolehmainen, C.M.S. Fowler, W.K. Kwong, L.I. Grad, M. Davey, C. Schluter, and E. Conibear. 2018. Competitive organelle-specific adaptors recruit Vps13 to membrane contact sites. J Cell Biol. 217:3593-3607.

Chowdhury, S., C. Otomo, A. Leitner, K. Ohashi, R. Aebersold, G.C. Lander, and T. Otomo. 2018. Insights into autophagosome biogenesis from structural and biochemical analyses of the ATG2A-WIPI4 complex. Proceedings of the National Academy of Sciences of the United States of America. 115:E9792-E9801.

De, M., A.N. Oleskie, M. Ayyash, S. Dutta, L. Mancour, M.E. Abazeed, E.J. Brace, G. Skiniotis, and R.S. Fuller. 2017. The Vps13p-Cdc31p complex is directly required for TGN late endosome transport and TGN homotypic fusion. J Cell Biol. 216:425-439.

Emsley, P., B. Lohkamp, W.G. Scott, and K. Cowtan. 2010. Features and development of Coot. Acta crystallographica. Section D, Biological crystallography. 66:486-501.

Enyenihi, A.H., and W.S. Saunders. 2003. Large-scale functional genomic analysis of sporulation and meiosis in Saccharomyces cerevisiae. Genetics. 163:47-54.

Gomez-Sanchez, R., J. Rose, R. Guimaraes, M. Mari, D. Papinski, E. Rieter, W.J. Geerts, R. Hardenberg, C. Kraft, C. Ungermann, and F. Reggiori. 2018. Atg9 establishes Atg2-dependent contact sites between the endoplasmic reticulum and phagophores. J Cell Biol. 217:2743-2763.

Kotani, T., H. Kirisako, M. Koizumi, Y. Ohsumi, and H. Nakatogawa. 2018. The Atg2-Atg18 complex tethers pre-autophagosomal membranes to the endoplasmic reticulum for autophagosome formation. Proceedings of the National Academy of Sciences of the United States of America. 115:10363-10368.

Kumar, N., M. Leonzino, W. Hancock-Cerutti, F.A. Horenkamp, P. Li, J.A. Lees, H. Wheeler, K.M. Reinisch, and P. De Camilli. 2018. VPS13A and VPS13C are lipid transport proteins differentially localized at ER contact sites. J Cell Biol. 217:3625-3639.

Lang, A.B., A.T. John Peter, P. Walter, and B. Kornmann. 2015. ER-mitochondrial junctions can be bypassed by dominant mutations in the endosomal protein Vps13. J Cell Biol. 210:883-890.

Lesage, S., V. Drouet, E. Majounie, V. Deramecourt, M. Jacoupy, A. Nicolas, F. Cormier-Dequaire, S.M. Hassoun, C. Pujol, S. Ciura, Z. Erpapazoglou, T. Usenko, C.A. Maurage, M. Sahbatou, S. Liebau, J. Ding, B. Bilgic, M. Emre, N. Erginel-Unaltuna, G. Guven, F. Tison, C. Tranchant, M. Vidailhet, J.C. Corvol, P. Krack, A.L. Leutenegger, M.A. Nalls, D.G. Hernandez, P. Heutink, J.R. Gibbs, J. Hardy, N.W. Wood, T. Gasser, A. Durr, J.F. Deleuze, M. Tazir, A. Destee, E. Lohmann, E. Kabashi, A. Singleton, O. Corti, A. Brice, S. French Parkinson's Disease Genetics, and C. International Parkinson's Disease Genomics. 2016. Loss of VPS13C Function in Autosomal-Recessive Parkinsonism Causes Mitochondrial Dysfunction and Increases PINK1/Parkin-Dependent Mitophagy. American journal of human genetics. 98:500-513.

Osawa, T., T. Kotani, T. Kawaoka, E. Hirata, K. Suzuki, H. Nakatogawa, Y. Ohsumi, and N.N. Noda. 2019. Atg2 mediates direct lipid transfer between membranes for autophagosome formation. Nature structural & molecular biology. 26:281-288.

Owens, T.W., R.J. Taylor, K.S. Pahil, B.R. Bertani, N. Ruiz, A.C. Kruse, and D. Kahne. 2019. Structural basis of unidirectional export of lipopolysaccharide to the cell surface. Nature. 567:550-553.

Park, J.S., and A.M. Neiman. 2012. VPS13 regulates membrane morphogenesis during sporulation in Saccharomyces cerevisiae. J Cell Sci. 125:3004-3011.

Pettersen, E.F., T.D. Goddard, C.C. Huang, G.S. Couch, D.M. Greenblatt, E.C. Meng, and T.E. Ferrin. 2004. UCSF Chimera--a visualization system for exploratory research and analysis. Journal of computational chemistry. 25:1605-1612.

Rampoldi, L., C. Dobson-Stone, J.P. Rubio, A. Danek, R.M. Chalmers, N.W. Wood, C. Verellen, X. Ferrer, A. Malandrini, G.M. Fabrizi, R. Brown, J. Vance, M. Pericak-Vance, G. Rudolf, S. Carre, E. Alonso, M. Manfredi, A.H. Nemeth, and A.P. Monaco. 2001. A conserved sorting-associated protein is mutant in chorea-acanthocytosis. Nature genetics. 28:119-120.

Rohou, A., and N. Grigorieff. 2015. CTFFIND4: Fast and accurate defocus estimation from electron micrographs. Journal of structural biology. 192:216-221.

Ueno, S., Y. Maruki, M. Nakamura, Y. Tomemori, K. Kamae, H. Tanabe, Y. Yamashita, S. Matsuda, S. Kaneko, and A. Sano. 2001. The gene encoding a newly discovered protein, chorein, is mutated in chorea-acanthocytosis. Nature genetics. 28:121-122.

Valverde, D.P., S. Yu, V. Boggavarapu, N. Kumar, J.A. Lees, T. Walz, K.M. Reinisch, and T.J. Melia. 2019. ATG2 transports lipids to promote autophagosome biogenesis. J Cell Biol. 218:1787-1798.

Wan, R., R. Bai, C. Yan, J. Lei, and Y. Shi. 2019. Structures of the Catalytically Activated Yeast Spliceosome Reveal the Mechanism of Branching. Cell. 177:339-351 e313.

Wong, L.H., A.T. Gatta, and T.P. Levine. 2019. Lipid transfer proteins: the lipid commute via shuttles, bridges and tubes. Nat Rev Mol Cell Biol. 20:85-101.

Yang, G., R. Zhou, Q. Zhou, X. Guo, C. Yan, M. Ke, J. Lei, and Y. Shi. 2019. Structural basis of Notch recognition by human gamma-secretase. Nature. 565:192-197.

Zheng, S.Q., E. Palovcak, J.P. Armache, K.A. Verba, Y. Cheng, and D.A. Agard. 2017. MotionCor2: anisotropic correction of beam-induced motion for improved cryo-electron microscopy. Nature methods. 14:331-332.

Zivanov, J., T. Nakane, B.O. Forsberg, D. Kimanius, W.J. Hagen, E. Lindahl, and S.H. Scheres. 2018. New tools for automated high-resolution cryo-EM structure determination in RELION-3. eLife. 7.

Chapter 3 Insights into lysosomal PI(3,5)P$_2$ homeostasis from a structural and biochemical analysis of the PIKfyve lipid kinase complex.

This work was previously published as “Lees, J. A.[*], Li, P.[*], Kumar, N., Weisman, L. S., & Reinisch, K. M[**]. (2020). Insights into lysosomal PI (3, 5) P2 homeostasis from a structural-biochemical analysis of the PIKfyve lipid kinase complex. *Molecular Cell*, *80*(4), 736-743. *Contributed equally** Corresponding author, karin.reinisch@yale.edu”

Author contributions： KMR and LSW conceived the project; KMR, NK, JAL, and PL designed experiments. NK developed overexpression protocols for the complex and obtained initial data supporting that Fig4 is a protein phosphatase from phosphosite analysis of PIKfyve in PIKfyve complexes assembled in cells. LSW originated the idea that Fig4 could be a protein phosphatase. JAL is responsible for the cryo-EM reconstruction of the PIKfyve complex, lipid phosphatase assays, lipid kinase assays with respect to membrane incorporated PI3P, and the PIKfyve phosphosite analysis using complexes assembled in vitro from PIKfyve and Fig4/Vac14. PL is responsible for negative stain analysis of the PIKfyve complex and lipid kinase assays with respect to soluble phosphoinositides. PL made all figures. KMR supervised the project and wrote the manuscript with input from all authors.

Insights into lysosomal PI(3,5)P_2 homeostasis from a structural biochemical analysis of the PIKfyve lipid kinase complex.

Joshua A. Lees*[1], PeiQi Li*[1], Nikit Kumar[1], Lois S. Weisman[2], Karin M. Reinisch**[1]

[1]Department of Cell Biology, Yale School of Medicine, 333 Cedar Street, New Haven, CT 06520, USA
[2]Life Sciences Institute, University of Michigan, Ann Arbor, MI 48109, USA.
*Contributed equally
** Corresponding author, karin.reinisch@yale.edu

Summary

The phosphoinositide PI(3,5)P_2, generated exclusively by the PIKfyve lipid kinase complex, is key for lysosomal biology. Here we explore how PI(3,5)P_2 levels within cells are regulated. We find the PIKfyve complex comprises 5 copies of the scaffolding protein Vac14, and one copy each of the lipid kinase PIKfyve, generating PI(3,5)P_2 from PI3P, and the lipid phosphatase Fig4, reversing the reaction. Fig4 is active as a lipid phosphatase only in the ternary complex, whereas PIKfyve within the complex cannot access membrane-incorporated phosphoinositides due to steric constraints. We find further that the phosphoinositide-directed activities of both PIKfyve and Fig4 are regulated by protein directed activities within the complex. PIKfyve autophosphorylation represses its lipid kinase activity and stimulates Fig4 lipid phosphatase activity. Further, Fig4 is also a protein phosphatase acting on PIKfyve to stimulate its lipid kinase activity, explaining why catalytically active Fig4 is required for maximal PI(3,5)P_2 production by PIKfyve in vivo.

Eukaryotic cells have seven species of phosphoinositide lipids differentially enriched at different compartments. Although these lipids are present only in minute quantities, they play major roles in organelle dynamics and signaling. Two phosphoinositides critical for lysosome biology are PI3P and its derivative PI(3,5)P_2, which is generated by the still poorly characterized PIKfyve complex (Hasegawa et al., 2017; Jin et al., 2016). PIKfyve is conserved in all eukaryotes and is their only source of PI(3,5)P_2. Highlighting the importance of this complex in cell physiology, mutations in its subunits result in disabling neurodegenerative diseases such as forms of Charcot-Marie Tooth (CMT) disease (Chow et al., 2007) and Amyotropic Lateral Sclerosis (ALS) (Chow et al., 2009). PIKfyve inhibition has been proposed as an anti-viral treatment (Hulseberg et al., 2019; Nelson et al., 2017), and a selective inhibitor of PIKfyve activity, apilimod, is being evaluated as a treatment for non-Hodgkins lymphoma (Gayle et al., 2017).

In addition to the lipid kinase PIKfyve itself (also called Fab1), the complex includes a lipid phosphatase in the Sac family, Fig4 (also called Sac3), and a scaffolding protein Vac14 (also called ArPIKfyve) (Fig. 1A). While PIKfyve transfers a phosphate group from ATP to convert PI3P to PI(3,5)P_2, Fig4 dephosphorylates PI(3,5)P_2 in the reverse reaction.

How these activities are coordinated within the complex to avoid futile cycles of ATP hydrolysis has been enigmatic. Further adding to the mystery is the observation that PI(3,5)P_2 levels in cells deficient in Fig4 activity, as for example in patients with CMT, are reduced rather than upregulated as might have been expected (Chow et al., 2007; Duex et al., 2006; Shisheva et al., 2019; Strunk et al., 2020).

Here we combine negative stain- and cryo-EM studies elucidating the architecture of the human PIKfyve complex at medium to low resolution with a biochemical analysis to obtain first insights as to how the antagonistic activities within the complex are regulated. Our structural studies show that Vac14 pentamerizes into a star-shaped structure, which can bind a single copy each of PIKfyve and Fig4. We have found that Fig4 is active as a lipid phosphatase only in the intact complex including PIKfyve, whereas the ability of PIKfyve to generate PI(3,5)P_2 in membranes is suppressed in the complex as compared to by itself.

Our structural data indicate that complex formation conformationally restrains the kinase domain to prevent its access to membranes containing the PI3P substrate. We further report that in addition to its activity on lipid, Fig4 is a serine phosphatase that acts on PIKfyve to increase its lipid kinase activity. While PIKfyve within the complex cannot access PI3P, it may nevertheless be primed by Fig4 for maximal activity following a conformational change, such as complex dissociation, in response to a still unknown stimulus. This model would explain why the ablation of Fig4 activity depresses PI(3,5)P_2 production in cells.

Vac14 forms a pentameric scaffold through which PIKfyve and Fig4 interact.

As a first step in understanding the regulation of the PIKfyve complex, we examined its architecture and that of its subcomplexes by negative stain electron microscopy. The protein assemblies were produced in mammalian cells (Expi293F) by transfecting these with DNAs coding for one or combinations of PIKfyve components. Fig4 was N-terminally 3xFLAG-tagged to capture Fig4/Vac14 complex, PIKfyve was N-terminally 3xFLAG-tagged to capture PIKfyve alone or ternary complex, and Vac14 alone was purified via an N-terminal 2xStrepII tag. Vac14, predicted to comprise almost entirely alpha helical HEAT repeats, forms a rod that oligomerizes into a pentameric star-like structure (Fig 3.1B). As C-terminal deletions abrogate Vac14 oligomerization (Ikonomov et al., 2009), Vac14 self-association at the center of the star-shaped assembly must be via its C-terminal portions. The N-terminus of Vac14 is at the other end of each Vac14 “leg”, as identified by density corresponding to maltose binding protein (MBP) in 2D class averages of an MBP-Vac14 construct (Fig 3.1B). (We could not find density corresponding to MBP in 2D class averages of a Vac14-MBP construct (distinct from the MBP-Vac14 construct).) We next produced Fig4/Vac14, unexpectedly finding that only one copy of Fig4 associates with each Vac14 pentamer. The density corresponding to Fig4 appears between the N-terminal tips of two of the Vac14 “legs” (Fig 3.1C). PIKfyve alone is elongated and kinked at one end (Fig 3.1D, top row). In the ternary complex, there is density for a single copy of PIKfyve appended to one of the Vac14 legs that flanks Fig4, extending away from the Vac14 pentamer (Fig 3.1E). We observed only a single stoichiometry, a pentamer of Vac14 associated with one copy each of the phosphatase and kinase, irrespective of the ratios of Fig4:Vac14 or PIKfyve: Fig4:Vac14 DNAs used in transfection. Addition of independently expressed and purified Fig4 and PIKfyve constructs did not change this stoichiometry. The five-fold symmetry of the Vac14 pentamer is disrupted in both the binary and ternary complexes, apparent as a different spacing between Vac14 legs interacting with Fig4 and PIKfyve (Fig. 3.1F).

The Fig4 and PIKfyve active sites cannot access membranes simultaneously in the complex.

A ternary complex comprising PIKfyve$_{S2053E}$, which harbors a point-mutation in the kinase activation loop (see characterization below), along with wildtype versions of Fig4 and Vac14 was analyzed further by cryo-EM, yielding a map at a final nominal resolution of 5.25 Å (FSC=0.143 criterion). Due to the extended shape and high flexibility of the complex, it was not possible to obtain a single map with well-ordered density for all three proteins. Rather, a reconstruction of the complete complex was synthesized from three independent maps obtained from the same micrograph dataset, centered on different portions of the complex, which were calculated separately (as described in Methods; Fig. S3.1, S3.2) and superimposed based on their overlaps, to form a composite reconstruction (Fig. 3.2). In the reconstruction, the Vac14 pentamer is cup-shaped, measuring 240 Å across and 110 Å deep, with both Fig4 and PIKfyve occupying sites near the "rim" of the cup as defined by the Vac14 N termini. Each Vac14 "leg" was modeled as a series of alpha helices, although their connectivity could not be established at the resolution of the reconstruction. The Sac homology module of Fig4 comprises an N-terminal regulatory and the upstream catalytic domain and was modeled based on a crystal structure of the same module in Sac1 (PDB 4tu3). It could be confidently docked into density between opposite surfaces of two neighboring copies of Vac14 (Fig. 3.2), corresponding to the highest resolution region in our maps. The Fig4 active site is oriented to face the top of the Vac14 cup. The catalytic domain of the Fig4 Sac-homology module primarily mediates the interactions with both neighboring Vac14's. This interaction slightly twists one of the Vac14 copies, likely modifying a surface on its opposite face to facilitate PIKfyve binding, consistent with PIKfyve's reported inability to bind Fig4 or Vac14 alone (Ikonomov et al., 2009). We did not observe density that could be attributed to portions of Fig4 downstream of its catalytic domain, although Fig4 C-terminal regions interact with Vac14 (Ikonomov et al., 2009).

PIKfyve comprises four structured regions, including a FYVE domain and CCR, CCT and kinase modules, separated by long unstructured sequences (Fig 3.1A). We generated homology models for the kinase and CCT modules of PIKfyve using threading software (RaptorX and I-Tasser (Kallberg et al., 2012; Yang et al., 2015), PDB 1e8x and 3pn9). The CCT module was manually fitted into PIKfyve density closest to Vac14 (Fig. 3.2B). The CCT module consists of three domains, termed axial, intermediate and equatorial in the chaperonin TCP1/TRiC where this module is also present, with the so-called equatorial domain abutting Vac14. For the best fit into the map, the axial/intermediate domains of PIKfyve were reoriented with respect to the equatorial domain as compared to in other contexts (PDBIDs 1a6d, 5gw5, 3pn9). Consistent with our assignment, the PIKfyve CCT-domain is required for the formation of the ternary complex (Botelho et al., 2008; Ikonomov et al., 2009). The kinase domain was docked into the map adjacent to the CCT-domain, with the kinase active site twisted by ~45° away from the top of the Vac14 “cup” (Fig. 3.2B, C). As the resolution in this part of the map was low (local resolutions are ~8-10 Å, Fig. S3.2D), locations of both the CCT and kinase domains were independently confirmed by negative stain EM of MBP-labeled PIKfyve alone (Fig. 3.1D). In the cryo-EM maps, there is additional unassigned density in PIKfyve between the CCT and kinase domains as well as adjacent to the kinase domain N-terminus. An MBP-label inserted N-terminally to the CCR domain in PIKfyve is positioned between the CCT and kinase domains in negative stain micrographs (Fig 3.1D), suggesting that the density between the CCT and kinase modules in the cryo-EM maps corresponds to an N-terminal portion of the CCR domain. The remaining unassigned density could correspond to C-terminal portions of the CCR region and/or portions or the FYVE domain. The fold of the CCR module is unknown.

The PIKfyve complex is recruited to endo-lysosomal membranes via interactions between PI3P and the FYVE domain of PIKfyve (Hasegawa et al., 2017; Jin et al., 2016). Given the location of PIKfyve close to one of the Vac14 legs, it is plausible that the complex associates with membranes via the "rim" of the Vac14 cup (Fig 3.2C). If the complex is bound in this fashion, the Fig4 active site is oriented for optimal access to its lipid substrate while the PIKfyve active site is rotated away from the membrane (Fig 3.2C) and so is sub-optimally positioned for contact with substrate. The different orientations of their active site pockets in the complex indicates that either Fig4 or PIKfyve, but not both, can access membrane bound phosphoinositides at one time. This suggests a structural switching mechanism that controls the relative access of Fig4 and PIKfyve to substrate, and thus, their activities.

PI3P/PI35P2 metabolism by individual PIKfyve components is modulated within the intact complex.

To better understand how lipid phosphorylation and dephosphorylation activities are coordinated within the complex; we next compared these activities in subcomplexes, containing either PIKfyve or Fig4/Vac14, and intact complex. To make the intact complex for these experiments, we co-expressed Fig4 and Vac14, purified them together, and then mixed the Fig4/Vac14 subcomplex with PIKfyve that had been expressed and purified separately. We were unable to make Fig4 alone as it is proteolytically degraded in the absence of Vac14, likely because its C-terminal portions are unstructured.

We monitored PIKfyve lipid kinase activity on soluble diC6-PI3P (C6-C6-BODIPY-FLPI3P)

as well as PI3P incorporated in liposomes, with different outcomes. We followed diC6-PI3P conversion to diC6-PI(3,5)P_2 by thin layer chromatography, finding that PIKfyve alone and PIKfyve/Fig4/Vac14 phosphorylated diC6-PI3P with similar efficiencies (Fig. 3A). Although Fig4 in the intact complex dephosphorylates soluble PI(3,5)P_2 (see below), neither the presence of Fig4 or a catalytically inactivated version (C486S) significantly affected PI(3,5)P_2 generation. This could be because the PI3P phosphorylation reaction is more efficient. In contrast, when we used a radiometric assay to monitor PI(3,5)P_2 production from liposome incorporated PI3P and ^{32}P-ATP, we found that only PIKfyve alone but not PIKfyve/Fig4/Vac14 was active (Fig. 3.3B). This supports the notion that the kinase domain cannot access PI3P in the membrane because of a conformational restraint imposed within the complex, as suggested by the structure.

We next compared the lipid phosphatase activities of Fig4/Vac14 and PIKfyve/Fig4/Vac14 on diC8-PI(3,5)P2 using the malachite green assay, which measures the levels of orthophosphate released upon dephosphorylation. Robust Fig4 lipid phosphatase activity was observed only in the intact complex, including PIKfyve (Fig. 3.3C). The conformational changes in Fig4/Vac14 induced when PIKfyve is added may relieve an inhibition, perhaps by unblocking or rearranging the Fig4 active site. They may also correctly orient the Fig4 active site with respect to the membrane, but such a reorientation would not be necessary for activity with respect to the soluble diC8-lipids as used in the assay.

The protein kinase and phosphatase activities of PIKfyve and Fig4 regulate phosphoinositide metabolism.

PIKfyve has been well established as a ser kinase that auto phosphorylates itself to inhibit its lipid kinase activity (Sbrissa et al., 2000). We found, unexpectedly, that PIKfyve autophosphorylation is also required for the lipid phosphatase activity of Fig4 within the complex, for only wild-type PIKfyve but not a catalytically inactive version (K1877E) stimulates lipid hydrolysis by Fig4 in the malachite green assays (Fig. 3.3C). Because PIKfyve and Fig4/Vac14 were prepared separately and then mixed in the absence of ATP, it is improbable that Fig4 stimulation is due to its phosphorylation by PIKfyve. Instead, it is PIKfyve autophosphorylation that must stimulate Fig4 activity.

To determine which sites in PIKfyve are auto phosphorylated and to obtain insights as to how PIKfyve autophosphorylation might affect the activities of the complex with respect to phosphoinositides, we prepared two versions of PIKfyve/Fig4/Vac14, one containing wild-type and another the catalytically inactive PIKfyve (K1877E). We analyzed the PIKfyve phosphosites by mass spectrometry (MS/MS), finding serines that were phosphorylated only in the wild-type construct (S23, S48, S1522, S1669, S1969, and S2053) (Fig. 3.4). One of these sites (S2053) was of particular interest as it is located in the activation loop (residues 2036-2069) near the kinase active site, where it might play a role in inhibiting kinase activity. Consistent with such a role, we found a ~2-fold reduction in lipid kinase activity when we mutated this serine to glutamate, mimicking phosphorylation, versus no reduction when the serine was changed to alanine (Fig. 3.3D).

This reduction in activity is similar to that reported before for an auto phosphorylated versus a dephosphorylated form of the kinase (Sbrissa et al., 2000). It is likely that PIKfyve autophosphorylation at one or more of the six phosphosites we identified also affects Fig4 lipid phosphatase activity.

The observations (1) that PIKfyve is both a lipid and a protein kinase whose autophosphorylation affects both lipid kinase and phosphatase activities of the PIKfyve complex (Sbrissa et al., 2000)(and above) and (2) that a catalytically active version of Fig4 is required for normal PIKfyve function in vivo (Chow et al., 2007; Duex et al., 2006; Shisheva et al., 2019; Strunk et al., 2020) prompted us to explore the possibility that Fig4 might affect PIKfyve activity as a protein phosphatase. To determine whether Fig4 might act on PIKfyve, we prepared two versions of the PIKfyve/Fig4/Vac14 complex, as described before, one containing wild-type and the other a catalytically inactive Fig4 mutant (C486S). We again analyzed PIKfyve phosphosites in these complexes by mass spectrometry, finding that three of the sites phosphorylated by PIKfyve are dephosphorylated by Fig4 (S48, S1669, S2053). These sites include Ser2053 in the

PIKfyve activation loop, whose phosphorylation state affects lipid kinase activity (Fig 3.3D).

As another approach, we also overexpressed the two versions of the complex in mammalian cells (Expi293F) and similarly analyzed PIKfyve phosphosites, with similar results (S48 and S2053 are differentially phosphorylated). These results strongly support the idea that in addition to acting as PI(3,5)P_2 phosphatase, Fig4 is a serine phosphatase that regulates PIKfyve lipid kinase activity, explaining why an active form of Fig4 is required for normal levels of PI(3,5)P_2 in vivo. PTEN, the phosphatase that dephosphorylates PI(3,4,5)P_3 during PI3K/Akt signaling, also is active on protein substrates (Myers et al., 1997), setting a precedent for phosphatases with dual specificity on lipids and proteins.

Although relatively long, the PIKfyve activation loop cannot reach the Fig4 active site if PIKfyve and Fig4 are placed as in the cryo-EM structure. It is plausible, though, that the kinase and phosphatase active sites can move closer together as the complex flexes, or that there are conformational changes that allow for closer proximity, or that PIKfyve and Fig4 from different complexes interact in trans, or that Fig4 can act on PIKfyve either as the complex assembles or disassembles. Conformational changes within the complex will be subject to further investigation.

Concluding thoughts

The unusual 1:1:5 stoichiometry in the PIKfyve/Fig4/Vac14 complex is intriguing. From our structural studies, a key role of Vac14 pentamerization is as a scaffold that coordinates Fig4 and PIKfyve activities to avoid futile cycles of ATP hydrolysis. The Vac14 scaffold helps to optimally orient Fig4 in the complex with respect to the membrane for its lipid-targeted catalytic activities whereas PIKfyve is constrained and unable to access membrane incorporated PI3P.

Still, there may be additional roles for Vac14 pentamerization. For example, the Vac14 pentamer could help define membrane micro zones that are enriched in either PI3P or PI(3,5)P_2, and these roles remain to be investigated. Our studies have also uncovered an exquisite interplay between the lipid-directed activities of PIKfyve and Fig4 and their protein-directed activities that affect

phosphoinositide metabolism. We have found that PIKfyve autophosphorylation downregulates its lipid kinase activities (as also reported in (Sbrissa et al., 2000)) while simultaneously upregulating Fig4 activity with respect to phosphoinositide lipids. We have also discovered a new role for Fig4 as a protein phosphatase required for PIKfyve activation. Likely, PIKfyve and Fig4 will additionally be regulated by protein kinases and phosphatases extrinsic to the complex, and this remains to be explored.

These studies represent a major advance in understanding the regulation within the PIKfyve complex and lysosomal phosphoinositide homeostasis. Additionally, Vac14 has been reported to interact with a host of proteins, including Rabs, RabGEFs, RabGAPs, BAR domain proteins, scaffolding proteins, and others (Currinn et al., 2016; Ikonomov et al., 2015; Jin et al., 2016; Malia et al., 2018; Mayer et al., 2018; Schulze et al., 2014), which could modulate and be modulated by its interaction with the membrane and with PIKfyve and Fig4. These interactions likely play a role in spatiotemporal regulation of PIKfyve and Fig4 enzymatic activities, as well as signaling between the PIKfyve complex and downstream effectors. The specifics of these interactions and their relation to PIKfyve and Fig4 activities offer another clear avenue for follow-up work.

Materials and methods

Plasmid construction. Constructs of wildtype Vac14, Fig4, and PIKfyve were PCR amplified from plasmids gifted by the laboratory of L.Weisman and cloned into indicated linearized plasmids using Gibson Assembly (NEB). Plasmids were linearized via BamH1 and Not1 restriction enzymes (NEB). StrepII-tagged Vac14 and His-tagged Fig4 were cloned into pcDNA3.1 vector. 3xFLAG-Fig4 and -PIKfyve were cloned into pCMV-10 vector. The sequence for MBP was inserted into the vectors for PIKfyve or Vac14, as indicated in Fig. 1A, using Gibson Assembly (NEB).

Protein expression and purification. For EM specimens, constructs encoding 3xFLAG-PIKfyve(S2053E), His$_8$-Fig4, and 2xStrepII-Vac14 were co-transfected into Expi293F cells according to manufacturer instructions. Proteins were expressed for 48 hours after transfection, then harvested by centrifugation and flash-frozen for storage or immediately used for protein purification. Cells were lysed by 3 cycles of freezing and thawing in buffer containing 100 mM HEPES, 700 mM NaCl, 0.5 mM TCEP, 1 mM ATP, 1 mM $MgCl_2$, and 1x EDTA-free protease inhibitor (Roche), pH 7.8. Insoluble debris was removed by centrifugation at 15000 x g for 30 minutes. The supernatant was incubated with anti-FLAG M2 beads (Sigma) for 2 hours, then
washed with 3 x 10 bed volumes of buffer and eluted in 3 x 0.5 bed volume of buffer containing 0.25 mg/ml 3xFLAG peptide (APExBio). Elutions were immediately analyzed by negative-stain electron microscopy to assess sample quality and concentration. Grids were frozen immediately for cryoEM data collection.

For kinase and phosphatase enzymatic assays, constructs encoding 3xFLAG-tagged versions of PIKfyve (WT, S2053E, S2053A, and K1877E) were transfected into Expi293 cells according to manufacturer instructions and expressed for 48 hours. For formation of ternary complexes, 3xFLAG-Fig4 and 2xStrepII-Vac14 or 3xFLAGFig4(C486S) and

2xStrepII-Vac14 were co-transfected into Expi cells for 48 hours. Cell pellets were resuspended and lysed by freeze-thaw in buffer containing 100 mM HEPES, 500 mM NaCl, 0.5 mM TCEP, 1x EDTA-free protease inhibitor (Roche), pH 7.8. After centrifugation to remove insoluble material, supernatants were incubated with anti-FLAG M2 beads, washed with 3 x 10 bed volumes of buffer, then incubated overnight in 10 bed volumes buffer with 1 mM ATP and 1 mM $MgCl_2$ added. Beads were then washed again with 3 x 10 bed volumes of buffer, then eluted in 3 x 0.5 bed volume of buffer containing 0.25 mg/ml 3xFLAG peptide.

Specimen preparation and imaging by negative stain EM. Indicated protein samples were diluted to 50nM–100nM. 4ul of sample was loaded onto glow discharged copper grids coated with 10nm of carbon film. Samples were negatively stained with 2% of uranyl acetate and visualized on a FEI Tecnai T12 electron microscope operating at voltage of 120kV with a nominal magnification of 52000x (2.14 Å/pixel at specimen level). Images were further analyzed via RELION 3.0.4 (Zivanov et al., 2018) to obtain 2D class averages.

Cryo-EM specimen preparation and data collection (Table S1). Purified PIKfyve complex samples were supplemented with 0.02% ß-octylglucoside immediately before freezing and applied to Quantifoil Cu 300 mesh R1.2/1.3 grids glow discharged in residual air for 30 seconds at 20 mA. Grids were then blotted and plunge-frozen in liquid ethane cooled by liquid nitrogen using a Vitrobot Mark IV plunge-freezing robot (FEI) (Fig. S1B).

1913 movies were collected in super-resolution mode on an FEI Titan Krios at 300 kV equipped with a Gatan K2 Summit direct electron detector, using a nominal magnification of 130000x in super-resolution mode with a magnified pixel size of 1.05 Å on the specimen level (counting mode). Movies were dose-fractionated into 40 frames of 0.2 seconds each at a dose rate of 1.6 e^-/Å^2/frame for a total dose of 64 e^-/Å^2. All micrographs were collected with the stage tilted at a 30º angle to overcome a preferred particle orientation bias.

Data processing (Fig. S1 and S2). Motion correction for 1913 micrographs was performed in MotionCor2 (Zheng et al., 2017) with a binning factor of 2 and dividing micrographs into 5x5 patches. Global CTF calculation was performed with CTFFIND4.1 (Rohou and Grigorieff, 2015). 954 particles were manually picked and subjected to 2D reference-free classification in Relion 3.0.4 (Zivanov et al., 2018). Classes showing good particle definition were chosen as references for automated particle picking in Relion, yielding a dataset of 649,270 particles. Multiple rounds of 2D classification were used to remove ice contamination and bad particles, leaving 218356 particles representing 21 2D classes. These particles were used to generate

an initial model using the stochastic gradient descent algorithm as implemented in Relion. The resulting reference model was used for 3D classification and refinement in Relion. After Bayesian polishing, followed by further 3D classification, refinement, and post-processing, a final model centered on the Vac14 pentamer, comprising 53279 particles with a resolution of 5.25 Å (FSC=0.143 criterion), was obtained. The density of PIKfyve in the 5.25 Å map was diffuse and incomplete. To obtain a more complete map of the region around PIKfyve, particle subtraction was used in Relion to remove partial density for Vac14 and Fig4 from the particles, after which 2D classification was performed on the subtracted particles, yielding improved

alignment of the kinase region. Particle selection from these 2D classes was used to re-center the classes on the center of mass of the remaining density, closer to the kinase, and these were used to auto-pick a new dataset, which was subjected to 2D classification, initial modeling, 3D classification and refinement. This process of subtraction, re-centering, auto-picking, and re-processing was repeated twice more before a dataset of 614008 particles, centered close to the kinase, which showed improved density after modeling, was obtained. These were subjected to 2D classification with circular masking to remove ice and bad particles, which yielded a good dataset of 39125 particles. Particles from the best-defined 2D classes representing a range of different views were used for initial modeling by stochastic gradient descent. This model was used for 3D classification and refinement. After polishing and re-refinement, a model comprising 19998 particles was used for multibody refinement to independently refine the kinase and the region around Fig4 comprising two copies of Vac14, yielding maps of these regions with nominal resolutions of 6.6 and 5.1 Å according to the FSC=0.143 criterion, respectively, after

post-processing (Fig. S2B, C). Local resolution was estimated using the algorithm implemented in RELION 3.0.4, and much of the map for the kinase domain is estimated ~8-10 Å resolution by this means (Fig. S2D). We attribute the discrepancy in part to the inherent difficulty of measuring local resolution in cryoEM maps, which can vary between algorithms. Importantly, this map exhibits well-defined tubular densities that closely match the helical arrangements of the CCT and kinase modules, and allowed confident fitting of these modules, confirmed further by analysis of MBPtagged constructs by negative-stain EM.

Homology models of Fig4 Sac homology and PIKfyve kinase modules were obtained using RaptorX (Kallberg et al., 2012) against coordinates from PDB entries 4tu3 and 1e8x, respectively. The PIKfyve CCT domain was modeled using I-TASSER (Yang et al., 2015) against coordinates from PDB entry 3p9e. For Fig4, models were rigid-body fitted into the 5.1 Å cryoEM map, then manually adjusted in Coot (Emsley et al., 2010), followed by real-space refinement in Phenix (Adams et al., 2010). The PIKfyve kinase domain was rigid-body fitted into congruent density in the map of the kinase, then manually adjusted in Coot and real-space refined in Phenix. The PIKfyve CCT was split into separate models for the equatorial domain and the remainder of the module, which were rigid-body fitted independently to allow for the domains to rotate relative to one another. Vac14 helices were modeled de novo as poly-alanine into the 5.5 Å map using Coot, but their connectivity could not be ascertained from the density, nor sequence assigned.

Liposome preparation. For PIKfyve kinase enzymatic assays, substrate liposomes were prepared by mixing lipid stocks dissolved in chloroform in glass test tubes in the following molar ratio: 75% DOPC (Avanti Polar Lipids), 20% liver PE (Avanti Polar Lipids), 5% PI3P diC16 (Echelon Biosciences). Lipid mixtures were evaporated to dryness under a nitrogen stream, then dried further under vacuum for 30 minutes. Dried lipid films were rehydrated under 1 ml buffer (100 mM HEPES pH 7.8, 500 mM NaCl, 0.5 mM TCEP, 0.75 M sucrose) at 85°C for 30 minutes, then vortexed for 30 seconds to generate crude liposomes. Liposomes were subjected to 7 freeze-thaw cycles to eliminate multi-lamellar structures, then mixed with 2 volumes sucrose-free buffer and pelleted for 40 minutes at 16,000 x g. The resulting liposome pellet was resuspended in sucrose-free buffer and pelleted again for 30 minutes. The second pellet was resuspended to 5 mM total lipid concentration in sucrose-free buffer and used immediately.

Lipid kinase enzymatic assays—on liposome incorporated PI3P. Purified PIKfyve and Fig4/Vac14 samples were analyzed by SDS-PAGE and Coomassie staining, then quantitated by band densitometry against BSA standards. For complexes, PIKfyve WT or K1877E samples were mixed in equimolar amounts with Fig4/Vac14 complexes. All protein samples were diluted to a 100 nM final stock concentration (based on kinase concentration). Shortly before preparing reactions, liposomes were swollen by pelleting and resuspending in sucrose-free buffer containing 150 mM NaCl. Reaction mixtures were prepared by combining protein (10 nM final concentration), sucrose-free buffer, a 10x ATP/Mg^{2+}/Mn^{2+} solution (1 mM ATP, 20 mM $MgCl_2$, and 5mM $MnCl_2$ final concentration), and ^{32}P-ATP (2.5 uCi per reaction), then adding substrate liposomes to a final concentration of 2.5 mM total lipid. Reactions were incubated at room temperature for one hour, then removed to tubes containing EDTA (10 mM final) and proteinase K (0.1 mg/ml final) and incubated for 15 minutes at room temperature. Liposomes were then pelleted by centrifugation for 15 minutes at 16,000 x g. Pellets were resuspended in 100 µl buffer, then transferred to scintillation vials for measurement of ^{32}P radioactivity in a scintillation counter.

Lipid kinase enzymatic assay –on soluble PI3P lipids. For the assays on soluble diC6-PI3P, the protein samples were diluted to 40nM final stock concentration (based on PIKfyve quantitation). Shortly before preparing reactions, green fluorophore labeled C6-C6-BODIPY-FL-PI3P (Echelon Biosciences) was dissolved in water to make a 50□M stock solution. Reaction mixtures (20 µl total volume) were prepared by combining PIKfyve or the PIKfyve complex (10 nM final concentration) with diC6-PI3P (20 µM final concentration) in buffer (100 mM HEPES, pH 7.8, 150 mM NaCl, 0.5mM TCEP) supplemented with 1 mM ATP, 2 mM MgCl2, and 0.5 mM $MnCl_2$. The reactions were incubated at room temperature for 1.5 hours and terminated by introducing ten volumes of Chloroform:Methanol (1:2). The samples were dried by SpeedVac (ThermoFisher) at 35°C for two hours, then dissolved in chloroform and separated by thin layer chromatography as in (Taylor and Dixon, 2001). The phosphoinositide spots were visualized under ultraviolet light and quantitated fluorometrically, using ImageJ.

Lipid phosphatase enzymatic assays. Purified PIKfyve was mixed with purified Fig4/Vac14 complexes to achieve an equimolar ratio of PIKfyve to Fig4, with a final concentration of 100 nM ternary complex. For Fig4/Vac14 only assays, Fig4/Vac14 complexes were directly diluted to 100 nM. Reactions were carried out in a 50 µl volume containing 50 nM protein complex, 50 µM diC8 PI3P or $PI(3,5)P_2$ (Echelon Biosciences), and 2 mM $MgCl_2$ for 1 hour at 37°C. Released phosphate was quantitated using a malachite green colorimetric assay in 96-well plate format according to the manufacturer’s instructions (Cayman Chemical #30412051), with measurements performed on a BioTek Synergy H1M microplate reader.

PIKfyve phosphosite analysis by mass spectrometry. For *in vitro* phosphorylation/dephosphorylation analysis, purified PIKfyve (WT or K1877E) and Fig4 (WT and C486S)/Vac14 complex samples were quantitated by band densitometry against BSA standards after SDS-PAGE and Coomassie staining. PIKfyve WT or K1877E samples were mixed in equimolar amounts with Fig4 (WT or C486S)/Vac14 complexes to give four different combinations. Samples were incubated in the presence of 1 mM ATP, 2 mM $MgCl_2$, and 0.5 mM $MnCl_2$ for 1 hour at room temperature. After incubation, samples were resolved by SDS-PAGE and stained with Coomassie Brilliant Blue. PIKfyve bands were excised from the gels after extensive washing in deionized water, and submitted to the University of Alabama-Birmingham Proteomics core facility for tryptic digestion and phosphopeptide identification by MS/MS. Samples of PIKfyve/Fig4/Vac14 and PIKfyve/Fig4(C486S)/Vac14 complexes produced by co-transfection in Expi293 cells were similarly prepared and submitted for phosphosite analysis at the University of Alabama-Birmingham Proteomics core facility.

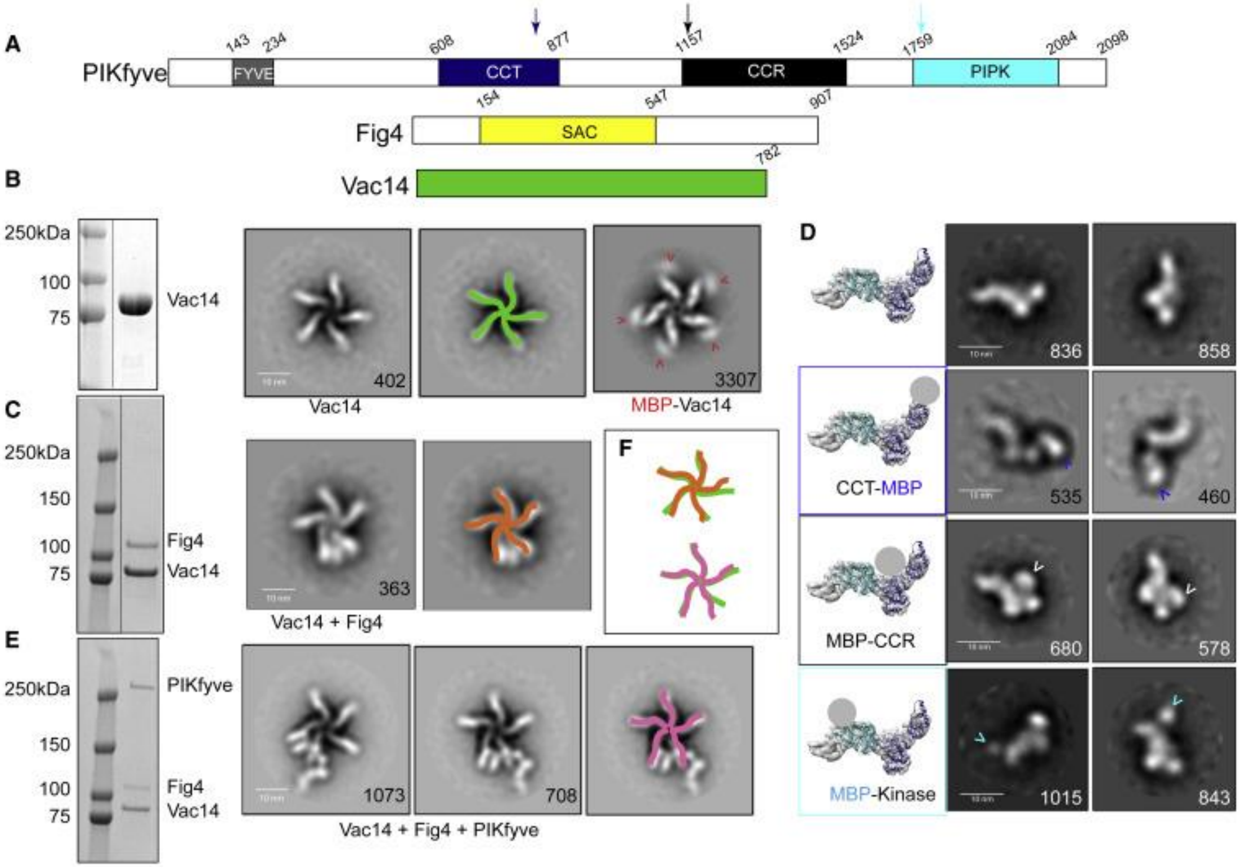

Figure 3.1. Assembly and gross architecture of the human PIKfyve complex by negative stain EM analysis. (**A**) Domain organization of PIKfyve, Fig4, and Vac14. (**B**) The Vac14 sample used for negative staining EM is pure as per SDS-PAGE. 2D class averages of Vac14 or MBP-Vac14 show that it pentamerizes. Numbers of particles for each class average are indicated. Maltose binding protein (MBP) fused to the Vac14 N-terminus is at the tip of the Vac14 "leg". (**C**) The Fig4/Vac14 sample used for negative staining EM is pure per SDS-PAGE. 2D class averages of Fig4/Vac14 show density for Fig4 between two Vac14 "legs". (**D**) Negative stain EM analysis of PIKfyve or

MBP+PIKfyve fusions. MBP was inserted into the PIKfyve sequence as indicated by arrows in 1A. The left-most column shows PIKfyve density from the cryo-EM maps (Fig. 2) with docked models of the CCT and kinase modules; the location of MBP in the class averages is indicated as a grey ball. The other columns show 2D class averages of PIKfyve by itself or with MBP-insertions. (**E**) The PIKfyve/Fig4/Vac14 sample used for negative staining and cryo-EM is pure per SDS-PAGE. 2D class averages of PIKfyve/Fig4/Vac14, showing that PIKfyve binds close to Fig4 at the tip of the Vac14 legs. (**F**) Schematic overlay of the Vac14 pentamers in Vac14, Fig4/Vac14, and PIKfyve/Fig4/Vac14, showing that the 5-fold symmetry of the Vac14 pentamer is distorted in the Fig4/Vac14 and PIKfyve/Fig4/Vac14 complexes.

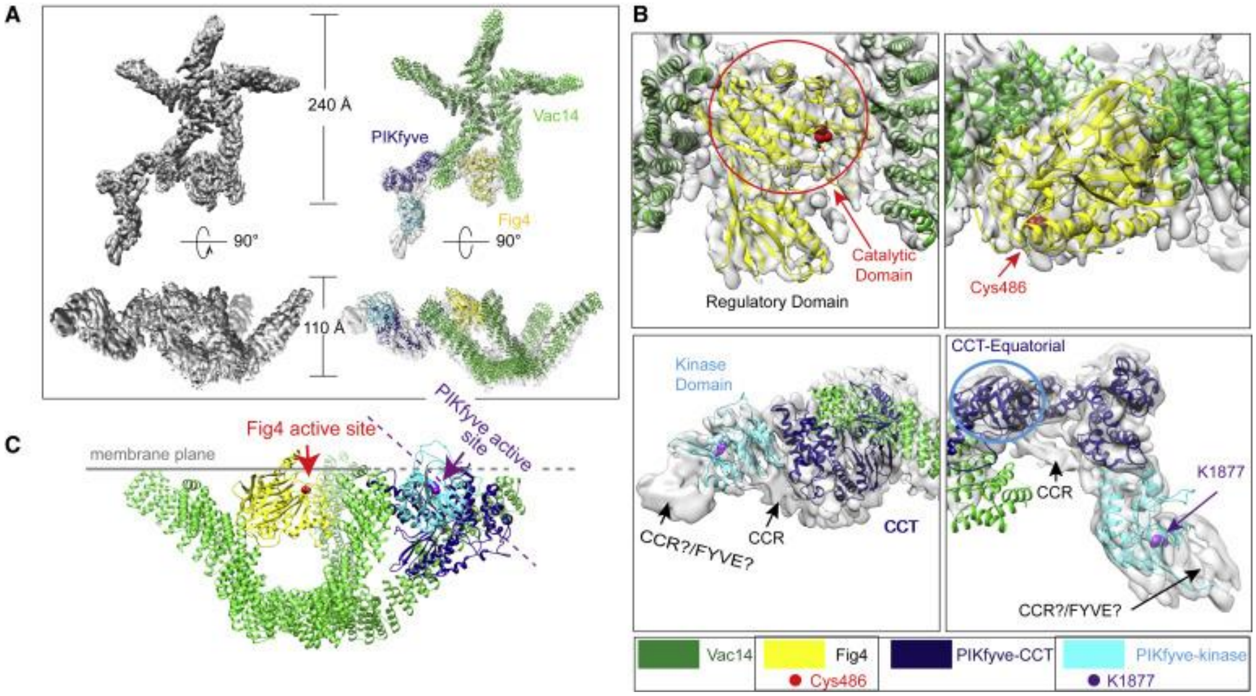

Figure 3.2. **Cryo-EM reconstruction of the human PIKfyve complex at medium-low resolution.** (**A**) The composite reconstruction (see text and Methods) alone and with the model. The left panels show the maps only, and the right panels also shows docked protein models colored according to panel 1A. (**B**) Enlarged views showing the fit of the Fig4 Sac homology module (top panels) and the PIKfyve CCT and kinase modules (bottom panels) to the map. Two different views for Fig4 and PIKfyve are related by 90° rotations. (**C**) Model for PIKfyve complex interacting with membrane. The Fig4 active site is oriented to face the membrane, whereas the PIKfyve active site is twisted away from the membrane by ~45° and so cannot access membrane incorporated phosphoinositides.

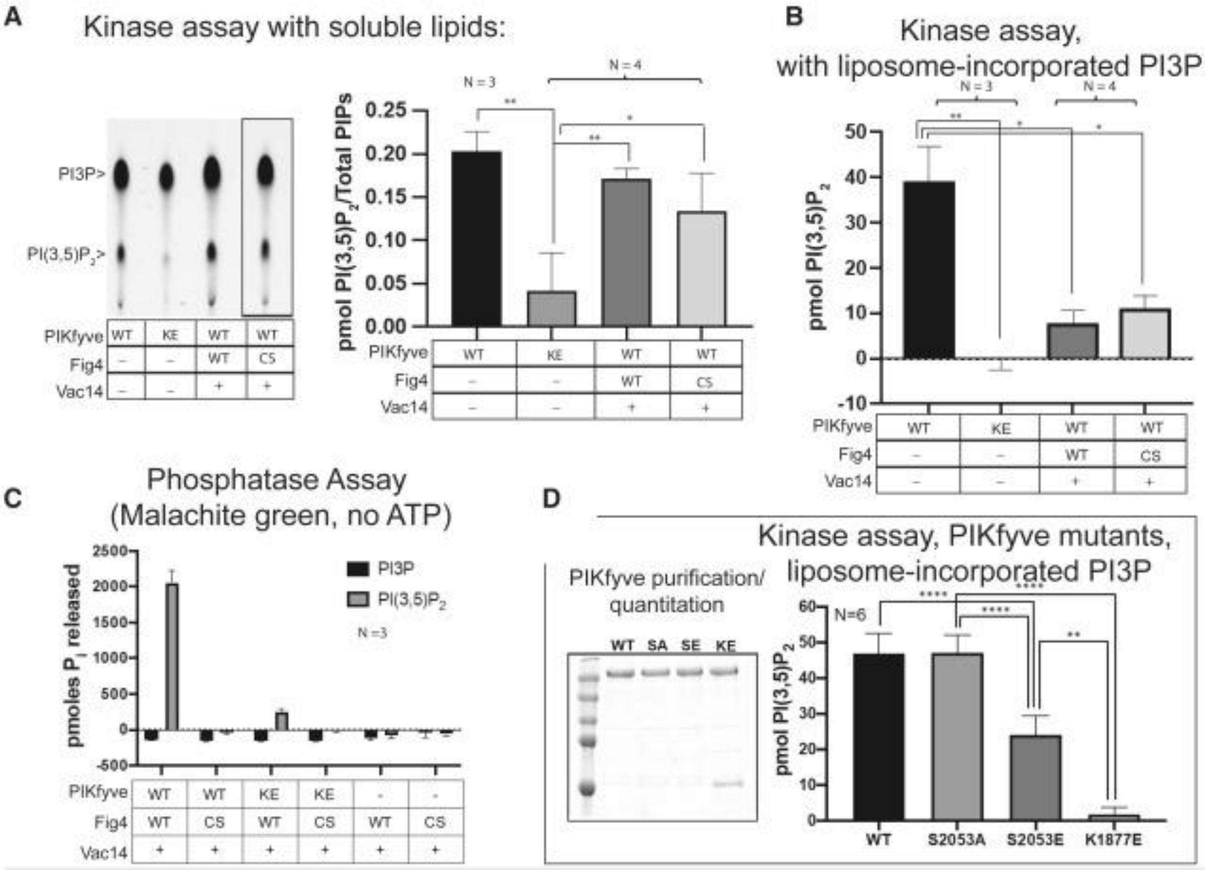

PIKfyve **KE**= catalyically inactivated PIKFyve mutant **K1877E**; Fig4 **CS**= catalytically inactivated Fig4 mutant **C486S**. **SA**= PIKfyve **S2053A; SE**= PIKFyve **S2053E**.

Figure 3.3. Complex formation affects the enzymatic activities of PIKfyve and Fig4 with respect to phosphoinositide lipids. (**A**) PIKfyve alone and in the PIKfyve/Fig4/Vac14 complex phosphorylate soluble C6-C6-BODIPY-FL-PI3P with similar efficiency, independent of whether the lipid phosphatase Fig4 is catalytically active (WT) or not (C486S). (**B**) PIKfyve alone phosphorylates liposome incorporated PI3P in a radiometric assay more efficiently that the PIKfyve/Fig4/Vac14 complex. A plausible explanation is that the PIKfyve active site is sterically constrained in the

complex and so unable to access membrane-incorporated PI3P. (**C**) In a malachite green assay monitoring dephosphorylation of soluble di-C8 PI(3,5)P_2, robust Fig4 lipid phosphatase activity was observed only for Fig4 in a complex with WT PIKfyve. Complexes comprising a catalytically inactivated PIKfyve mutant (K1877E) were significantly less active, and a binary complex lacking PIKfyve was the least active. (**D**) PIKfyve lipid kinase activity is inhibited when Ser2053 in the kinase activation loop is mutated to glutamate to mimic its phosphorylation but not when it is changed to alanine. Experiments were carried out at least 3 times, as indicated. Significance determined by Welch’s t-test.

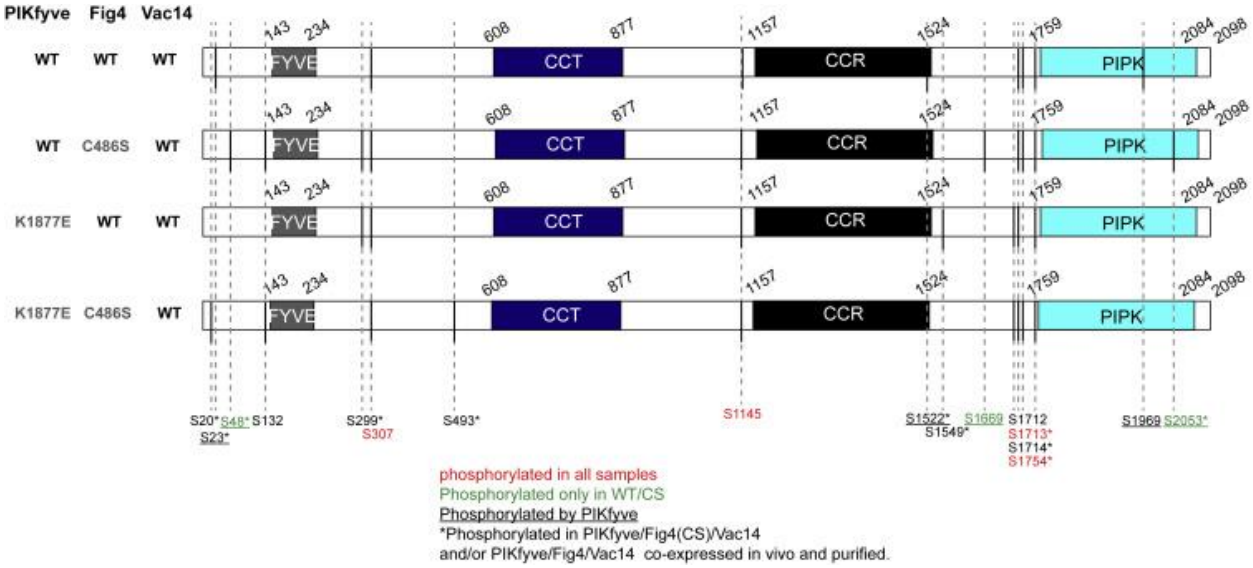

Figure 3.4. **PIKfyve autophosphorylates itself, and Fig4 is also a protein phosphatase that dephosphorylates PIKfyve**. Samples of WT PIKfyve or a catalytically inactivated mutant (K1877E) were mixed in equimolar amounts with Fig4 (WT or C486S)/Vac14 complexes to give four different combinations. Samples were incubated in the presence of 1 mM ATP, then resolved by SDS-PAGE. The gels were stained and the bands corresponding to PIKfyve were excised and submitted to the University of Alabama-Birmingham Proteomics core facility for tryptic digestion and phosphopeptide identification by MS/MS. Samples produced by co-expressing all three proteins, including either WT or catalytically inactivated Fig4 (C486S), were similarly prepared and submitted to the same core facility for PIKfyve phosphosite analysis. Ser23, Ser28, Ser1522, Ser1669, Ser1969, and Ser2053 were phosphorylated in complexes containing WT PIKfyve but not catalytically inactivated K1877E mutant. PIKfyve lipid kinase activity is inhibited when Ser2053, in the kinase activation loop, is mutated to glutamate to mimic its phosphorylation (in Fig. 3D). Importantly, Ser2053 is

among sites that are dephosphorylated in complexes containing WT Fig4 but not a catalytically inactivated (C486S) mutant. This suggests a model where Fig4 activates PIKfyve by dephosphorylating PIKfyve's activation loop Ser2053, explaining why maximal PI(3,5)P_2 production in vivo requires catalytically active Fig4.

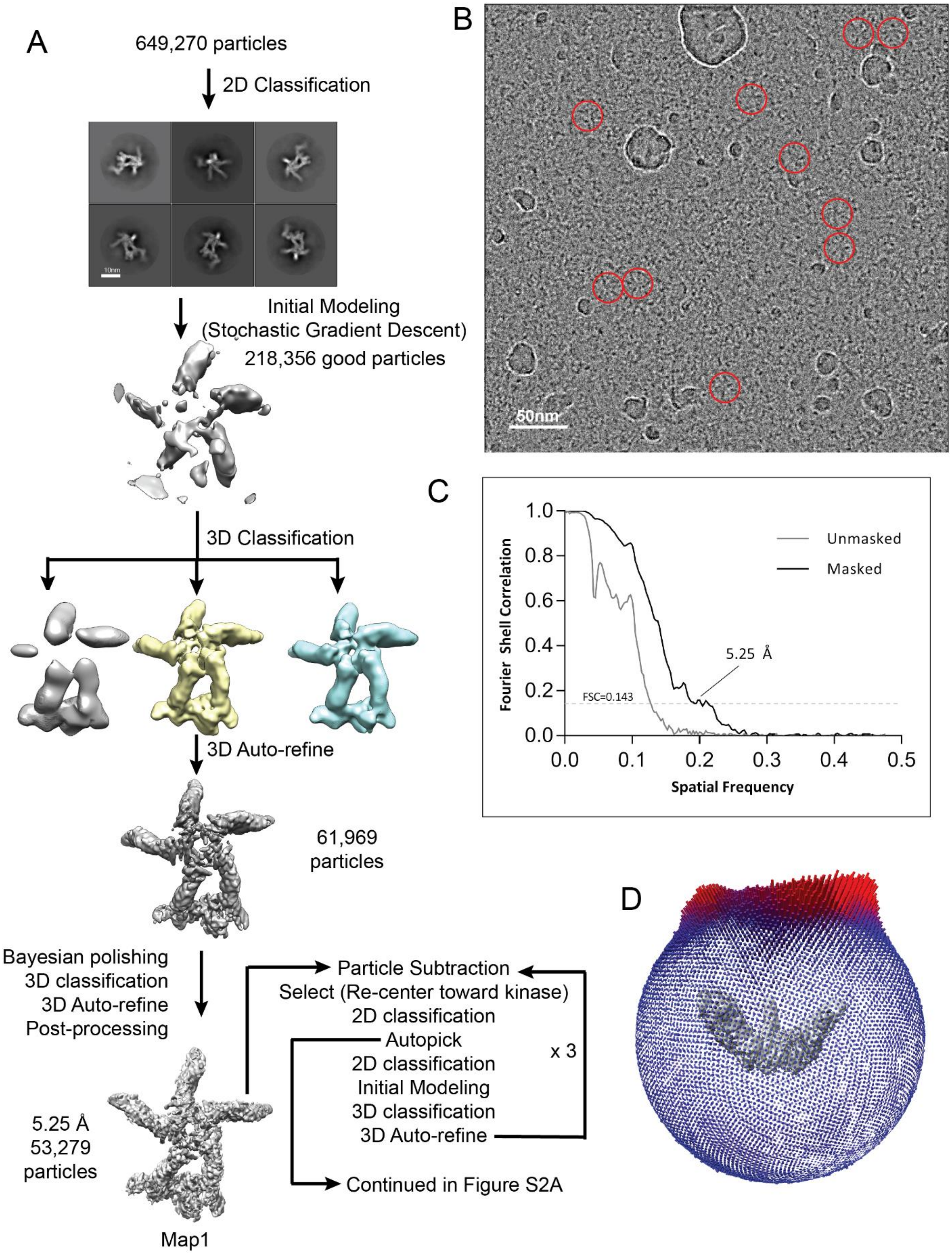
A
649,270 particles
2D Classification
10nm
Initial Modeling
(Stochastic Gradient Descent)
218,356 good particles
3D Classification
3D Auto-refine
61,969
particles
Bayesian polishing
3D classification
3D Auto-refine
Post-processing
5.25 Å
53,279
particles
Map1
Particle Subtraction
Select (Re-center toward kinase)
2D classification
Autopick
2D classification
Initial Modeling
3D classification
3D Auto-refine
x 3
Continued in Figure S2A
B
50nm
C
Fourier Shell Correlation
1.0
0.8
0.6
0.4
0.2
0.0
Unmasked
Masked
5.25 Å
FSC=0.143
0.0
0.1
0.2
0.3
0.4
0.5
Spatial Frequency
D

Figure S3.1: CryoEM work flow (part 1). (**A**) Cryo-EM work flow resulting in a map centered on the Vac14 pentamer (map1) nominally at 5.25 Å resolution. (**B**) Representative raw micrograph as collected on a FEI Titan Krios at 300 kV equipped with a Gatan K2 Summit direct electron detector. Particles picked for initial 2D classification are circled. See method section for more details. (**C**) FSC curves after gold standard refinement for masked and unmasked map1 (centered on Vac14 pentamer). FSC cutoff at 0.143 is shown by a dashed line. (**D**) Particle orientation distribution of map1.

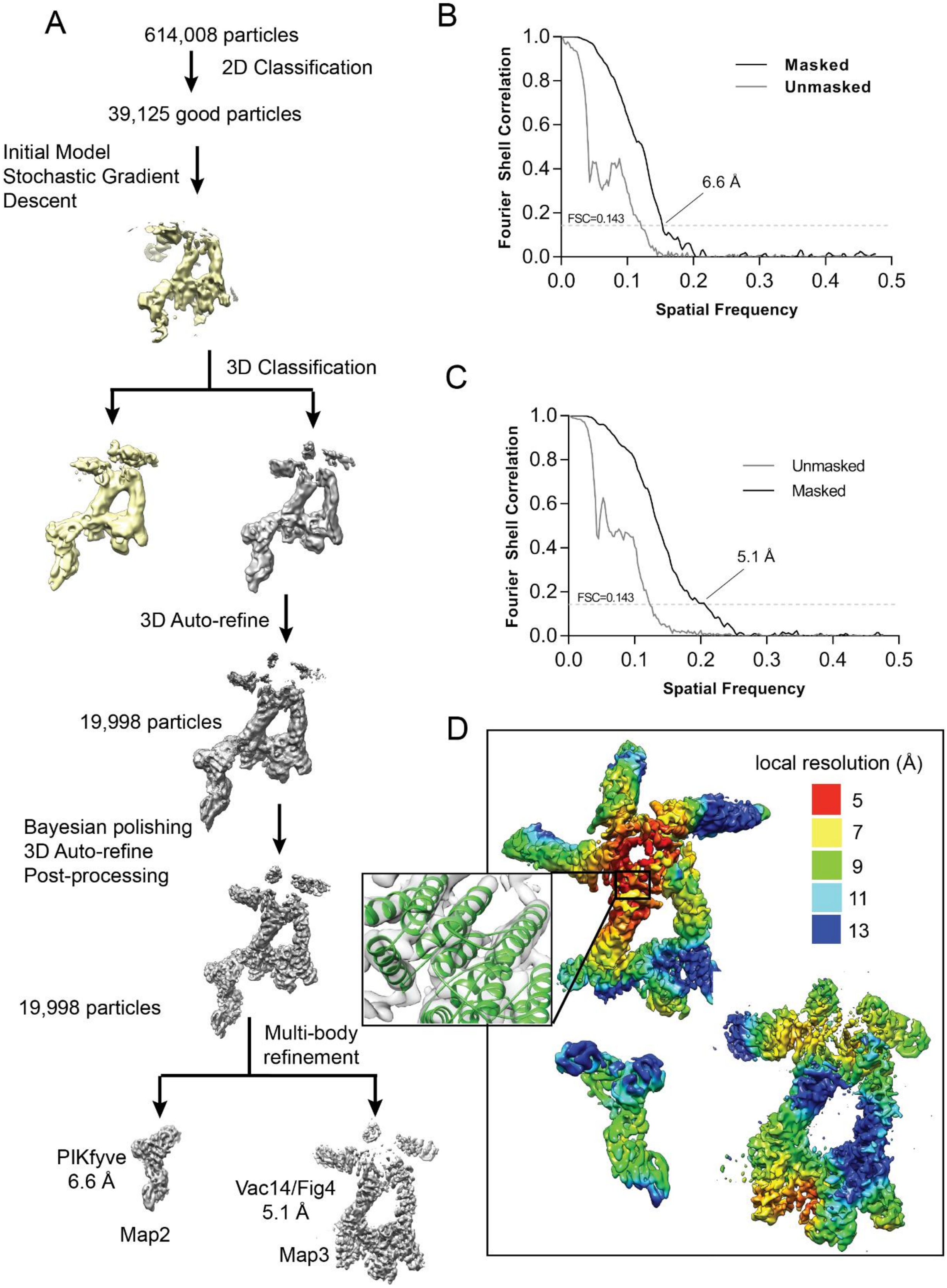
A
614,008 particles
2D Classification
39,125 good particles
Initial Model
Stochastic Gradient
Descent
3D Classification
3D Auto-refine
19,998 particles
Bayesian polishing
3D Auto-refine
Post-processing
19,998 particles
Multi-body
refinement
PIKfyve
6.6 Å
Map2
Vac14/Fig4
5.1 Å
Map3
B
Fourier Shell Correlation
Spatial Frequency
Masked
Unmasked
6.6 Å
FSC=0.143
1.0
0.8
0.6
0.4
0.2
0.0
0.0
0.1
0.2
0.3
0.4
0.5
C
Fourier Shell Correlation
Spatial Frequency
Unmasked
Masked
5.1 Å
FSC=0.143
1.0
0.8
0.6
0.4
0.2
0.0
0.0
0.1
0.2
0.3
0.4
0.5
D
local resolution (Å)
5
7
9
11
13

Figure S3.2: CryoEM work flow (part2). (**A**) Cryo-EM work flow, continued from FigS1A, for maps centered on PIKfyve (map2, nominally at 6.6 Å resolution) and Fig4 (map3, nominally at 5.1 Å resolution). See method section for more details. (**B**) FSC curves after gold standard refinement for masked and unmasked map2. (**C**) FSC curves after gold standard refinement for masked and unmasked map3. (**D**) Maps colored by local resolution. The discrepancy between the FSC=0.143 and local resolution estimate for PIKfyve in map 2 is discussed in the Methods. Importantly, the map exhibits well-defined tubular densities that closely match the helical arrangements of the CCT and kinase modules, and allowed confident fitting of these modules. The fitting was further confirmed by analysis of MBP-tagged constructs by negative-stain EM. The inset shows Vac14 helices placed into density from higher resolution portions of Map 1.

Table S3.1

Data collection and processing	**Map1**	**Map2**	**Map3**
Magnification	130000x	130000x	130000x
Voltage (kV)	300	300	300
Electron exposure (e^{-}/Å^2)	64	64	64
Defocus range (µm)	-1.5 to -3.5	-1.5 to -3.5	-1.5 to -3.5
Pixel size (Å)	1.05	1.05	1.05
Symmetry imposed	C1	C1	C1
Initial particle images (no.)	649270	614008	614008

Final particle images (no.)	53279	19998	19998
Map resolution (Å)	5.25	6.6	5.1
FSC threshold	0.143	0.143	0.143

Table S3.2:

REAGENT or RESOURCE	**SOURCE**	**IDENTIFIER**
Chemicals, Peptides, and Recombinant Proteins		
cOmplete™, EDTA-free Protease Inhibitor Cocktail	Roche Applied Science	Cat # 11873580001
3X (DYKDDDDK) Peptide	APExBio	Cat # A6001
Critical Commercial Assays		
Gibson Assembly® Master Mix	New England BioLabs	Cat # E2611S
ANTI-FLAG® M2 Affinity Gel	Sigma Aldrich	Cat # A2220
Octyl-beta-Glucoside Detergent	Thermo Fisher	Cat # 28310
18:1 (Δ9-Cis) PC (DOPC)	Avanti Polar Lipids	Cat # 850375
16:0-18:1 PE	Avanti Polar Lipids	Cat # 850757

PI3P diC16	Echelon Biosciences	Cat # P-3016
PI(3,5)P_2 diC16	Echelon Biosciences	Cat # P-3516
PI3P diC8	Echelon Biosciences	Cat # P-3008
PI(3,5)P_2 diC8	Echelon Biosciences	Cat # P-3508
C6-C6-BODIPY-FL-PI3P	Echelon Biosciences	Cat # C-03F6
C6-C6-BODIPY-FL-PI(3,5)P_2	Echelon Biosciences	Cat # C-35F6
Malachite Green Phosphate Assay Kit	Cayman Chemical	Cat # 10009325
Deposited Data		
PIKfyve complex centered on Vac14 - map1	This paper	EMD: 22634
Vac14 backbone models	This paper	PDB: 7K1Y
PIKfyve complex centered on PIKfyve - map2	This paper	EMD: 22647
PIKfyve Kinase domain, CCT domain models	This paper	PDB: 7K2V
PIKfyve complex centered on Fig4 – map3	This paper	EMD: 22631
Fig4 Sac homology domain model	This paper	PDB: 7K1W
Experimental Models: Cell Lines		
Expi293F™ Cells	Gibco™ Thermo Fisher	Cat # A14527
Oligonucleotides		

Primers for Recombinant DNA, see Table S2	This paper	N/A
Recombinant DNA		
Construct of wildtype Vac14, Fig4, PIKfyve	L. Weisman	N/A
Plasmid: pcDNA3.1 - 2xStrepII-tagged Vac14	This paper	N/A
Plasmid: pcDNA3.1 - 2xStrepII-tagged Vac14 - MBP	This paper	N/A
Plasmid: pcDNA3.1 - His-tagged Fig4 -WT	This paper	N/A
Plasmid: pcDNA3.1 - His-tagged Fig4 -CS	This paper	N/A
Plasmid: pCMV-10 - 3xFLAG-Fig4 - WT	This paper	N/A
Plasmid: pCMV-10 - 3xFLAG-Fig4 - CS	This paper	N/A
Plasmid: pCMV-10 - 3xFLAG-PIKfyve - WT	This paper	N/A
Plasmid: pCMV-10 - 3xFLAG-PIKfyve – S2053E	This paper	N/A
Plasmid: pCMV-10 - 3xFLAG-PIKfyve – S2053A	This paper	N/A

Plasmid: pCMV-10 - 3xFLAG-PIKfyve – K1877E	This paper	N/A
Plasmid: pCMV-10 - 3xFLAG-PIKfyve – 722-MBP-723	This paper	N/A
Plasmid: pCMV-10 - 3xFLAG-PIKfyve – 1192-MBP-1193	This paper	N/A
Plasmid: pCMV-10 - 3xFLAG-PIKfyve – 1806-MBP-1807	This paper	N/A
Software and Algorithms		
ImageJ	Schneider et al., 2012	https://imagej.nih.gov/ij/
RELION 3.0.4	Zivanov et al., 2018	DOI: 10.7554/eLife.42166
RaptorX	Kallberg et al., 2012	http://raptorx.uchicago.edu/
I-TASSER	Yang et al., 2015	https://zhanglab.ccmb.med.umich.edu/I-TASSER/
Other		
Quantifoil®, Orthogonal Array of 1.2µm Diameter Holes - 1.3µm Separation, mounted on a 300M Cu grid	TED PELLA, INC	Cat # 658-300-Cu

Table S3.3: Recombinant DNA and primers:

2xStrepII-tagged Vac14
ATATAGATCTATGAACCCCGAGAAGGATTTCG ATATGCGGCCGCTCATCAGAGGACAACCCTCCGG
2xStrepII-tagged Vac14 - MBP
ACGATGACAAGCTTGCGGCCGCAAACCCCGAGAAGGATTTCG TCGATTTTGAGGACAACCCTCCGGTC GGTTGTCCTCAAAATCGAAGAAGGTAAACTGG AGGGATGCCACCCGGGATCCTTAAGTCTGCGCGTCTTTCAG
His-tagged Fig4 -WT
ATATGTCGACATGCCCACGGCCGCCG ATATCTCGAGCAGGTAGCGGTTCCTGATGTACTC
His-tagged Fig4 -CS
GCATCCTTCGAACCAACAGTGTGGACTGTTTAGAT ATCTAAACAGTCCACACTGTTGGTTCGAAGGATGC
3xFLAG-PIKfyve - WT
ATATGTCGACATGGCCACAGATGATAAGACGTC ATATGCGGCCGCTCAGCAATTCAGACCCAAGCCTGTC
3xFLAG-PIKfyve – S2053E
TGGGACAAAAAGCTTGAGATGGTTGTGAAAGAGACAGGAATTTTAGGTGGAC GTCCACCTAAAATTCCTGTCTCTTTCACAACCATCTCAAGCTTTTTGTCCCA
3xFLAG-PIKfyve – S2053A
GACAAAAAGCTTGAGATGGTTGTGAAAGCAACAGGAATTTTAGG CCTAAAATTCCTGTTGCTTTCACAACCATCTCAAGCTTTTTGTC
3xFLAG-PIKfyve – K1877E

GCGGGAGAGTTTCATGAGATGCGTGAAGTGATTC GAATCACTTCACGCATCTCATGAAACTCTCCCGC
3xFLAG-PIKfyve – 722-MBP-723
CGCGCAGACTTGCATTGATCCTATTGTGCTTCAG CTTCGATTTTAGTAAACTTAGTTTCTTCTCTGTAGAG TAAGTTTACTAAAATCGAAGAAGGTAAACTGGTAATCTGGATTAACG GATCAATGCAAGTCTGCGCGTCTTTCAGGGCTT
3xFLAG-PIKfyve – 1192-MBP-1193
CGCGCAGACTGAGAGAGGGCTTATTCTGAG CTTCGATTTTTTCATCACCCTCATTTTTGC GGGTGATGAAAAAATCGAAGAAGGTAAACTGG GCCCTCTCTCAGTCTGCGCGTCTTTCAG
3xFLAG-PIKfyve – 1806-MBP-1807
CGCGCAGACTCCTCATGTGGAACTTCAATTTTC CTTCGATTTTATTTATGAGTTGCTTCTTTTGTG ACTCATAAATAAAATCGAAGAAGGTAAACTGG CCACATGAGGAGTCTGCGCGTCTTTCAG

Reference

Adams, P.D., Afonine, P.V., Bunkoczi, G., Chen, V.B., Davis, I.W., Echols, N., Headd, J.J., Hung, L.W., Kapral, G.J., Grosse-Kunstleve, R.W., *et al.* (2010). PHENIX: a comprehensive Python-based system for macromolecular structure solution. Acta Crystallogr D Biol Crystallogr *66*, 213-221.

Botelho, R.J., Efe, J.A., Teis, D., and Emr, S.D. (2008). Assembly of a Fab1 phosphoinositide kinase signaling complex requires the Fig4 phosphoinositide phosphatase. Mol Biol Cell *19*, 4273-4286.

Chow, C.Y., Landers, J.E., Bergren, S.K., Sapp, P.C., Grant, A.E., Jones, J.M., Everett, L., Lenk, G.M., McKenna-Yasek, D.M., Weisman, L.S., *et al.* (2009). Deleterious variants of FIG4, a phosphoinositide phosphatase, in patients with ALS. Am J Hum Genet *84*, 85-88.

Chow, C.Y., Zhang, Y., Dowling, J.J., Jin, N., Adamska, M., Shiga, K., Szigeti, K., Shy, M.E., Li, J., Zhang, X., *et al.* (2007). Mutation of FIG4 causes neurodegeneration in the pale tremor mouse and patients with CMT4J. Nature *448*, 68-72.

Currinn, H., Guscott, B., Balklava, Z., Rothnie, A., and Wassmer, T. (2016). APP controls the formation of PI(3,5)P(2) vesicles through its binding of the PIKfyve complex. Cell Mol Life Sci *73*, 393-408.

Duex, J.E., Nau, J.J., Kauffman, E.J., and Weisman, L.S. (2006). Phosphoinositide 5-phosphatase Fig 4p is required for both acute rise and subsequent fall in stress-induced phosphatidylinositol 3,5-bisphosphate levels. Eukaryot Cell *5*, 723-731.

Emsley, P., Lohkamp, B., Scott, W.G., and Cowtan, K. (2010). Features and development of Coot. Acta Crystallogr D Biol Crystallogr *66*, 486-501.

Gayle, S., Landrette, S., Beeharry, N., Conrad, C., Hernandez, M., Beckett, P., Ferguson, S.M., Mandelkern, T., Zheng, M., Xu, T., *et al.* (2017). Identification of apilimod as a firstin-class PIKfyve kinase inhibitor for treatment of B-cell non-Hodgkin lymphoma. Blood *129*, 1768-1778.

Hasegawa, J., Strunk, B.S., and Weisman, L.S. (2017). PI5P and PI(3,5)P2: Minor, but Essential Phosphoinositides. Cell Struct Funct *42*, 49-60.

Hulseberg, C.E., Feneant, L., Szymanska-de Wijs, K.M., Kessler, N.P., Nelson, E.A., Shoemaker, C.J., Schmaljohn, C.S., Polyak, S.J., and White, J.M. (2019). Arbidol and Other Low-Molecular-Weight Drugs That Inhibit Lassa and Ebola Viruses. J Virol *93*.

Ikonomov, O.C., Sbrissa, D., Compton, L.M., Kumar, R., Tisdale, E.J., Chen, X., and Shisheva, A. (2015). The Protein Complex of Neurodegeneration-related Phosphoinositide Phosphatase Sac3 and ArPIKfyve Binds the Lewy Body-associated Synphilin-1, Preventing Its Aggregation. J Biol Chem *290*, 28515-28529.

Ikonomov, O.C., Sbrissa, D., Fenner, H., and Shisheva, A. (2009). PIKfyve-ArPIKfyve-Sac3 core complex: contact sites and their consequence for Sac3 phosphatase activity and endocytic membrane homeostasis. J Biol Chem *284*, 35794-35806.

Jin, N., Lang, M.J., and Weisman, L.S. (2016). Phosphatidylinositol 3,5-bisphosphate: regulation of cellular events in space and time. Biochem Soc Trans *44*, 177-184.

Kallberg, M., Wang, H., Wang, S., Peng, J., Wang, Z., Lu, H., and Xu, J. (2012). Templatebased protein structure modeling using the RaptorX web server. Nat Protoc *7*, 1511-1522.

Malia, P.C., Numrich, J., Nishimura, T., Gonzalez Montoro, A., Stefan, C.J., and Ungermann, C. (2018). Control of vacuole membrane homeostasis by a resident PI-3,5-kinase inhibitor. Proc Natl Acad Sci U S A *115*, 4684-4689.

Mayer, L., Jasztal, M., Pardo, M., Aguera de Haro, S., Collins, J., Bariana, T.K., Smethurst, P.A., Grassi, L., Petersen, R., Nurden, P., *et al.* (2018). Nbeal2 interacts with Dock7, Sec16a, and Vac14. Blood *131*, 1000-1011.

Myers, M.P., Stolarov, J.P., Eng, C., Li, J., Wang, S.I., Wigler, M.H., Parsons, R., and Tonks, .K. (1997). P-TEN, the tumor suppressor from human chromosome 10q23, is a dual-specificity phosphatase. Proc Natl Acad Sci U S A *94*, 9052-9057.

Nelson, E.A., Dyall, J., Hoenen, T., Barnes, A.B., Zhou, H., Liang, J.Y., Michelotti, J., Dewey, W.H., DeWald, L.E., Bennett, R.S., *et al.* (2017). The phosphatidylinositol-3-phosphate 5-kinase inhibitor apilimod blocks filoviral entry and infection. PLoS Negl Trop Dis *11*, e0005540.

Rohou, A., and Grigorieff, N. (2015). CTFFIND4: Fast and accurate defocus estimation from electron micrographs. J Struct Biol *192*, 216-221.

Sbrissa, D., Ikonomov, O.C., and Shisheva, A. (2000). PIKfyve lipid kinase is a protein kinase: downregulation of 5'-phosphoinositide product formation by autophosphorylation. Biochemistry *39*, 15980-15989.

Schulze, U., Vollenbroker, B., Braun, D.A., Van Le, T., Granado, D., Kremerskothen, J., Franzel, B., Klosowski, R., Barth, J., Fufezan, C., *et al.* (2014). The Vac14-interaction network is linked to regulators of the endolysosomal and autophagic pathway. Mol Cell Proteomics *13*, 1397-1411.

Shisheva, A., Sbrissa, D., Hu, B., and Li, J. (2019). Severe Consequences of SAC3/FIG4 Phosphatase Deficiency to Phosphoinositides in Patients with Charcot-Marie-Tooth Disease Type-4J. Mol Neurobiol *56*, 8656-8667.

Strunk, B.S., Steinfeld, N., Lee, S., Jin, N., Munoz-Rivera, C., Meeks, G., Thomas, A., Akemann, C., Mapp, A.K., MacGurn, J.A., *et al.* (2020). Roles for a lipid phosphatase in the activation of its opposing lipid kinase. Mol Biol Cell, mbcE18090556.

Taylor, G.S., and Dixon, J.E. (2001). An assay for phosphoinositide phosphatases utilizing fluorescent substrates. Anal Biochem *295*, 122-126.

Yang, J., Yan, R., Roy, A., Xu, D., Poisson, J., and Zhang, Y. (2015). The I-TASSER Suite: protein structure and function prediction. Nat Methods *12*, 7-8.

Zheng, S.Q., Palovcak, E., Armache, J.P., Verba, K.A., Cheng, Y., and Agard, D.A. (2017).

MotionCor2: anisotropic correction of beam-induced motion for improved cryo-electron microscopy. Nat Methods *14*, 331-332.

Zivanov, J., Nakane, T., Forsberg, B.O., Kimanius, D., Hagen, W.J., Lindahl, E., and Scheres, S.H. (2018). New tools for automated high-resolution cryo-EM structure determination in RELION-3. Elife *7*.

Chapter 4 Investigation of VPS13 interaction with acceptor membrane

LTP localization at MCS aids in the selective and directional transfer of lipids. Lipids are first extracted from the donor membrane, then transferred across the cytosolic space, and finally inserted into the acceptor membrane. As a soluble protein without transmembrane region, VPS13 likely interacts with additional protein machinery at both membranes to perform the extraction and insertion step. To better understand these processes, the nature of the interactions between VPS13 and these proteins must be characterized. Several domains and motifs are found to mediate the interaction of VPS13 with membranes in humans. An FFAT motif at loops in the N-terminal halves of VPS13A and VPS13C tethers the protein to the ER by interacting with the ER-resident VAMP-associated protein (VAP). The WD40-like domain at the C-terminal end drives VPS13C localization to endolysosomal membranes (Kumar et al., 2018). Additionally, the C-terminal PH-DH domain recruits VPS13A to mitochondria, while this domain in VPS13A and VPS13C recruits them to lipid droplets (Kumar et al., 2018). The slight sequence variations in these conserved domains may contribute to the specific localization patterns of the VPS13 isoforms to different contact sites. In yeast, Mcp1, Ypt35, and Spo71 have been identified as proteins responsible for recruiting VPS13 to mitochondria, the endosome, or the prospore membrane, respectively. The three proteins use a similar PxP motif to interact with the WD40-like domain of VPS13. The three proteins competitively recruit VPS13 to different contact sites by varying their expression levels (Bean et al., 2018). The WD40-like domain in VPS13 is reminiscent of another WD40 protein, WIPI4, which is an interacting partner of ATG2 in humans. ATG2 is recruited to autophagosomes by interacting with WIPI4, which interacts with PI3P localized on autophagosome. It is intriguing to speculate that VPS13, when functioning alone, might mimic the function of an ATG2-WIPI4 complex. It is also possible that the VPS13 WD40 domain may play a direct role in lipid transfer to the acceptor organelle membrane. To better understand how VPS13 MCS localization is regulated by interaction with protein partners at different acceptor organelles, I decided to study the structure of the VPS13's WD40 domain and how it binds to the PxP motif.

Chapter 4.1 Identification of soluble VPS13's WD40 domain fragment

VPS13 contains an N-terminal lipid transfer domain followed by a WD40 domain and a DH-PH domain at the C-terminus (Figure 4.1). However, the exact boundaries of the WD40 domain are unknown. As the first step in studying the WD40 domain of VPS13, I designed a series of fragments with various N- and C-terminal boundaries and tested their ability to fold well using an *E. coli* expression system. From the 22 constructs that I designed and expressed, I hoped to find a soluble, well-behaved fragment that includes the entire WD40 domain. The list of fragments can be found in Supplemental Table 4.1. Six out of the 22 constructs expressed well. I picked the longest soluble fragment, and trimmed its boundaries further to generate a final construct consisting of VPS13 residues 1944–2635, which has a size of 79kDa. I tried both N- and C-terminally 6xHis tagged fragments, and found that the C-terminally tagged variant had comparatively fewer degradation products upon purifying the proteins under similar conditions, therefore more selectively enriching for the complete fragment during affinity binding. The construct ran as a monodisperse peak at around 15ml from Superdex 200 10/300 size exclusion chromatography (Figure 4.1). It ran as a single protein band around 79kDa determined by SDS gel electrophoresis. An aliquot from the peak fraction was imaged using negative stain electron microscopy (EM), which revealed that the WD40 domain folded into a semi-circle shape (Figure 4.3), similar to the structural feature also present in full length VPS13 that was also imaged using negative stain EM (De et al., 2017).

Apart from the WD40 domain, I designed several fragments comprising the PH-DH domain and tested their expression in *E. coli*. The constructs I made and tested by *E. coli* expression are also indicated in Supplemental Table 4.1. However, none of them behaved well upon purification from *E. coli*. I reasoned that it is because some binding partners, or other regions of VPS13, might be required for the fragments containing this domain to fold properly *in vitro*.

Chapter 4.2 PxP motif interacts with C-terminus of VPS13's WD40 domain

To future investigate the interaction between the WD40 domain of VPS13 and the PxP motif, a copy of the PxP motif from Mcp1 (about 10 amino acids long) was fused to the N-terminus of the WD40 domain linked by five amino acids (details can be found in the Materials and Methods section). The chimeric construct behaved well in *E. coli*, and its yield was comparable to that of WD40 domain alone. Interestingly, the peak of the WD40 domain that contained an N-terminally fused PxP motif shifted 2ml to the left in Superdex 200 10/300 size exclusion chromatography (Figure 4.2), suggesting an increase in size compared with WD40 domain alone. Negative stain EM of this WD40 domain with N-terminally fused PxP motif showed monodisperse particles, and 2D class averaging revealed a ring composed of a dimer of semi-circles (Figure 4.3). In another scenario, the PxP motif was fused to the C-terminus of the WD40 domain via a six amino acid linker. At similar expression and purification conditions, the yield of WD40–PxP is three times that of WD40 domain only, suggesting that the fragment with the PxP motif fused on the C-terminus is comparatively more stable. However, negative stain EM 2D class averages of WD40 with C-terminally fused PxP motif indicates a monomeric semi-circle (Figure 4.3). Overall, the results above suggest that the PxP motif interacts with the C-terminus of VPS13's WD40 domain.

Chapter 4.3 Crystallization of VPS13's WD40 domain

To study the structure of VPS13's WD40 domain, I chose x-ray crystallography as the primary method. Crystal Screen, Index, PEGRx screen (Hampton), Wizard Classic Crystallization Screen (Rigaku) and JCSG+ Suite (Qiagen) were used to hunt for initial "hits." Among the three constructs, the WD40 monomer failed to generate any initial crystal "hits," and the PxP-WD40 dimer gave rise to 48 crystal "hits" from initial screens. A list of crystallization conditions that gave rise to crystal "hits" can be found in Supplemental Table 4.2. In order to optimize crystallization conditions, a customized crystallization screen was designed based on the information from the initial 48 crystal "hits"; the specific conditions are detailed in Supplemental Table 3. Half of the drops from the customized screen grew initial hits, and four of them were promising 3D crystals. Continuing from the four conditions, finally, two of the conditions gave rise to crystals that diffracted to 3.5 Å using the home x-ray generator at the Yale Medical School (Figure 4.4). (For details on crystallization conditions and x-ray generator settings used for exposing the crystals, see the Materials and Methods section and Supplemental Table 4.3.) The crystals that diffracted well were highly dependent on the freshness and concentration of the protein. The method for determining the concentration of the protein is described in Materials and Methods section.

Chapter 4.4 Solving the phase problem for the structure of VPS13's WD40 domain

I took two approaches in parallel in order to solve the phase problem for the crystal structure of the VPS13's WD40 domain. I initially planned to take advantage of the anomalous dispersion signal from heavy metals incorporated in the crystals for phasing. The heavy metal must bind the protein specifically and can either be soaked into a pre-existing crystal or co-crystallized with the protein. In order to test the heavy metal binding properties of the VPS13's WD40 domain, I set up a heavy metal binding screen where I incubated purified protein with a series of heavy metal solutions. I found out that the WD40 domain can bind with gold, mercury, cadmium and lead compounds (Figure 4.5 and Figure 4.6). The result provides several options for heavy metal soaking or co-crystallization. I tried to co-crystallize the protein with either gold or mercury, but was not able to grow a well-diffracting crystal.

The second approach I took for solving the phase problem was by crystallizing selenomethionine-substituted protein. After recently fine-tuning the expression conditions based on our lab's protocols, I managed to produce milligram quantities of selenomethionine-substituted protein. The protein is well-folded as a dimer when assessed by negative staining EM. To obtain a high-quality crystal, I tried using similar crystallization conditions as the native protein, as well as optimizing crystal growth by varying the protein concentration, buffer conditions, temperature, well solution composition, the volume of the drop, as well as micro-seeding, but I was only able to grow crystals that diffract to 7 Å. To optimize the protein fold, I designed two constructs that deleted two different loops (loop1: 2316-2338; loop2: 1964-1976) from the original WD40 domain, but none of them yielded well-behaved protein. Compared to native protein, selenomethionine-substituted protein is less soluble, as it can only be concentrated to two-thirds of the highest concentration of native WD40 domain, and crystals appear in two days in comparison to the 10 days required for native protein crystal formation. From these findings, I believe that slowing down crystal growth of selenomethionine-substituted protein will help with the ordering of crystal.

Another avenue for structure determination might be cryo-EM. If the molecule is too flexible to obtain an atomic resolution structure by cryo-EM, a combination of cryo-EM and x-ray crystallography can be used, where a lower resolution version of the structure from cryo-EM could be used as a search model for molecular replacement. However, after testing four different freezing conditions, I have not yet found freezing conditions in order to obtain good cryo grids (Supplemental table 4.4). Ice on the four grids was too thick to acquire a good signal for the protein particles. Lowering the glycerol concentration in final protein might help with ice thickness on the grids.

Materials and Methods

Plasmid construction. Constructs of wildtype VPS13's WD40 domain were PCR amplified from *C. thermophilum* genomic DNA and cloned into pET-Duet plasmids containing a uncleavable N- or C-terminal 6xHis tag using T4 ligase. Constructs of wildtype VPS13 PH-DH domain were PCR amplified from *C. thermophilum* genomic DNA and cloned into pCDF vector containing a uncleavable N- GST tag using T4 ligase. Plasmids and insert were linearized via BamH1 and Not1 restriction enzymes (NEB). Loop deletion constructs were generated using Q5® Site-Directed Mutagenesis Kit (NEB).

Construct information for *C. thermophilum* VPS13 PxP-linker-WD40-6xHis

Backbone: Pet-Duet. (Ampicillin resistance; F primer: pet-up; R primer: duet-down)

Sequence of insert:

MVSLVELDPAPIA(*PxPmotif*)EDAVVD(*linker*)APYRIRNYTGFDVIISTKRQIPGASPTTEQQLPTMTLRLEDGQEAPWSFEEWEKMRESLMTESSTANSISVQLVGSGFQEVKSIRLTREGEFLFGLKPKTQQVLHKLLVEIKLGKDNIKYVTLRSPLLVENDTGIVVELGVYDAHEGHLLKIERINPGESKPAPVGAAYFKSLLVRPDPGFKYGWSSDTLWWRDLLKRPTKTLVCKSEQYGGEVFYFRLHARWDQANPLTRNYPYMRLKLTAPLTIENLLPYDFKYKIYDRVNKQEWNNFLRKGGSIPVHMVDLSHTFLLGIEMQDTPFQASEFVVINTGNADDFKKDSHLVVKDNAGMPLNLRLHYFRIPDGGGSFKVTVYSPYVILNKTGLDVSVRSKGFMQSARAAAGQTLIDVGGDGQKKARPLMFSFHNDDHRNRALLKAGDSEWSKPQSFDAIGSTTEVVLQTANRNAEIHLGVTVDSGQGKYKMVKVVTLAPRYVIHKLGEDINIREPSSSFWIPLKHGAHRPLHWLQRGAVKQL

CLCYPGVDNQWTAPFNISDLGITHLKIARAGQRQRLIRVEILMEDATIFLNLSMEQ
RNWPFSMRNESDTEFTFYQVNPTIEEDASEDRSGWRPVRYRLPPRSIMPYAWDFP
AAKHKEICICAYNKERHVKLQEIGNLMPMKLALPNGESKTIDINVTADGPTQTLI
LSNYRQSKSLYRQ(*CT-VPS13-1944-2635*)HHHHHH(*6 x His tag without linker*)

Expression and purification of native VPS13's WD40 protein C-terminally tagged VPS13's WD40 domain was expressed in BL21(DE3) codon plus cells (Agilent). Cells were grown in LB media supplemented with antibiotic at 37°C to an OD of 0.6. Protein expression was induced by 0.5mM of isopropyl β-D-1-thiogalactopyranoside (IPTG) and incubated at 18°C for 20hrs. Cells were pelleted and resuspend using lysis buffer (NaCl 500ml, HEPES 20mM: pH 7.8, Imidazole 20mM, TCEP 1mM, Glycerol 10%) supplemented with 1mM of PMSF (Phenyl Methyl Sulfonyl Fluoride). Cells were lysed with an Emulsiflex-C5 cell disruptor (Avestin). Cell lysate was clarified via centrifugation. The protein was purified using affinity chromatography with Ni-NTA resin (Qiagen). After washing three times with 10 x bed volume of lysis buffer, protein was eluted using lysis buffer supplemented with 500mM imidazole. The elution was then purified using Superdex 200 10/60 column (GE Healthcare) equilibrated with FPLC buffer (NaCl 500ml, HEPES 20mM: pH 7.8, Tcep 1mM, Glycerol 10%). Peak fractions were concentrated using Amicon Ultra 4 with cut-off of 100kDa.

Expression of selenomethionine-substituted protein Selenomethionine-substituted protein expression was modified from methods described previously (Doublie, 1997). To summarize, an overnight LB culture was inoculated into 1L of 1xM9 media supplemented with 0.2% glucose, 2mM Mg2SO4, 0.1mM CaCl2, 0.1mM thiamine, and antibiotic. Cells were grown at 37°C until the OD_{600} reached 0.5. 100mg each of threonine, lysine, phenylalanine; 50mg of leucine, isoleucine, valine; and 120mg of DL-seleno-methionine were added per 1 liter of cell culture. Cells were shaken at 30°C for 1hr to deplete methionine. Protein was induced by 0.5mM of IPTG and overexpressed at 18°C for 20hrs. Selenomethionine-substituted protein was purified using the same strategy as native protein.

Protein crystallization trays WD40 dimer protein was concentrated to a final concentration of 3mg/ml. (The concentration was measured using Bradford assay. Calculation is based on a standard curve: (reads – 0.095) / 0.06943 * 20 / load(μl) = Con (mg/ml). For example, for 4ul of protein solution into 1ml of 1x Bradford solution, normally the reads are around 0.5 – 0.52, meaning the final concentration is around 3mg/ml). The Formulatrix NT8 liquid handling robot was used for setting up 96-well crystallization screen, where the settings were for 100nl of protein mixed with 100nl of mother liquor. The mixture was equilibrated using 50μl of mother liquor with 500mM of NaCl in an Intelli low-profile plate (Hampton). For well-diffracting crystals of the native protein, 2μl of protein was mixed with 2μl of 100mM imidazole, pH 8.0 and 80mM Li2SO4 (mother liquor A). The mixture was equilibrated using 500μl of mother liquor A with 55μl of 5M NaCl. In another case, 2μl of 3mg/ml native protein was mixed with 2μl of 90mM imidazole, pH 8.0 and 50mM Li2SO4 (mother liquor B). The mixture was equilibrated using 500μl of mother liquor B with 55μl of 5M NaCl in 24 well crystallization plate (Hampton M plate). In both cases, crystals appeared after 10 days.

Crystals were mounted in a 0.1-0.2um cryo-loop and dipped serially in mother liquor A/B supplemented with 5% glycerol, 10% glycerol, 15% glycerol and then 20% glycerol. The loops were then mounted, with the crystals centered onto an AFC 4-axis goniometer. Crystals were protected using Oxford Cobra cryo-stream and exposed to Rigaku X-ray Generator for 300s, and the diffraction data was collected with a Dectris Pilatus 200K Pixel Array Detector (Rigaku) in the Macromolecular X-Ray Crystallography Core at the Yale Medical School.

Heavy metal binding and gel shift assay For heavy metal screening, 4μl of purified C-terminal 6xHis tagged PxP-WD40 protein at 1mg/ml was mixed with 4μl of the heavy metal stock solutions (Hampton) listed with their concentrations in Figure 4.5 and 4.6. Concentrations used for heavy metal solutions are indicated. If the concentrations of heavy metal solutions are higher than the indicated concentrations, the protein will precipitate out upon mixing. The mixtures were kept on ice for 30 minutes. 8μl of native gel loading buffer was then mixed with protein and heavy metal before loading onto a native gel. 15μl of the final mixture was loaded onto a 4% - 15% gradient gel (Bio-Rad). The native gel was run at a constant voltage of 100V for 100mins at 4°C.

Supplemental Table 4.1 Construct boundary information for VPS13’s WD40 domain. Well-behaved constructs are bolded.

Constructs	domain
C. thermophilum VPS13 1626 – 2638	WD40
C. thermophilum VPS13 1807 – 2638	WD40
***C. thermophilum* VPS13 1940 – 2638**	WD40

C. thermophilum VPS13 2040 – 2638	WD40
C. thermophilum VPS13 1807 – 2798	WD40
C. thermophilum VPS13 1940 – 2502	WD40
***C. thermophilum* VPS13 1940 – 2533**	WD40
***C. thermophilum* VPS13 1940 – 2571**	WD40
***C. thermophilum* VPS13 1940 – 2605**	WD40
C. thermophilum VPS13 1977 – 2502	WD40
C. thermophilum VPS13 1977 – 2533	WD40
C. thermophilum VPS13 1977 – 2571	WD40
C. thermophilum VPS13 1977 – 2605	WD40
C. thermophilum VPS13 2007 – 2502	WD40
C. thermophilum VPS13 2007 – 2533	WD40
C. thermophilum VPS13 2007 – 2571	WD40
C. thermophilum VPS13 2007 – 2605	WD40
C. thermophilum VPS13 2042 – 2502	WD40
***C. thermophilum* VPS13 2042 – 2533**	WD40
***C. thermophilum* VPS13 2042 – 2571**	WD40
C. thermophilum VPS13 2042 – 2605	WD40
C. thermophilum VPS13 2649 – 3225	PH-DH-PH
C. thermophilum VPS13 2649 – 3087	PH-DH
C. thermophilum VPS13 2811- 3225	DH-PH
C. thermophilum VPS13 2811 – 3087	DH

Supplemental Table 4.2. Crystallization conditions for initial "hits" of WD40 dimer; conditions for 2D or 3D crystals are bolded.

Number	Buffer	Salt	Precipitant
1	0.1 M Sodium acetate trihydrate pH 4.0		10% w/v Polyethylene glycol 4,000
2	0.1 M MES monohydrate pH 6.0,		14% w/v Polyethylene glycol 4,000
3	**0.1 M Sodium citrate tribasic dihydrate pH 5.5**	**0.1 M Lithium sulfate monohydrate,**	**20% w/v Polyethylene glycol 1,000**
4	**0.1 M Imidazole pH 7.0**	**2% v/v Tacsimate pH 7.0, 5% v/v 2-Propanol**	**8% w/v Polyethylene glycol 3,350**
5	0.1 M MES monohydrate pH 6.0,	0.4 M Sodium malonate pH 6.0	0.5% w/v Polyethylene glycol 10,000
6	0.1 M BIS-TRIS pH 6.5	0.2 M Potassium sodium tartrate tetrahydrate,	10% w/v Polyethylene glycol 10,000
7	100 mM Potassium phosphate monobasic/ Sodium phosphate dibasic pH 6.2		10% (w/v) PEG 3000

8	**100 mM Imidazole/ Hydrochloric acid pH 8.0**		**1000 mM Ammonium phosphate dibasic**
9	100 mM Tris base/ Hydrochloric acid pH 8.5		20% (w/v) PEG 1000
10	100 mM HEPES/ Sodium hydroxide pH 7.5		30% (v/v) PEG 400
11	100 mM HEPES/ Sodium hydroxide pH 7.5	200 mM Sodium chloride	10% (v/v) 2-propanol
12	0.1 M bis-Tris pH 5.5	1 M Ammonium sulfate	1% w/v PEG 3350
13	0.1 M HEPES pH 7.0	1.0 M Succinic acid pH 7.0	1% w/v Polyethylene glycol monomethyl ether 2,000
14	0.2 M Ammonium citrate tribasic pH 7.0		20% w/v Polyethylene glycol 3,350
15		0.4 M Ammonium phosphate monobasic	
16	0.1 M Sodium acetate trihydrate pH 4.6		

17	0.1 M MES monohydrate pH 6.5		12% w/v Polyethylene glycol 20,000
18	0.1 M Sodium acetate trihydrate pH 4.0		10% w/v Polyethylene glycol monomethyl ether 2,000
19	0.1 M Sodium citrate tribasic dihydrate pH 5.5		18% w/v Polyethylene glycol 3,350
20	**0.1 M BIS-TRIS pH 6.5**	**28% v/v 2-Propanol**	**3% v/v Polyethylene glycol 200**
21	0.1 M Imidazole pH 7.0		20% v/v Jeffamine ® ED-2001 pH 7.0
22	100 mM Sodium acetate/ Acetic acid pH 4.5	1000 mM Ammonium phosphate dibasic	
23	**100 mM Imidazole/ Hydrochloric acid pH 8.0**	**10% (v/v) 2-propanol**	
24	0.1 M Sodium citrate tribasic dihydrate pH 5.5		22% w/v Polyethylene glycol 1,000

25		**0.4 M Potassium sodium tartrate tetrahydrate**	
26	0.1 M Imidazole pH 6.5		1.0 M Sodium acetate trihydrate
27	0.1 M Sodium citrate tribasic dihydrate pH 5.6	20% v/v 2-Propanol	
28	0.1 M Sodium citrate tribasic dihydrate pH 5.6	0.5 M Sodium chloride	2% v/v Ethylene imine polymer
29	0.1 M tri-Sodium citrate pH 5.5		20% w/v PEG 3000
30	**0.2 M di-Ammonium citrate pH 5.0**		**20% w/v PEG 3350**
31	0.1 M Succinic acid pH 7.0		15% w/v PEG 3350
32	0.1 M bis-Tris pH 5.5	0.1 M Ammonium acetate	17% w/v PEG 10,000
33	0.1 M bis-Tris pH 5.5	0.2 M Ammonium sulfate	25% w/v PEG 3350

34	0.1 M bis-Tris pH 5.5	0.2 M Magnesium chloride	25% w/v PEG 3350
35	0.1 M BIS-TRIS pH 5.5	0.3 M Magnesium formate dihydrate	
36	0.1 M HEPES pH 7.0	1.0 M Ammonium sulfate	0.5% w/v Polyethylene glycol 8,000
37		0.2 M Ammonium citrate tribasic pH 7.0	20% w/v Polyethylene glycol 3,350
38	0.1 M BIS-TRIS pH 5.5	0.1 M Ammonium acetate	17% w/v Polyethylene glycol 10,000
39	**0.1 M Sodium citrate tribasic dihydrate pH 5.0**		**30% v/v Polyethylene glycol monomethyl ether 550**
40	**0.1 M HEPES pH 7.5**		**4% w/v Polyethylene glycol 8,000**
41	0.1 M Imidazole pH 7.0		12% w/v Polyethylene glycol 20,000
42	0.1 M Sodium citrate tribasic dihydrate pH 5.5	0.10% w/v n-Octyl-b-D-glucoside	22% w/v Polyethylene glycol 3,350
43	0.1 M HEPES pH 7.5		10% w/v PEG 8000, 8% v/v Ethylene glycol

44	0.1 M Phosphate-citrate pH 4.2		40% v/v PEG 300
45	0.1 M Imidazole pH 8		10% w/v PEG 8000
46	0.1 M HEPES pH 7.5	0.02 M Magnesium chloride	22% w/v Polyacrylic acid 5100 sodium salt
47			35% v/v 1,4-Dioxane
48	0.1 M MES monohydrate pH 6.0		20% w/v Polyethylene glycol monomethyl ether 2,000

Supplemental Table 4.3 Customized crystallization screen for VPS13's WD40 dimer. Conditions for 3D crystals are bolded.

B1; S1;	B2; S1;	B3; S1;	B4; S1;	B5; S1;	B1; S2;	B2; S2;	B3; S2;	B4; S2;	B5; S2;
B1; S3;	B2; S3;	B3; S3;	B4; S3;	**B5; S3;**	B1; S4;	B2; S4;	B3; S4;	B4; S4;	B5; S4;
B1; P1	B2; P1	B3; P1	B4; P1	**B5; P1**	B1; P2;	B2; P2;	B3; P2;	B4; P2;	B5; P2;
B1; S1; P1	B2; S1; P1	B3; S1; P1	B4; S1; P1	B5; S1; P1	B1; S2; P1	B2; S2; P1	B3; S2; P1	B4; S2; P1	B5; S2; P1
B1; S3; P1	B2; S3; P1	B3; S3; P1	B4; S3; P1	B5; S3; P1	B1; S4; P1	B2; S4; P1	B3; S4; P1	B4; S4; P1	B5; S4; P1

B1; S1; P2;	B2; S1; P2;	B3; S1; P2;	B4; S1; P2;	B5; S1; P2;	B1; S2; P2;	B2; S2; P2;	B3; S2; P2;	B4; S2; P2;	B5; S2; P2;
B1; S3; P2;	B2; S3; P2;	B3; S3; P2;	B4; S3; P2;	B5; S3; P2;	B1; S4; P2;	B2; S4; P2;	B3; S4; P2;	B4; S4; P2;	B5; S4; P2;

B1: imidazole pH 7.5 100mM, B2: Bis-tris pH 6.5 100mM, B3: Sodium Citrate pH 5.0 100mM, B4: Ammonium Citrate pH 5.0 100mM, B5: HEPES Ph 7.5 100mM,

S1: Potassium Sodium tartrate 400mM, S2: Ammonium phosphate 500mM, S3: Lithium Sulfate 100mM, S4: Ammonium tartrate 400mM

P1: 2-propanol 10%, P2: PEG300 20%

Supplemental Table 4.4 Cryo grid freezing conditions for PxP-WD40

Protein	**Force**	**Time**	**Grid type**	**Glow Discharge**	**Temperature Humidity**	**Detergent**	**Negative stain**	**Glacios Check**
WD40 dimer	-2	2s	Quantifoil R1.2/1.3 300 Mesh, Copper	30s	4°C/90%	None	Looks good	All black

WD40 dimer	-2	2s	Quantifoil R1.2/1.3 300 Mesh, Copper	30s	4℃/90%	0.02% OG	Looks good	All black
WD40 dimer	-2	5s	Quantifoil R1.2/1.3 300 Mesh, Copper	30s	4℃/90%	None	Looks good	All black
WD40 dimer	-2	5s	Quantifoil R1.2/1.3 300 Mesh, Copper	30s	4℃/90%	0.02% OG	Looks good	No particles in hole

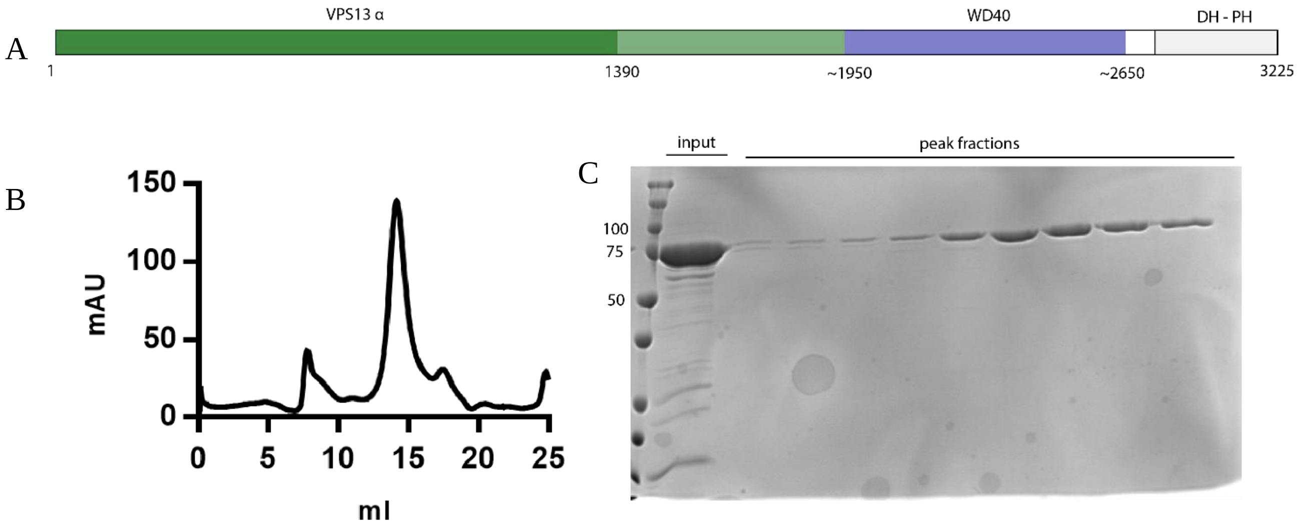

Figure 4.1 (A) Schematic of the putative domain architecture of *Chaetomium thermophilum* VPS13 protein. Position of the boundaries of domains are indicated; (B) Superdex 200 10/30 chromatography profile of WD40 domain (construct information: CT-VPS13-1944-2635-6xHis). Peak position at around 15ml. (C) SDS gel electrophoresis of peak fractions. Position of protein markers are indicated.

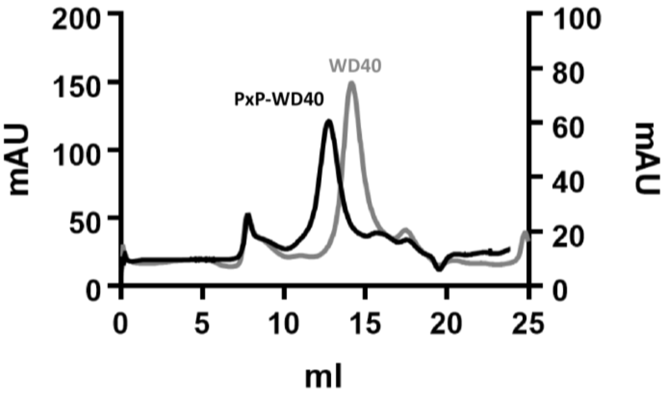

Figure 4.2 Comparison of Superdex 200 10/30 chromatography profile of WD40 domain (construct information: CT-VPS13-1944-2635-6xHis) and PxP-WD40 domain (construct information: CT-VPS13-PxP-5 amino acid linker – 1944 – 2635 – 6xHis). WD40 domain has a peak at 15ml while PxP-WD40's peak position is around 13ml.

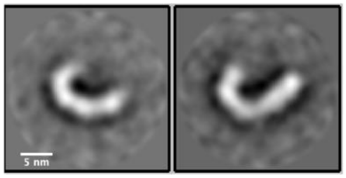

2D class average of WD40 domain

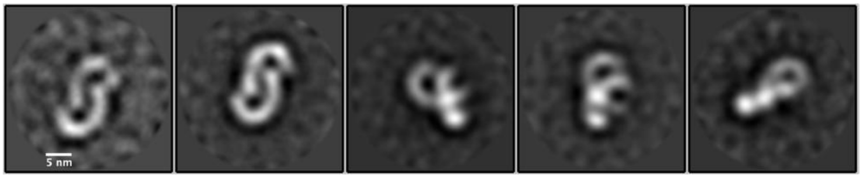

2D class average of PxP - WD40

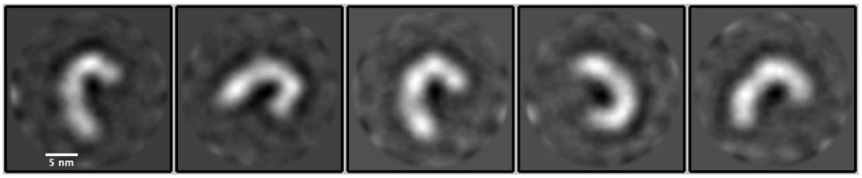

2D class average of WD40 - PxP

Figure 4.3 2D class averages of WD40 domain, PxP–WD40 and WD40–PxP. Scale bar is indicated. WD40 and WD40–PxP adopt the shape of a semi-circle ring. PxP–WD40 forms a dimer.

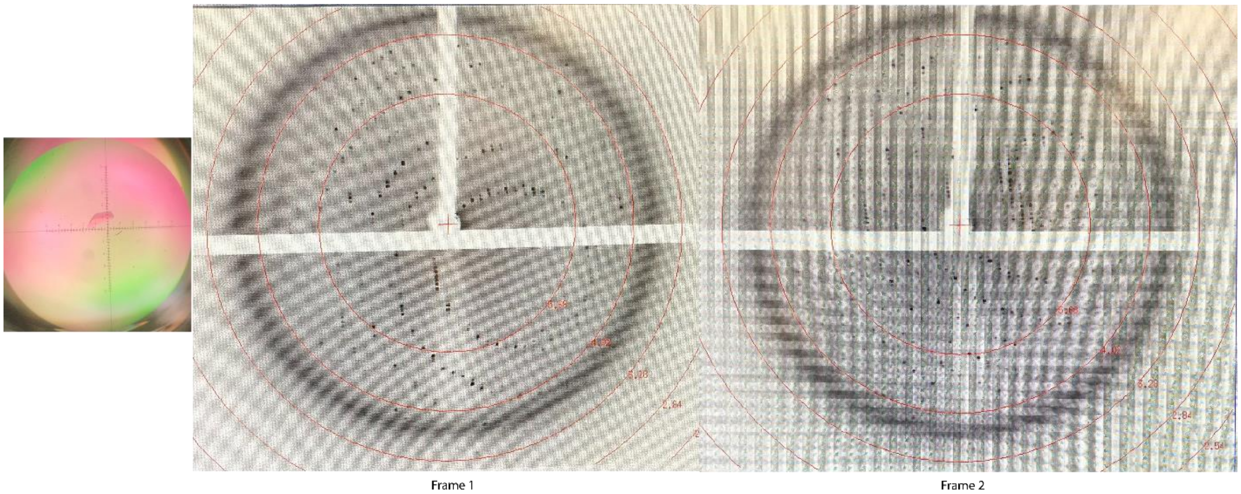

Frame 1

Frame 2

Figure 4.4 Native PxP-WD40 protein crystals diffract to 3.5 Å in-house. Crystals were serially dipped into crystallization buffer supplemented with 5% glycerol, 10% glycerol, 15% glycerol and then 20% glycerol. The crystal was then exposed to Rigaku X-ray Generator for 300s and the diffraction data (the two frames are 90° apart) was collected with a Pilatus 200k Pixel Array Detector. Preliminary analysis suggests the crystals may be monoclinic (P2) with a = 80.18, b = 168.79, c = 80.41 or Orthorhombic ($C222_1$) with a = 108.61, b = 117.46, c = 168.38.

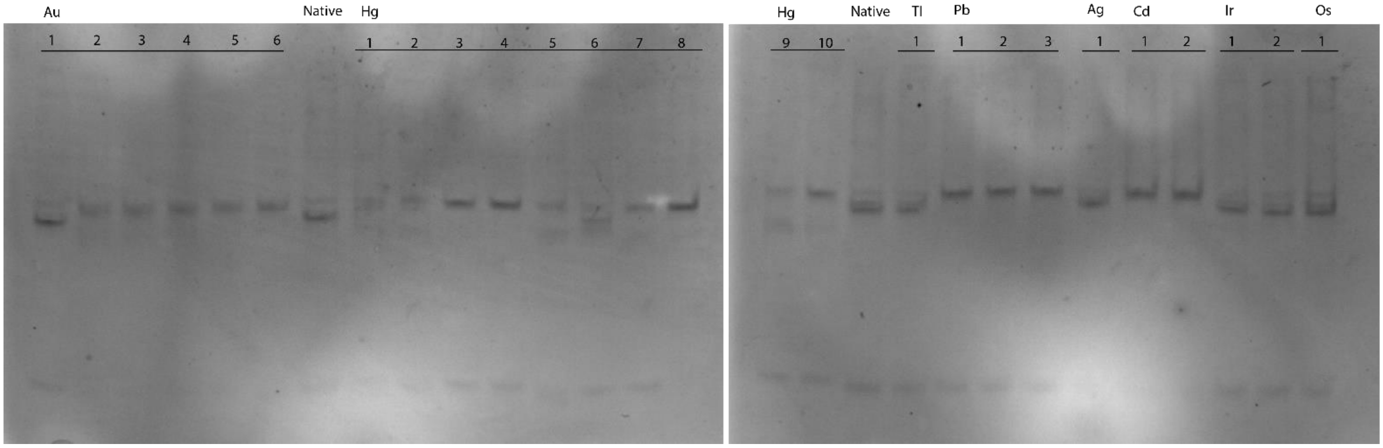

Figure 4.5 Heavy metal screen of PxP–WD40. Purified protein was incubated with heavy metal solutions (concentrations are indicated below) with a ratio of 1:1. Shift of protein bands on native gel electrophoresis indicates the heavy metal binding. Native: native protein; Au-1: KAu(CN)2, 1mM; Au-2: KAuCl4 • xH2O, 1mM; Au-3: NaAuCl4 • 2H2O, 1mM; Au-4: AuCl3, 1mM; Au-5: HAuCl4 • 3H2O, 1mM; Au-6: KAuBr4 • 2H2O, 1mM; Hg-1: C13H17HgNO6 1mM; Hg-2: C2H5HgH2PO4, 1mM; Hg-3: HgCl2, 1mM; Hg-4: Hg(OOCCH3)2, 1mM; Hg-5: C9H9HgNaO2S, 1mM; Hg-6: C8H8HgO2, 0.3mM; Hg-7: K2HgI4, 1mM; Hg-8: HgBr2, 0.5mM; Hg-9: Hg(NO3)2 • H2O, 1mM; Hg-10: HgO, 1mM; Tl-1: Tl(O2C2H3)3 • xH2O, 1mM; Pb-1: Pb(CH3COO)2 • 3H2O, 1mM; Pb-2: Pb(NO3)2, 1mM; Pb-3: PbCl2, 1mM; Ag-1: AgNO3, 1mM; Cd-1: CdCl2 • xH2O, 1mM; Cd-2: CdI2, 1mM; Ir-1: K2IrCl6, 1mM; Ir-2: K3Ir(NO2)6, 1mM; Os-1:K2OsO4 • 2H2O, 1mM;

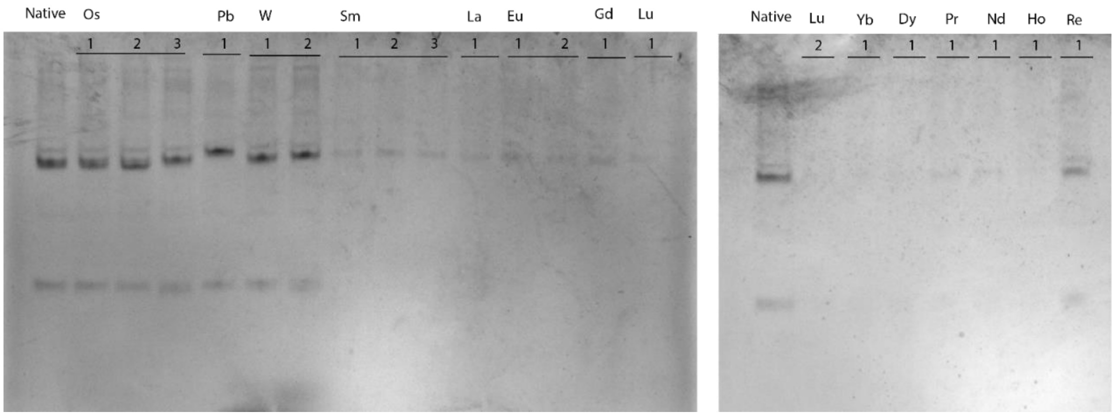

Figure 4.6 Heavy metal screen of PxP–WD40, continued from last figure.

Native: native protein; Os-1: (NH4)2OsBr6, 1mM; Os-2: K2OsCl6 1mM; Os-3: OsCl3 • xH2O 1mM; Pb-1: CH3CO2Pb(CH3)3 2mM; W-1: Na2WO4 • 2H2O 5mM; W-2: (NH4)2WS4 , 5mM; Sm-1: SmCl3 • 6H2O 5mM; Sm-2: Sm(O2C2H3)3 • xH2O 5mM; Sm-3: Sm(NO3)3 • 6H2O 5mM; La-1: La(NO3)3 • 6H2O 5mM; Eu-1: Eu(NO3)3 • 6H2O 5mM; Eu-2: EuCl3 • 6H2O 5mM; Gd-1: GdCl3 • xH2O 5mM; Lu-1: LuCl3 • 6H2O 5mM; Lu-2: Lu(O2C2H3)3 • Xh2o 5mM; Yb-1: YbCl3 • Xh2O 5mM; Dy-1: DyCl3 • 6H2O

Reference:

Bean, B. D. M., Dziurdzik, S. K., Kolehmainen, K. L., Fowler, C. M. S., Kwong, W. K., Grad, L. I., . . . Conibear, E. (2018). Competitive organelle-specific adaptors recruit Vps13 to membrane contact sites. *J Cell Biol, 217*(10), 3593-3607. doi: 10.1083/jcb.201804111

De, M., Oleskie, A. N., Ayyash, M., Dutta, S., Mancour, L., Abazeed, M. E., . . . Fuller, R. S. (2017). The Vps13p-Cdc31p complex is directly required for TGN late endosome transport and TGN homotypic fusion. *Journal of Cell Biology, 216*(2), 425-439. doi: 10.1083/jcb.201606078

Doublie, S. (1997). Preparation of selenomethionyl proteins for phase determination. *Methods Enzymol, 276*, 523-530.

Kornmann, B. (2020). The endoplasmic reticulum-mitochondria encounter structure: coordinating lipid metabolism across membranes. *Biol Chem, 401*(6-7), 811-820. doi: 10.1515/hsz-2020-0102

Kumar, N., Leonzino, M., Hancock-Cerutti, W., Horenkamp, F. A., Li, P., Lees, J. A., . . . De Camilli, P. (2018). VPS13A and VPS13C are lipid transport proteins differentially localized at ER contact sites. *J Cell Biol, 217*(10), 3625-3639. doi: 10.1083/jcb.201807019

Olkkonen, V. M. (2015). OSBP-Related Protein Family in Lipid Transport Over Membrane Contact Sites. *Lipid Insights, 8*(Suppl 1), 1-9. doi: 10.4137/LPI.S31726

Qiu, S., Leung, A., Bo, Y., Kozak, R. A., Anand, S. P., Warkentin, C., . . . Cote, M. (2018). Ebola virus requires phosphatidylinositol (3,5) bisphosphate production for efficient viral entry. *Virology, 513*, 17-28. doi: 10.1016/j.virol.2017.09.028

Sbrissa, D., Ikonomov, O. C., & Shisheva, A. (2000). PIKfyve lipid kinase is a protein kinase: downregulation of 5'-phosphoinositide product formation by autophosphorylation. *Biochemistry, 39*(51), 15980-15989. doi: 10.1021/bi001897f

ProQuest LLC
789 East Eisenhower Parkway
P.O. Box 1346
Ann Arbor, MI 48106 - 1346 USA